Ozone and Aerosol Optical Properties from Ground based Ultra-Violet Irradiance Measurements

By
Thomas E. Taylor, James Slusser and Graeme L. Stephens

Department of Atmospheric Science
Colorado State University
Fort Collins, Colorado

Research was supported by the Office of Biological and Environmental Research of the US Department of Energy (DE-FG02-94ER61748) as part of the Atmospheric Radiation measurement Program and by the USDA/CSREES grant 2004-34263-14270 Amendment 1, through the UltraViolet Monitoring and Research Program at the National Resource Ecology Laboratory at CSU.

Colorado State University

Department of Atmospheric Science

Paper No. 767

OZONE AND AEROSOL OPTICAL PROPERTIES FROM GROUND BASED ULTRA-VIOLET IRRADIANCE MEASUREMENTS

Thomas E. Taylor, James Slusser and Graeme L. Stephens

Research Supported by the Office of Biological and Environmental Research of the U.S. Department of Energy (DE-FG02-94ER61748) as part of the Atmospheric Radiation Measurement Program and by the USDA/CSREES Grant 2004-34263-14270-Amendment 1 through the UltraViolet Monitoring and Research Program at the Natural Resource Ecology Laboratory at Colorado State University

OZONE AND AEROSOL OPTICAL PROPERTIES FROM GROUND BASED ULTRA-VIOLET IRRADIANCE MEASUREMENTS

Thomas E. Taylor, James Slusser and Graeme L. Stephens

Research supported by the UltraViolet Monitoring and Research Program at the Natural Resource Ecology Laboratory at Colorado State University

Principal Investigator: James Slusser

Department of Atmospheric Science

Colorado State University

Fort Collins, Colorado 80523

Spring, 2006

Atmospheric Science Paper No. xxx

ABSTRACT

OZONE AND AEROSOL OPTICAL PROPERTIES FROM GROUND BASED ULTRA-VIOLET IRRADIANCE MEASUREMENTS

Error analysis and characterization of an optimal estimation retrieval algorithm are described. The algorithm, which was initially developed by Goering *et al.*, estimates values of aerosol optical properties (aerosol optical depths, AOD, and aerosol single scattering albedo, SSA) at 7 wavelengths in the ultraviolet (UV) spectral region as well as total column ozone (TOC) Goering et al. (2005). The measurements used in the retrieval algorithm are obtained from a UV Multi-Filter Rotating Shadow-Band Radiometer (UV-MFRSR), which measures diffuse and direct irradiances at 300-, 305-, 311-, 317-, 325-, 332- and 368-nm Bigelow et al. (1998). These radiometers are deployed as part of the United States Department of Agriculture's (USDA) Ultra-Violet Monitoring and Research Program (UVMRP) network of 33 surface stations distributed around the USA. The Tropospheric Ultraviolet/Visible (TUV) radiative transfer model Madronich (1993) is employed as the forward model in the retrieval algorithm.

Several improvements to the original retrieval algorithm were developed. The wavelength independent asymmetry factor, g, was added as an explicit retrieval parameter and *a priori* error covariances were incorporated as a way of adding information to the retrieval. More careful evaluation of the retrieval was performed, including sensitivity studies of the radiative transfer solvers used by the forward model. Model sensitivities to TOC, g and surface albedo over domains of AOD and SSA were used to create a realistic model error budget. Realistic wavelength-dependent surface albedos were incorporated into the model using analytical expressions created from measurements Doda and Green (1981). The new algorithm also uses a more rigorous UV-MFRSR measurement error budget determined from previous research Krotkov et al. (2005) as well as

specified model error derived from the sensitivity analysis. The new version also benefits from several modifications that significantly speed up the retrieval algorithm, making it potentially valuable for routine operational use.

Synthetic testing of the retrieval algorithm for various atmospheric conditions was performed to determine the conditions under which the algorithm produced accurate and statistically significant results. Retrieval results were found to improve with increasing atmospheric turbidity (AOD) and with increasing particle scattering properties (SSA and g). The sensitivity of the results to solar zenith angle was determined to be minimal. Solution spaces of the retrieval in the AOD-SSA domain space were studied to show that the retrieval has a uni-modal solution with respect to these two parameters and that the model has sufficient sensitivity and resolution to these parameters to make reasonable estimates of their values.

The optimal estimation retrieval was performed on a cloud screened data set from May, 2003 at the Panther Junction station in Big Bend National Park, Texas. The monthly time series of AOD, SSA, TOC and g were filtered using the chi-squared value at the 95% significance level before the estimated errors and diagnostics were analyzed to interpret the usefulness of the retrieved parameters. Daily intercomparisons of 368nm AOD with the Langley method Harrison and Michalsky (1994) and TOC with the direct sun method Gao et al. (2001) were then made for May 12 and May 22, which were high and low turbidity cases, respectively. Overall, the retrieval results were shown to be physically consistent. As with the synthetic testing, the retrieval tends to yield more useful results, i.e., lower estimated error and better diagnostic values, with increasing turbidity and scattering properties.

The results are used to establish *a priori* and *posteriori* boundary conditions which can be used in an automated fashion for determining successful retrievals. The results indicate that it is feasible to use the algorithm operationally on the data collected by

the UVMRP network to build a data base of TOC and aerosol optical properties. When implemented on the network of ~30 instruments it will provide a comprehensive and internally consistent climatology of ground-based aerosol properties in the UV spectral range, which can be used for both validation of satellite measurements as well as for regional aerosol and ultra-violet transmission studies.

Thomas E. Taylor
Atmospheric Sciences Department
Colorado State University
Fort Collins, CO 80523
Spring 2006

ACKNOWLEDGMENTS

We would like to thank Drs. Christian Kummerow and John Volckens for their evaluation of this research as well as Dr. Tristan L'Ecuyer for many hours of discussion concerning the fundamentals of the optimal estimation technique and its interpretation. Thanks to Christian Goering for laying the initial foundation of this project. This research was supported by the Office of Biological and Environmental Research of the U.S. Department of Energy (DE-FG02-94ER61748) as part of the Atmospheric Radiation Measurement Program and by the USDA/CSREES Grant 2004-34263-14270-Amendment 1.

Contents

1. Introduction

1a. *The Role of Aerosols in Climate*

Aerosols are suspensions of fine solid or liquid particles in a gas. In the context of the earth's atmosphere they can be composed of a variety of different chemical elements or molecules. In general they range in size from a few tens of Ångstroms to several hundred micrometers Seinfeld and Pandis (1998). More typically they have equivalent spherical diameters ranging from about 1nm for clusters of molecules to about $10^4 = 10,000$nm for salt, dust and combustion particles Rogers and Yau (1989).

For natural background levels of aerosols, about 75% of the total global aerosol mass is produced by the so-called primary aerosol sources, including wind generated dust, volcanic eruptions, forest fires and salts from sea spray Hidy (1972). The generation of aerosols from photochemical and chemical reactions in the atmosphere, which account for about 25% of the total natural global aerosol mass, are secondary sources of aerosol production Hidy (1972). Changes in aerosol concentrations through the activities of humans are referred to as anthropogenic forcings. Anthropogenic sources include the release of sulphates and chlorofluorocarbons (CFC's) from industry, black carbon from the combustion of fossil fuels as well as the release of particulates from biomass burning Houghton et al. (2001). Increases in the concentrations of aerosols, either natural or anthropogenic, can lead to a wide variety of effects at various scales, ranging from the impairment of local and regional air quality due to forest fires to global changes in the stratospheric ozone shield, e.g., McMeeking et al. (2005) and Farman et al. (1985), respectively.

Furthermore, research has convincingly shown that changes in the global abundances of aerosols, generally due to anthropogenic forcings, lead to complicated climate feedback scenarios through direct and indirect effects Nakajima et al. (2001). The direct

aerosol effect refers to direct alteration of the incoming solar beam due to increased aerosol abundance and/or to changes in the absorption and scattering properties of the aerosols. This can yield modifications of both the flux and spectral characteristics of radiation reaching the surface of the earth, as well as alter the atmosphere's vertical temperature profile. The aerosol indirect effect forces changes in the microphysical and precipitation processes of clouds which yield increased reflectances of solar radiation to space as well as suppression of rainfall due to a decrease in the average cloud particle diameter Suzuki et al. (2004). This in turn leads to less efficient scavenging of aerosol pollutants from the atmosphere. It has been conjectured that these feedback effects cause a weakening of the earth's hydrological cycle Ramanathan et al. (2001), which would have tremendous impact on the future of all life on the planet.

1b. *Ultraviolet Radiation and the Ozone Layer*

Of specific concern to the characterization of atmospheric aerosols is the effect that they have on the transmission of UV radiation through the atmosphere of the earth. The UV electromagnetic spectrum spans approximately 10-nm to 400-nm wavelengths. Although the UV spectral band comprises less than 10% of the solar radiant energy at the top of the atmosphere (TOA), it is of paramount importance to the earth climate, as well as for biological and medical reasons, Frederick et al. (1989), Grant and Slusser (2003), Kimlin et al. (2003). There are many factors which can effect the transmission of UV through the atmosphere, making it difficult to accurately measure UV reaching the earth's surface, especially in cloudy and hazy conditions Bernhard and Seckmeyer (1999).

Of great importance with regard to the transmission of UV radiation is the absorption due to ozone. Ozone is considered a trace gas, making up only 0-12 parts per million (ppm) of the total fraction of molecules in the earth's atmosphere, compared to 325 ppm for CO_2 Wallace and Hobbs (1977). Over 90% of the total ozone resides in the strato-

sphere, where it is a stable chemical species between altitudes of about 10 and 25km, and is partially responsible for the strong temperature inversion beginning at the tropopause via the efficient absorption of virtually all UV below about 300-nm Wallace and Hobbs (1977). The remaining 10% of the total global ozone is found in the lower troposphere where it is involved in various chemical processes Seinfeld and Pandis (1998).

1c. *Characterizing and Quantifying Aerosol Parameters*

Characterizing and quantifying aerosols in the earth's atmosphere is a vital task in order to fully understand and predict the Earth Radiation Budget (ERB) and associated climate dynamics and feedbacks due to scattering and absorption of solar radiation. Although much of the research pertaining to the optical properties of aerosols has been focused on the visible regions of the solar spectrum, only recently have scientists begun to explore the interaction of UV radiation with aerosols. There are several techniques which allow for the quantification and study of aerosol properties, including surface and airborne in-situ measurements, chemical transport models and remote sensing. Remote sensing can provide either vertically resolved or vertically integrated properties from both ground and satellite platforms.

Although in-situ sensing of atmospheric properties by various instruments can provide thorough information of both bulk and non-bulk aerosol parameters, these types of measurements are expensive and do not lend themselves well to automated procedures. In-situ measurements are therefore only conducted over very limited spatial and temporal domains. Results from *in situ* measurements provide useful insight into the microscopic and chemical properties of aerosols as well as verification of remotely sensed data.

While remotely sensed data from space has the potential to provide a global picture of aerosol characteristics, and much development has been made in this field in recent years Anderson et al. (2005), the complications of operating equipment from these unser-

viceable platforms require that ground based validation of space-based measurements be performed. Ground validation is performed by pixel matching with satellite data, which must be corrected for differences in wavelength scales and slit resolutions Gröbner and Kerr (2001) as well as temporal and spatial discrepancies Sabburg et al. (2002).

Remote sensing from the earth's surface alleviates some of the issues involved with servicing of the equipment and calibrations that are problematic for satellite retrievals. Both broadband and spectrally resolved instruments (spectroradiometers), with varying levels of complexity and robustness, have been developed for measuring UV. Spectroradiometers normally have more complex mechanical features and include scanning and spectrograph instruments as well as narrow band filter instruments, Seckmeyer et al. (1994), Lantz et al. (2002), Webb (2003). However, surface instrumentation is not without its own set of inherent problems. Data from broadband instrumentation has been scrutinized for the lack of spectral information and the inability to represent the sensitivities of various biological and chemical targets which are important in dosimetry techniques WHO (1994). On the other hand, highly resolved spectral instruments are both more complicated mechanically, as well as more difficult to maintain in calibration Larason and Cromer (2001), making them somewhat cost prohibitive for large networks. Alternatively, use of a robust, stable and mechanically simple instrument, such as the Yankee Environmental multi-filter shadow-band radiometer Harrison et al. (1994) or the CIMEL spectral radiometer, can be deployed as a network to provide reasonable spatial coverage of land surfaces, e.g., Bigelow et al. (1998) and Holben et al. (1998). In addition to validating satellite data, ground-based measurements can be incorporated into radiative transfer models to estimate surface fluxes and other important parameters over global extent.

Aerosol transport models are useful for global studies and allow exploration of uncertainties by perturbing specific input parameters Takemura et al. (2005). Furthermore,

model derived aerosol distributions provide valuable inputs for global circulation models in order to calculate radiative forcings Suzuki et al. (2004). However models are limited in that many assumptions must be made to simplify the physics due to a lack of understanding as well as for computational efficiency.

Radiative transfer models are another useful tool for characterizing aerosols and their effects on radiation. Three categories of models used to calculate UV transmissions have been distinguished by the World Health Organization (WHO). The first of these are empirical models which estimate erythemal doses (spectral UV irradiances weighted by the human skin action spectra) as functions of latitude, SZA, cloud cover, etc. The second class are two-stream radiative transfer models which can be used to calculate ground fluxes based on initial conditions of the atmosphere. These models simply treat the radiation beam in the upward and downward directions with no angular dependencies. The third class distinguished by the WHO are the more complex multi-stream models which parameterize the radiation beam in an angular fashion. These can be used to compute actinic fluxes, which are important for detailed dosimetry techniques as well as for tropospheric chemistry calculations. However, all models have inherent uncertainties as a result of various assumptions and approximations, and as such, these three model types do not always produce equivalent results under the same conditions WHO (1994).

1d. *The Optimal Estimation Technique*

Inversion of remotely sensed data is the most widely used method for obtaining global atmospheric information. This technique relies on indirect determination of unknown parameters via their interaction with electromagnetic radiation Stephens (1994). The inverse problem, as it pertains to the remote sensing of aerosols, relies on some physical model (the forward model) of the atmosphere which can predict radiances based on the known state of the atmosphere. The Tropospheric Ultraviolet-Visible (TUV) radia-

tive transfer model from NCAR was employed as the forward model in this research Madronich (1993).

The inverse problem in remote sensing can be cast in terms of Bayes theorem which assigns probability distribution functions (PDFs) to the measurement and state spaces as well as to the associated errors. Assuming Gaussian statistics of the PDFs, the optimal estimation technique finds the most likely joint PDF of the measurement and state by minimizing the variance between the real and modeled measurement and the variance between the estimated value of the state parameter and the *a priori* value of the state parameter Rodgers (2000). Numerically the problem can be solved several ways. In this research an iterative technique is employed by way of the Gauss-Newton approximation for minimizing a derivative. The optimal estimation technique has been applied specifically to the retrieval of the aerosol optical depth, aerosol single scattering albedo and total ozone column from direct and diffuse irradiance measurements in the UV spectral range by Goering *et al.* Goering et al. (2005), following the framework discussed extensively in Rodgers text Rodgers (2000).

Critical to a successful application of the optimal estimation technique is careful characterization of the input error budgets as well as the *a priori* constraints. This is performed via model sensitivity testing and instrument measurement uncertainty analysis. Also, a set of output diagnostics should be carefully considered to determine the statistical significance, as well as usefulness, of the estimated state parameters.

1e. *The USDA UVMRP Network*

The retrieval algorithm, as established by Goering *et al.*, has been designed specifically to use the surface UV irradiances obtained from the United States Department of Agriculture's (USDA) Ultra-Violet Monitoring and Research Program's (UVMRP) network of UltraViolet Multi-Filter Shadow-Band Radiometers (UV-MFRSR). This network con-

sists of approximately 30 automated instruments, located at field sites spanning the entire United States in a grid-like pattern. The UV-MFRSRs measure voltages of the diffuse and total irradiance beam at 7 wavelength channels in the UV spectrum (300-, 305-, 311-, 317-, 325-, 332-, and 368-nm, each with a nominal bandpass of 2-nm). The diffuse and total voltages, which are used to calculate the direct component of the beam, are corrected for various instrument characteristics (e.g., angular response of the collector and spectral response of the instrument) and then are converted into 3 minute averaged irradiances. This typically provides a time series of between 120 to 300 measurements per day, depending on the latitude and time of year. These irradiances are then cloud screened and used as inputs into the optimal estimation retrieval algorithm to estimate values of aerosol optical depths (at 7 wavelengths), aerosol single scattering albedo (at 7 wavelengths), total ozone column and a wavelength-independent asymmetry factor.

1f. *Research Objectives*

The primary objective of this research is to improve the optimal estimation retrieval algorithm previously established by Goering *et al.* Goering et al. (2005). The following statements summarize how this was achieved:

1. Careful characterization of the forward model and measurement uncertainties used as inputs to the retrieval algorithm was performed. This provides more realistic and useful retrieval results;

2. A wavelength independent asymmetry factor was incorporated into the retrieval algorithm as an explicitly estimated state parameter, rather than using a fixed value;

3. The most efficient operational mode of the radiative transfer solver, i.e., Delta-Eddington approximation or n-stream discrete ordinate approximation was determined. Other minor modifications to the algorithm were performed to increase its

time efficiency and error trapping skill;

4. Boundary conditions were placed on the physical domain space, i.e., SZAs, AODs, etc., within which the retrieval algorithm produces statistically significant and accurate retrievals of the state parameters with reasonably small estimated errors.

1g. *Organization*

This document contains 7 chapters. Chapter 2 lays the groundwork for this research by briefly introducing the basic concepts of radiative transfer and discussing the interaction of UV radiation with the earth's atmosphere. Furthermore, it describes in detail the key optical properties of aerosols pertaining to the UV spectrum, as well as discussion of the previous research conducted on aerosol retrievals in the UV. Chapter 3 provides a survey of the inverse problem, Bayes Theorem and the optimal estimation technique. A detailed discussion of the optimal estimation diagnostic outputs is also given. Chapter 4 discusses the irradiance measurements of the UV-MFRSR instrument and gives a detailed account of the sensitivity studies performed on the Tropospheric Ultraviolet-Visible (TUV) radiative transfer model. The wavelength dependent error budget used in the retrieval algorithm is also addressed. Chapter 5 describes the synthetic retrievals that were performed to characterize the conditions under which the retrieval provides useful results. Also testing of the retrieval solution spaces is described. Chapter 6 analyzes retrieval data and diagnostic outputs from a one month data set performed at the Panther Junction, Texas research site. Intercomparisons with independent methods and results from previous research are highlighted. Finally, Chapter 7 presents a summary of the results and a guiding policy for successful use of the optimal estimation retrieval for varying atmospheric conditions. Future research ideas are also listed.

2. Radiative Transfer and Atmospheric Transmission in the Ultraviolet Spectrum

For brevity the treatment of atmospheric radiative transfer will be limited to the fundamental definitions used throughout both this text and the radiative transfer solver used in the TUV forward model code. The discussion will closely follow that given by Liou in his introductory text book Liou (2002).

2a. *Brief Introduction to Atmospheric Radiative Transfer*

Electromagnetic (EM) energy is produced by oscillating electric charges in a magnetic field and can be discussed in terms of either waves or particles Hecht (1987). The particle, or photon, theory is quite useful for explaining the quantized nature of light, and optical instruments often use photon counting to measure radiation. However, for such phenomena as scattering and absorption, which are the primary interactions considered in this work, the wave-like nature of light is more conveniently employed. Waves of EM energy are comprised of inversely proportional, sinusoidal electric and magnetic waves which are mutually perpendicular to one another as well as to the direction of motion.

Two important optical processes are considered in this research concerning the interaction of light with matter. These are scattering and absorption. Scattering of radiation refers to the change in the direction of propagation without a change in wavelength when EM waves are incident on a particle or gas molecule. Although scattering is a function of the polarizibility of the particle, it is also highly dependent on the particle's size and shape, making it a pseudo-macroscopic phenomenon. In the UV spectral region Rayleigh scattering by small air molecules is of great importance.

The second optical process of concern is absorption. Absorption refers to the transfer of energy from the incident EM wave to a particle or gas molecule by way of electronic

and molecular transitions. This process has less to do with the macroscopic size and shape of the particle and is more a function of the atomic and molecular chemistry. Absorption by atomic and molecular oxygen (O and O_2) and nitrogen (N_2), as well as by ozone (O_3) and other trace gases (e.g. SO_2 and NO_2), make remote sensing of the earth's atmosphere possible due to the distinct spectral "signatures" of these species.

Scattering and absorption processes occur simultaneously in the earth's atmosphere, although one often dominates the other depending on the wavelength regime of interest as well as the atmospheric composition. To describe the wavelength regime relative to the size of the atmospheric particles the size parameter, x, is introduced. It relates the circumference of the particle to the wavelength of EM radiation as,

$$x = \frac{2\pi a}{\lambda}, \tag{1}$$

where a is the particle radius.

Scattering and absorption, as well as extinction, which is the sum of the two, i.e., $E = S + A$, are described in terms of cross sections, mass cross sections and coefficients. Cross sections have units of $[cm^2]$ and will be represented using the symbols σ_e, σ_s, σ_a, for extinction, scattering and absorption, respectively. Mass cross sections have units of $[cm^2 g^{-1}]$ and will be represented using the symbols η_e, η_s, η_a. Note that η is a nonconventional symbol but is used here to avoid double use of the symbol k which appears to be common in the literature. When cross sections are multiplied by the number density of the particle, n_0 $[cm^{-3}]$ or when mass cross sections are multiplied by the particle density, ρ $[gcm^{-3}]$, the result is the extinction, scattering or absorption coefficient $[cm^{-1}]$, expressed using the symbols k_e, k_s and k_a, respectively. The cross sections and mass cross sections are non bulk parameters, i.e., they do not depend on the quantity of particles present, while the extinction, scattering and absorption coefficients are bulk parameters.

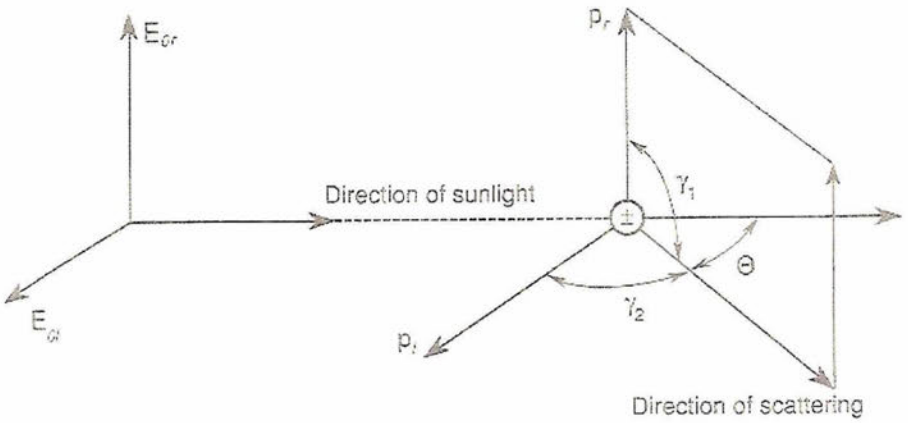

Figure 1: Geometry describing scattering of a radiation by a spherical particle to direction Θ. Taken from Liou (2002).

The relative importance of scattering and absorption at some particular wavelength and for some particular state of the atmosphere can be determined by comparing the scattering and absorption coefficients. Light which is not extincted is transmitted. Therefore fractional transmission, T, is defined as $1 - E$, where E is the total fraction extincted.

i. Scattering The scattering efficiency of a particle, Q_s, is defined as the ratio of the effective scattering cross section, σ_s, to the geometric area of the particle;

$$Q_s = \frac{\sigma_s}{\pi a^2}. \tag{2}$$

where a is the particle radius.

The scattering cross section, σ_s, is defined as the ratio of the flux, f $[W]$ to the incident flux density, F $[Wm^{-2}]$, but can also be written in terms of particle parameters as;

$$\sigma_s = \frac{f}{F} = \frac{128\alpha_p^2\pi^5}{3\lambda^4}, \tag{3}$$

where α_p gives the polarizibility of a particle in units of volume. Although polarization is an important concept in radiative transfer, in this research we are dealing exclusively with unpolarized solar radiation, so no further discussion of it will be given.

During a single scattering event, energy is redistributed from the original beam direction onto a sphere centered on the scatterer. The phase function, $P(\cos\Theta)$, is introduced to describe this process for use in multiple scattering radiative transfer calculations. Here Θ is a measure of the angle between the incident beam and the scattered beam, i.e., the scattering angle. The relevant geometry is depicted in Figure 1. For conservation of energy the integration of the phase function over all solid angles is defined to equal unity;

$$\int_0^{2\pi}\int_0^{\pi}\frac{P(\cos\Theta)}{4\pi}\sin\Theta d\Theta d\phi = 1, \tag{4}$$

where ϕ is the azimuthal angle.

The phase function is usually solved analytically in terms of Legendre polynomials;

$$P(\cos\Theta) = \sum_{l=0}^{N}\omega_l P_l(\cos\Theta), \tag{5}$$

where ω_l is the expansion coefficient given by,

$$\omega_l = \frac{2l+1}{2}\int_{-1}^{1}P(\cos\Theta)P_l(\cos\Theta)d\cos\Theta, \tag{6}$$

where $l = 0, 1, ...N$.

The first moment of the phase function, referred to as the asymmetry factor, occurs when $l = 1$ and is given as,

$$g = \frac{\omega_1}{3} = \frac{1}{2}\int_{-1}^{1}P(\cos\Theta)\cos\Theta d\cos\Theta. \tag{7}$$

The asymmetry factor is a parameterization of the inhomogeneity of the dispersion of the scattered energy onto a sphere. It is equal to -1 for complete backscattering off the particle (scattering at 180°) and equal to +1 for complete forward scattering (scattering at 0°). Isotropic and Rayleigh scatterers, which scatter symmetrically about the sphere,

yield $g = 0$.

A general form representing directionally scattered intensity in terms of the phase function, valid for all size parameters, can then be written as,

$$I(\Theta) = I_0 \frac{\sigma_s}{r^2} \frac{P(\Theta)}{4\pi}. \tag{8}$$

Here I is the intensity and r is the distance between the molecule and the point of observation.

Rayleigh Scattering When unpolarized light is incident on a particle with size much smaller than the wavelength, i.e., when the size parameter x is $\ll 1$, scattering is described by the formulation of Rayleigh. The specific form of the scattering function given in Eqn. 8 becomes,

$$I = \frac{I_0}{r^2} \alpha_p^2 \left(\frac{2\pi}{\lambda}\right)^4 \frac{1 + \cos^2 \Theta}{2}. \tag{9}$$

For Rayleigh scatterers the scattered intensity is inversely proportional to λ^4, such that scattering increases with decreasing wavelength and is therefore stronger in the UV than in the visible spectrum.

Lorenz-Mie Scattering When the size of the particle is large compared to the wavelength, i.e., for $x \gtrsim 1$, the scattering theory of Lorenz-Mie must be used. Although it still assumes spherical particles, this is a more fundamental theory, derived directly from Maxwell's equations and encompasses that of the Rayleigh formulation. In order to write the specific Mie form of the general scattering equation expressions for σ_s and $P(\Theta)$ are needed.

In Mie theory the scattering efficiency is defined in terms of the scattering cross

section as a series expansion;

$$\frac{\sigma_s}{\pi a^2} = Q_s = c_1 x^4 (1 + c_2 x^2 + c_3 x^4 + ...), \tag{10}$$

where c_1, c_2, c_3 are coefficients expressed as functions of the refractive indices of the particles, x is the size parameter and Q_s is the scattering efficiency. When the size parameter is small the expansion collapses to the first term which represents Rayleigh scattering. As the size parameter increases the subsequent terms provide greater contributions to the scattering efficiency.

In Mie theory the phase function, $P(\Theta)$, is transformed into a phase matrix, which has 4 independent elements in the case of a single sphere, but has 16 elements in general.

ii. Absorption Absorption of EM energy is dependent mainly on the wavelength of the incident light and the atomic and molecular structure of the absorber. In general, molecules can obtain vibrational and rotational excited states which become increasingly numerous and complex as both the number of atoms forming the molecule and the number of asymmetries in the electric charges increase. Also atoms and molecules can become ionized or dissociated as a result of the absorption of EM energy. The absorption coefficient, defined by,

$$k_{a,\nu} = \sigma_a n_0(z) = S f(\nu - \nu_0), \tag{11}$$

is a function of the absorption line strength S and the line shape as a function of the wavenumber ν Stephens (1994). Absorption of EM energy leads to blackbody emission, a concept which will be considered only briefly in the following section.

iii. Radiative Transfer Equation The most general form of the radiative transfer equation states that the decrease in monochromatic intensity upon transmission through a

layer is proportional to the product of the initial intensity at that wavelength, I_λ, the monochromatic mass extinction cross section, $\eta_{e,\lambda}$, the density of the medium, ρ, and the thickness of the layer, ds;

$$dI_\lambda = -\eta_{e,\lambda}\, \rho\, I_\lambda\, ds. \tag{12}$$

The introduction of scattering into the system allows the intensity of the beam to be enhanced by scattering from other layers. Likewise, if emission is taken into account, further enhancement of the beam takes place according to Planck's blackbody radiation law. These processes are represented in a general term called the source function, J_λ, which allows the general radiative transfer equation to be written as,

$$\frac{dI_\lambda}{\eta_{e,\lambda}\, \rho\, ds} = -I_\lambda + J_\lambda. \tag{13}$$

Applying the definition of the extinction coefficient, k_e, allows the basic equation to be rexpressed as,

$$\frac{dI_\lambda}{k_{e,\lambda}\, ds} = -I_\lambda + J_\lambda. \tag{14}$$

No coordinate system has been applied to the previous two equations. If the plane parallel atmosphere is adopted such that parameters are only allowed to vary in the vertical direction then it is convenient to measure linear distances normal to the plane of stratification, i.e., normal to the surface. In this case the solar zenith angle is represented by θ, the azimuthal angle is represented by ϕ and the altitude by z, as depicted in Figure 2. The total atmospheric optical depth, τ, is defined as the mass extinction cross section times the particle density, i.e., the extinction coefficient, integrated over the depth of the atmosphere;

$$\tau = \int_z^\infty \eta_{e,\lambda}\, \rho\, dz' = \int_z^\infty k_e\, dz'. \tag{15}$$

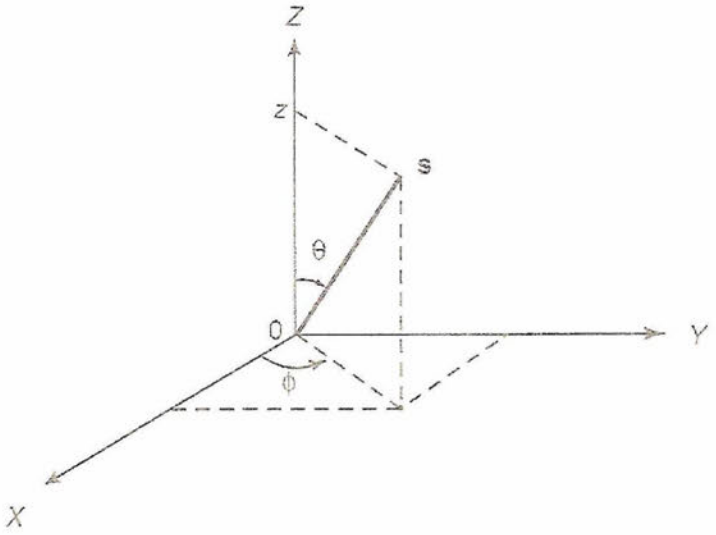

Figure 2: Coordinate system introduced during the plane-parallel approximation. Solar zenith angle given by θ, azimuthal angle given by ϕ and altitude given by z. Taken from Liou (2002).

Letting μ represent $\cos\theta$, the basic radiative transfer equation can be stated as,

$$\mu \frac{dI(\tau;\mu,\phi)}{d\tau} = I(\tau;\mu,\phi) - J(\tau;\mu,\phi). \tag{16}$$

This equation can be solved separately for the upward and downward intensities at any level τ by appropriate assignment of the sign of μ as well as for the limits of integration.

The treatment of radiative transfer can be considered as the sum of a direct and a diffuse component, i.e., unscattered and scattered components. In radiative transfer code, such as the TUV model used in this research, the direct and diffuse radiances are calculated separately at each altitude grid point and for each wavelength as defined by the user. The radiances $[W/(m^2 * nm * sr)]$ are then converted to monochromatic flux densities, i.e., irradiances in $[W/(m^2 nm)]$. Only the surface irradiances are considered in this research, although the TUV model has the ability to calculate flux densities as well as actinic fluxes at each level.

Direct Component For the direct component of radiation, scattering and emission processes are not considered. Solving the differential radiative transfer equation (Eqn. 16) by ignoring the source term, J, and using separation of variables yields the Beer-Lambert extinction law. This law states that the intensity of the direct component of radiation as it passes through an absorbing medium decays exponentially with the optical depth of the material;

$$I_\lambda = I_{\lambda 0}\, e^{-\tau m} \tag{17}$$

where $I_{\lambda 0}$ is the monochromatic solar radiance at the top of the atmosphere, $m = \sec\theta$ is the air mass and τ is the optical depth.

Diffuse Component The diffuse component of the radiation is more complicated than the direct due to scattering and absorption-emission considerations. Note that although the diffuse component should not be thought of in terms of a beam, the nomenclature direct and diffuse "beam" are sometimes used in this research for convenience. The diffuse component is composed of 4 terms; 1.) reduction from the extinction attenuation as for the direct beam, 2.) increase from multiple scattering of the diffuse beam from directions (μ', ϕ') to the direction of propagation (μ, ϕ), 3.) increase from the single scattering of the direct beam from the direction $(-\mu_0, \phi_0)$ to (μ, ϕ) and 4.) increase from emission within the layer. The appropriate geometry is depicted in Figure 3. The form of the radiative transfer equation is again;

$$\mu \frac{dI(\tau;\mu,\phi)}{d\tau} = I(\tau;\mu,\phi) - J(\tau;\mu,\phi), \tag{18}$$

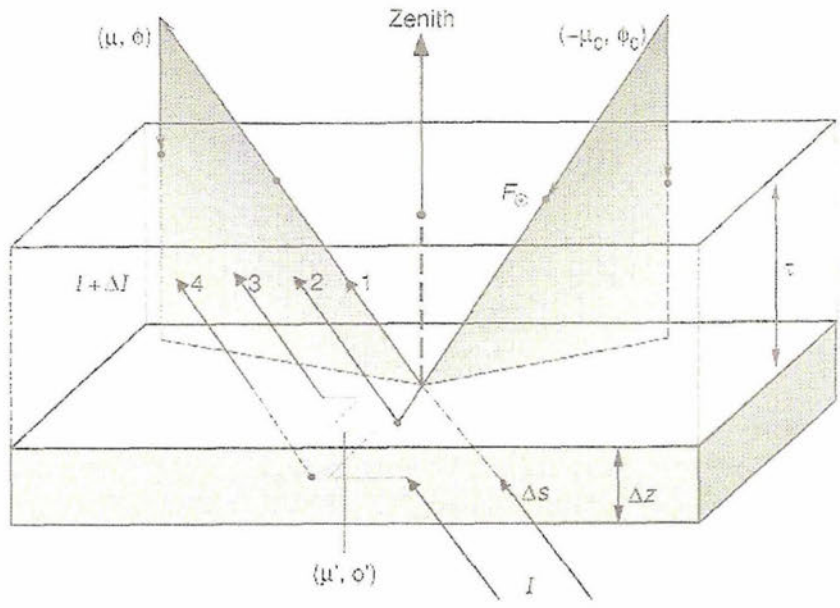

Figure 3: Geometry for the diffuse component of radiation. Taken from Liou (2002).

where the source function is comprised of terms 2.) through 4.), given above, and is written as,

$$J(\tau;\mu,\phi) = \frac{\beta}{4\pi}\int_0^{2\pi}\int_{-1}^{1} I(\tau;\mu',\phi')\; P(\mu,\phi;\mu',\phi')\; d\mu'\; d\phi'$$
$$+\frac{\beta}{4\pi}F_\odot\; P(\mu,\phi;-\mu_0,\phi_0)\; e^{-\tau/\mu_0} + (1-\beta)\; B[T(\tau)].$$

Here β is the single scattering albedo given by the ratio of the scattering to the extinction coefficient. More discussion of single scattering albedo will follow in the next chapter.

Net Flux Density Fluxes are obtained by integrating radiances over solid angle, or, in our current coordinate system, over all μ. The direct beam contains only a downward propagating component, while the diffuse beam contains both downward and upward components. The total upward flux is due solely to the upward component of the diffuse term as,

$$F^{\uparrow}(\tau) = F^{\uparrow}_{dif}(\tau) = 2\pi\int_0^1 I(\tau,\mu)\;\mu\; d\mu, \tag{19}$$

while the downward flux is given by the sum of the downward diffuse component and the direct beam;

$$F^{\downarrow}(\tau) = F^{\downarrow}_{dif}(\tau) + F^{\downarrow}_{dir}(\tau) = 2\pi \int_0^{-1} I(\tau, \mu)\, \mu\, d\mu + \mu_0\, F_{\odot}\, e^{-\tau/\mu_0}. \qquad (20)$$

The net flux at any given level is simply given as the difference in upward and downward fluxes;

$$F(\tau) = F^{\downarrow}(\tau) - F^{\uparrow}(\tau). \qquad (21)$$

As can be deduced from the preceding discussion, the diffuse beam is enhanced relative to the direct beam as the scattering properties of the atmosphere are increased. As discussed by Lorente *et al.*, the diffuse beam comprises about 50% of the total irradiance in the UV spectrum at small solar zenith angles and increases with both increasing air mass and turbidity to close to 100% diffuse under extreme conditions Lorente et al. (1994). The direct-to-diffuse irradiance ratio (DDR) in a cloud-free sky in the UV is therefore an important measurement of the scattering properties of the local atmosphere, and can be used to determine aerosol single scattering albedo when coupled with a radiative transfer model, as was done by Petters *et al.* Petters et al. (2003). The DDR at any particular latitude has an annual dependence on the solar elevation due to shortening in the photon path lengths of the scattered beam at large solar zenith angles (near the horizon). This yields smaller DDR values in the winter months relative to those in the summer months given the same atmospheric scattering conditions WHO (1994).

2b. *The UV Spectrum and the Primary Attenuators*

The total solar spectrum spans a wavelength interval from about 10^{-5} μm (gamma rays) to 10^{9} μm (radio waves). As can be inferred from a plot of irradiance versus wavelength, as shown in Figure 4, about 50% of the solar irradiance comes from radiation with wave-

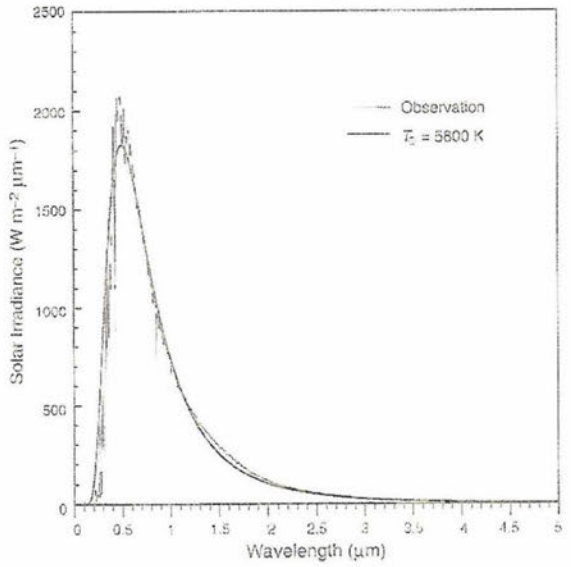

Figure 4: Solar irradiance plotted against wavelength. Taken from Liou (2002).

lengths greater than visible (>1 μm), about 40% is from the visible spectrum, while the remaining 10% is from wavelengths shorter than the visible. Of the wavelengths shorter than visible the Ultra-Violet (UV) region is of critical importance to the climate system.

The UV spectrum spans approximately 10-nm to 400-nm (0.010 μm to 0.40 μm) and is commonly subdivided into the ranges UV-A (400- to 320-nm), UV-B (320- to 280-nm) and UV-C (<280-nm). Although the UV spectral range comprises only about 1.5% and 0.5% of the total extraterrestrial and surface spectra, respectively Frederick et al. (1989), it bears great importance for the overall climate of the earth system due to its interaction with atmospheric constituents as well as biological entities. Figure 5 shows a plot of the altitude at which the UV as a function of wavelength is extincted by a factor of 1/e, i.e., unit optical depth. From this curve it can be deduced that a ground based instrument will not be able to measure UV at wavelengths much shorter than 300-nm (3000 Å) due to the extremely strong extinction in the atmosphere by atomic oxygen and nitrogen (O and N), molecular oxygen and nitrogen (O_2 and N_2) as well as ozone (O_3). These gases, which are abundant in the atmosphere above 10km, absorb a great portion of the incoming UV providing most of the energy in the upper atmosphere Liou (2002).

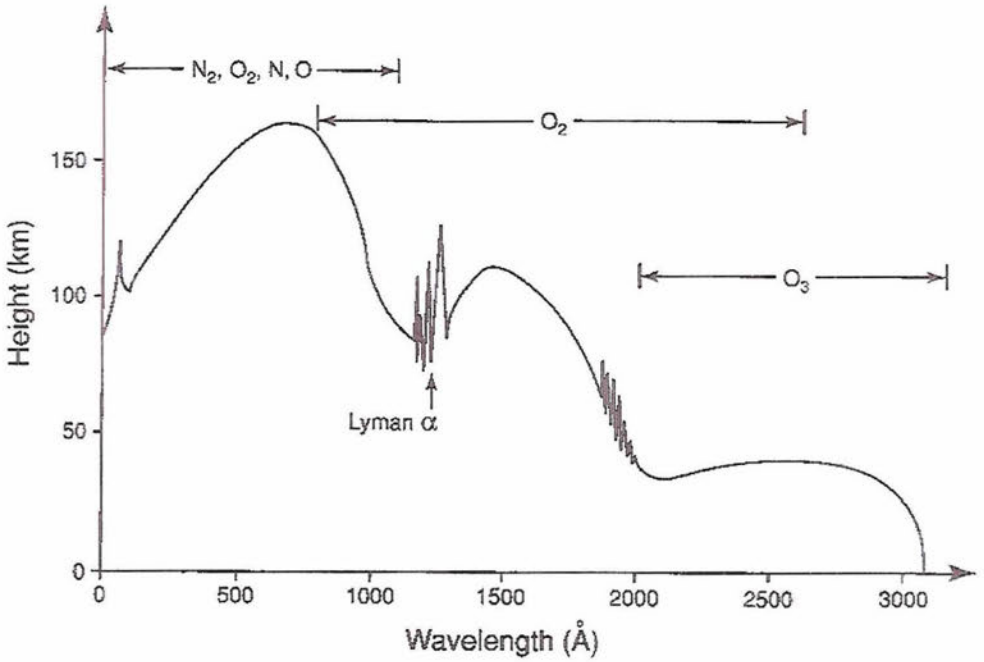

Figure 5: Altitude of unit optical depth versus wavelength in the UV spectral range. The dominant atmospheric absorbers for three wavelength intervals are indicated above the plot. Taken from Liou (2002).

The remaining atmospheric constituents which are significant attenuators of UV in the earth's atmosphere are trace gases, water vapor, cloud and aerosol. These components all have much higher variabilities, both spatially and temporally, than do oxygen, nitrogen and ozone.

i. UV Extinction by Air Molecular nitrogen (N_2) and oxygen (O_2) compose 78% and 21%, respectively, of the total number of molecules present in the earth's atmosphere. Both gases are distributed extremely homogeneously in the earth's atmosphere and therefore do not need to be routinely measured. They are normally represented in radiative transfer models using a standard vertical profile distribution, as is the case for the TUV model.

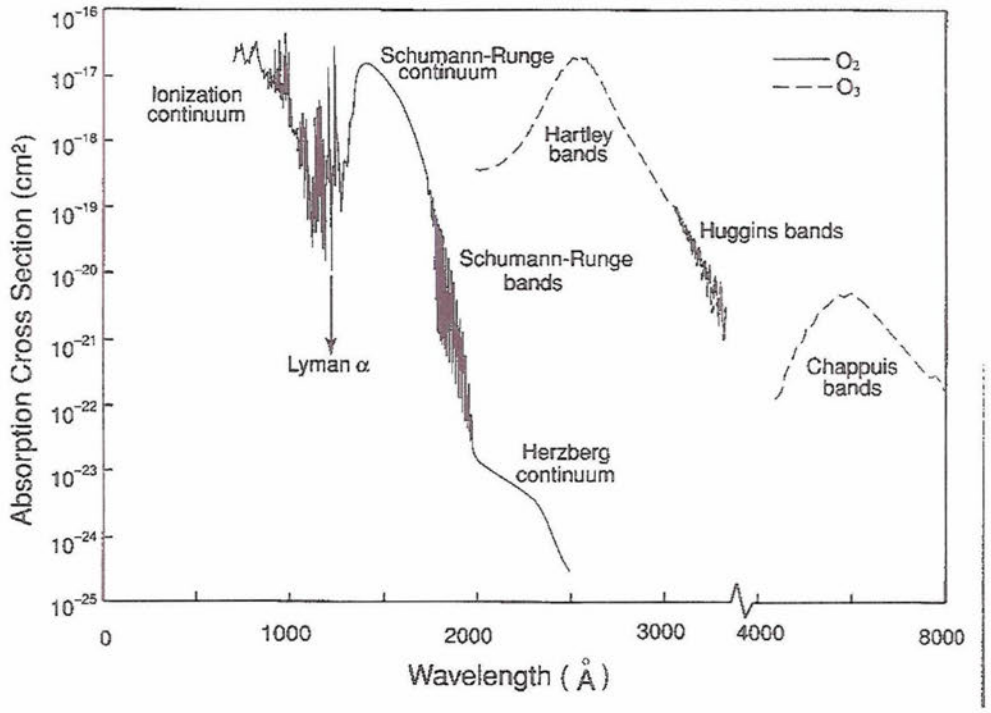

Figure 6: Absorption cross sections versus wavelength in the UV spectral range for oxygen and ozone. Taken from Liou (2002).

Scattering N_2 and O_2 act as Rayleigh scatters in the UV spectral range due to their small size. The Rayleigh scattering cross section is about $2\text{x}10^{-25}cm^2$ at 300-nm and is about $3\text{x}10^{-22}cm^2$ at 50-nm Huffman (1992), which, when compared to the absorption cross sections plotted in Figure 6 indicate that Rayleigh scattering is about 8 orders of magnitude smaller than ozone absorption at 300-nm and about 5 orders smaller than absorption by oxygen at 50-nm. However little ozone exists relative to N_2 and O_2 high in the atmosphere, as can be determined from the mixing ratios as a function of altitude plotted in Figure 7. This allows the scattering process to dominate at the upper reaches of the atmosphere. Recall that Rayleigh scattering increases as $1/\lambda^4$. Between 200- and 400-nm Rayleigh scattering is the dominant radiance source for satellite measurements and it is this backscattering that is used for ozone retrievals from space Huffman (1992).

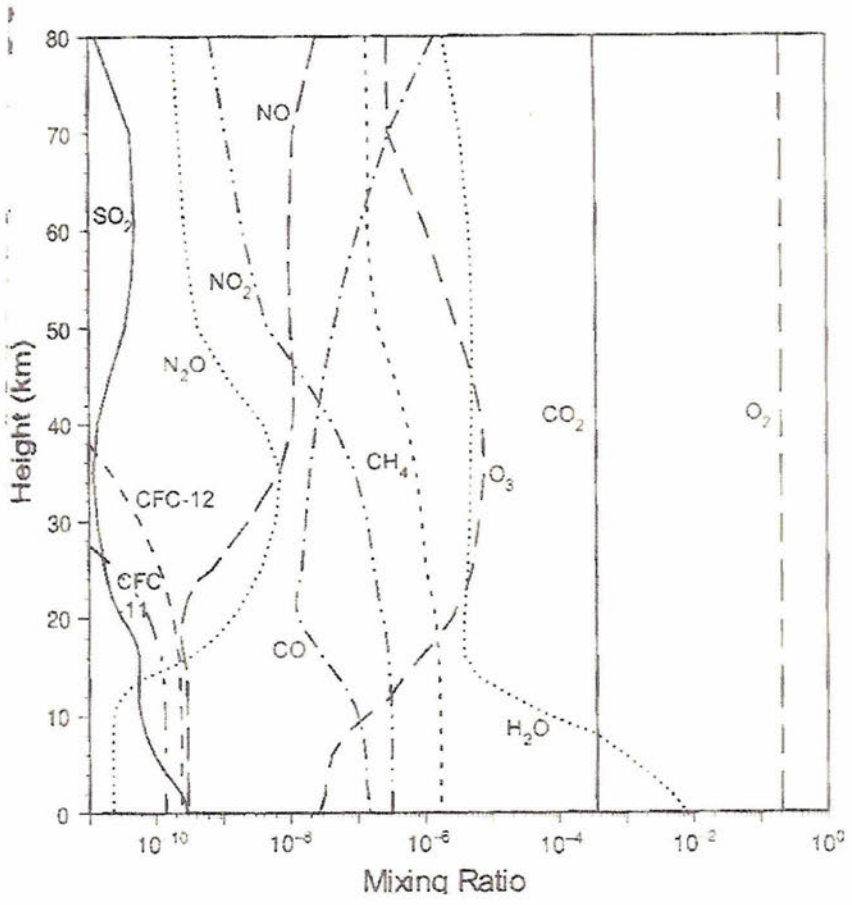

Figure 7: Mixing ratios of various atmospheric gases versus altitude. Taken from Liou (2002).

Absorption Absorption by N_2 is generally considered insignificant in the entire solar range, although photodissociation of these molecules into atomic nitrogen plays a minor role in atmospheric chemistry and can also lead to significant UV absorption in the thermosphere Liou (2002) and is partially responsible for the formation of the ionosphere Wallace and Hobbs (1977).

UV radiation in the wavelength band 100- to 200-nm is absorbed during the dissociation of oxygen molecules in the upper atmosphere as indicated by the solid line plotted

in Figure 6 and the altitude profile shown in Figure 5. The process is represented as,

$$O_2 + h\tilde{\nu} \longrightarrow 2O, \tag{22}$$

which plays a vital role in the formation of ozone, as will be discussed in the following section. Atomic oxygen absorbs UV between 1- and 100-nm at altitudes above about 50 to 60km in the reaction,

$$O + O + M \longrightarrow O_2 + M, \tag{23}$$

where M is a third atom or molecule which serves as a sink for the released energy.

ii. UV Extinction by Ozone

Stratospheric Ozone Figure 6 shows absorption cross sections of O_3 as a function of wavelength plotted as dashed lines. At wavelengths between about 200- and 300-nm extinction of the UV is dominated by the presence of ozone in the Hartley absorption bands, which have a peak absorption cross section of about $10^{-17} cm^2$ centered at 255.3-nm. The Huggins bands contain much greater spectral features and have absorption cross sections ranging from about 10^{-19} at 300-nm to about 10^{-21} at 360-nm. Note that this is the range of wavelengths used by the UV-MFRSR instrument, from which the data used in this research was obtained.

When atomic oxygen atoms, (O), produced via photodissociation (Eqn. 22), are involved in a 3-body collision with both molecular oxygen, (O_2), and some other molecule, (M), which absorbs the excess energy, the result is the formation of ozone (O_3). This reaction is given by the expression;

$$O_2 + O + M \longrightarrow O_3 + M. \tag{24}$$

The likelihood of this reaction occurring increases with increasing air density, which produces a maximum in the lower stratosphere as seen in the mixing ratio profiles plotted in Figure 7.

There are two ozone destruction reactions that occur naturally in the atmosphere. The first is given by,

$$O_3 + h\tilde{\nu} \longrightarrow O_2 + O, \tag{25}$$

where $h\tilde{\nu}$ represents the energy of an incident photon with a UV wavelength in the range of approximately 200- to 360-nm. The second reaction is given by,

$$O_3 + O \longrightarrow 2O_2. \tag{26}$$

The five reactions given by Eqns 22, 23, 24, 25 and 26 cause no net change in the chemical state of the atmosphere from the established equilibrium, but allow for virtually complete absorption of UV radiation in the range 10- to 300-nm Wallace and Hobbs (1977). The absorption of UV from 300- to 360-nm, the approximate wavelength interval of the UV-MFRSR instrument, falls off exponentially by approximately several orders of magnitude. This phenomenon provides information from the UV-MFRSR measurements which allows for the determination of total ozone column.

Tropospheric Ozone In the troposphere, where nitrogen dioxide (NO_2) is abundant, as can be seen from the mixing ratio profiles in Figure 7, atomic oxygen is generated from the dissociation reaction,

$$NO_2 + h\tilde{\nu} \longrightarrow NO + O, \tag{27}$$

where the incident wavelength must be less than about 424-nm. This provides the free oxygen atom which allows ozone to form via the reaction in Eqn. 24. The O_3 molecules

then recombine with NO molecules in the reaction,

$$O_3 + NO \longrightarrow NO_2 + O_2. \tag{28}$$

This process occurs at a non-linear, steady state rate with $[O_3]_{SS} \propto \sqrt{[NO_2]_0}$, where $[O_3]_{SS}$ represents the steady state formation of ozone and $[NO_2]_0$ represents the initial quantity of nitrogen dioxide. For example, given an initial state of 100ppb NO_2, tropospheric ozone will reach an equilibrium amount of 27ppb, whereas for an initial state of 1000ppb NO_2, tropospheric ozone will equilibrate at 95ppb Seinfeld and Pandis (1998).

At large solar zenith angles (SZA) the solar UV absorption due to tropospheric ozone can match that due to the stratospheric component due to the increased average path length of the scattered beam Bruhl and Crutzen (1989). In radiative transfer models, such as TUV, ozone is assigned a total column amount and a vertical profile, to which the column amount is scaled.

iii. UV Extinction by Other Trace Gases The two trace gases that are most commonly treated in UV applications are nitrogen dioxide, NO_2 and sulfur dioxide, SO_2. Both of these molecules compose about $1x10^{-7}$ percent by volume in the earth's atmosphere and are disseminated heterogeneously throughout. Although these two compounds interact only mildly with UV radiation compared to ozone and oxygen, they play vital roles in the chemistry of the troposphere. In radiative transfer models, such as TUV, NO_2 and SO_2 are assigned both total column amounts and vertical profiles, to which the column amounts are scaled. However, research has shown that UV models typically have low sensitivity to these two parameters under normal atmospheric conditions Schwander et al. (1997).

The mixing ratio of NO_2 is about an order of magnitude larger than that of ozone at the midlatitude surface as inferred from the mixing ratio profiles in Figure 7. The

absorption cross section peaks at about $10^{-19} cm^2$, which is approximately equivalent to the magnitude of the absorption coefficients in the Schumann-Runge oxygen absorption bands at 200-nm and the Huggins ozone bands at about 350-nm as see in Figure 6. Nitrogen dioxide is important in a number of catalytic cycles, especially as the only *in situ* chemical source of tropospheric ozone Seinfeld and Pandis (1998) as discussed in the preceding section. Laboratory measurements of temperature dependencies in the fine structure of the NO_2 spectrum in the UV spectral range have been made Harwood and Jones (1994).

Of all the sulfur containing compounds present in the earth's atmosphere, sulfur dioxide is by far the most prevalent, with mixing ratios ranging from about 20 to 50 ppt (parts per trillion) in the clean marine boundary layer all the way to several hundred ppb (parts per billion) in highly polluted continental air. The leading source of SO_2 is from fossil-fuel combustion and industry, estimated to produce 70 Terra grams of sulfur per year ($70x10^9$kg/yr) out of a total estimated 73-80 Tg/yr of anthropologically produced sulfur. This is in contrast to about 2.8 Tg/yr of sulfur from biomass burning and 7 to 8 Tg/yr from volcanoes Seinfeld and Pandis (1998).

iv. The Influence of Water Vapor on UV and Extinction by Clouds Water vapor exists mainly in the lower half of the troposphere, as seen in the mixing ratio profiles in Figure 7. The spatial distribution is highly variable in time and driven by the large scale circulation coupled with convective activity. Although water vapor is highly optically active with respect to the visible and infrared wavelengths, its effect on UV wavelengths is not discussed in current literature, and is assumed to be negligible. However, it has been shown that the absorption properties of aerosols are highly dependent on the relative humidity Im et al. (2001), making water vapor indirectly an important factor in UV radiation studies. In radiative transfer studies, such as this one, water vapor is normally

represented by some fixed vertical profile of humidity.

In general, clouds cause attenuation of radiation (decreased transmittance) at all solar wavelengths. The effect has been shown to be wavelength dependent in the UV region Kylling et al. (1997). It has also been shown that cloudy conditions can lead to the enhancement of UV radiation by increasing the upward flux, which, in turn, can be backscattered in the downward direction Frederick and Lubin (1988). Although cloud cover is very heterogeneous and has a short time scale variation, the problems associated with this can be minimized by applying a cloud screening algorithm to the data set. The cloud screening algorithm of Smirnov *et al.* uses a series of tests contingent on the standard deviation and temporal consistency of AOD_{500-nm} Smirnov et al. (2000). Note that the use of precalculated AOD to perform cloud screening is somewhat circular, as it applies to this research, since AOD is a parameter to be estimated by the retrieval code. Other algorithms are available which do not require precalculated AOD, such as that of Long and Ackerman Long and Ackerman (2000), however this cloud screening algorithm requires ancillary data from a broadband meter as well as synchronization with the data collected from the UV-MFRSR. Currently the Smirnov *et al.* algorithm, modified to operate on AOD_{368-nm} provided by the UVMRP, has been employed for cloud screening of the irradiance data set.

v. UV Extinction by Aerosol In the past decade a substantial number of papers have been published concerning the effects of aerosols on the transmission of UV using both measurements and models. Lorente *et al.* measured spectral UV irradiances for varying atmospheric conditions in the urban center of Barcelona, Spain. Their results showed that the difference in the UV transmission between a clear and turbid day can be as great as about 50% due to the presence of aerosols, compared to changes of only about 9% in the visible and IR Lorente et al. (1994). Furthermore they showed an increase in the diffuse

component of the UV radiation with increasing turbidity, as should be expected due to scattering. The change in the diffuse component with changes in turbidity had varying wavelength dependence, explained by increased scattering due to increased water vapor during high turbidity conditions, which is less wavelength dependent than that caused by Rayleigh scattering during low turbidity conditions.

Another study, performed by Kylling *et al.* using irradiances modeled via the discrete ordinate method with and without an aerosol layer, showed that the transmittances in the UV-B spectral interval decreased by between 5% and 35% due to the aerosol layer. The effect in the UV-A spectral region was smaller by about 5% Kylling et al. (1998).

These results point to the high sensitivity of the UV radiation in the atmosphere to changes in aerosol conditions and indicate a need for establishing a climatology of aerosol optical properties in the UV. Since the spatial distribution of aerosol quantity and composition is highly irregular, a climatology covering as large a spatial extent as possible is desirable. Once a climatology is established, the aerosol properties can be used as inputs into radiative transfer models which theoretically can be used to simulate UV irradiances over global extent. The issue of UV extinction by aerosols is treated more completely in the following section, including some of the previous research which has focused on this topic.

2c. *Aerosol Properties in the Ultra-Violet Spectral Range*

The critical component of solar UV extinction which is the focus of this research is the aerosol. As mentioned previously, aerosols are defined as a suspension of fine solid or liquid particles in a gas, and can range from a few nanometers (nm) to tens of micrometers (μm) in diameter Seinfeld and Pandis (1998). Given this broad definition, many distinct aerosol categorizations can be made, including dusts, fogs, fumes, hazes, mists, smogs, smokes and soots. These are based on the phases of the particles as well as the

chemical combinations and particle sizes. Due to the efficient removal of aerosols from the troposphere via wet and dry deposition, residence times are on the order of days and weeks, while stratospheric aerosols, especially those produced by volcanoes, have residence times on the order of months and years.

The key role of aerosols in the earth's atmosphere is that they serve as cloud condensation nuclei (CCN). The water soluble mass in aerosols allows supersaturated air to condense on the surface of the particle, a process that occurs rapidly once a critical threshold is reached. Precipitation processes occur as a direct result of clouds, which allows for the washout of the aerosol particles which initially served as CCN. This is the major source of aerosol removal from the atmosphere. As discussed in the introductory chapter, changes in aerosol properties and abundances, through either natural or man-made processes, cause changes in solar radiation transmittances as well as changes in cloud microphysical properties and precipitation processes.

The aerosol layer at any particular region during any particular time period can be characterized by a number of variables describing its physical, chemical and optical properties. This research is concerned exclusively with the optical nature of aerosols and the discussion will therefore be limited to the relevant properties. The quantification of optical properties of atmospheric aerosols from irradiance measurements, and the subsequent inversion via the optimal estimation retrieval, is dependent on the aerosols being optically active. This assumption allows the retrieval of optical characteristics such as AOD, SSA and g but limits the probability of successfully retrieving physical or chemical properties such as size distributions or chemical makeup for example. To obtain the non-optical properties, additional assumptions are required which completely change the characteristics and error budget of the retrieval and require different physical models. Current research is greatly simplified by not needing to consider these complexities.

i. Aerosol Optical Depth (AOD) The total atmospheric optical depth was defined in Eqn. 15. The aerosol optical depth is simply the component of the total optical depth due to extinction by aerosols. Although a form of the optical depth equation could be written specifically for AOD, with k_e replaced by an aerosol specific extinction coefficient, the common way to retrieve AOD information is by backing it out of Beer's Law in what is referred to as the Langley AOD technique.

The Langley Technique Taking the logarithm of Beer's Law (Eqn. 17) yields,

$$\ln I_\lambda = \ln I_{\lambda 0} + m\tau, \tag{29}$$

which is the equation for a straight line with slope = τ and y-intercept = $\ln I_{\lambda 0}$. A series of measurements made at varying air masses can be plotted in log space to yield a best-fit line, allowing approximation of total optical depth, τ, and the expected TOA radiances, $\ln I_{\lambda 0}$.

The total optical depth in the UV spectrum can be expressed as the sum of the optical depths of the various atmospheric absorbers present,

$$\tau_{total} = \tau_{Rayleigh} + \tau_{O_3} + \tau_{trace} + \tau_{aerosol}. \tag{30}$$

Combining Eqns. 29 and 30 the aerosol optical depth (AOD) can then be expressed as,

$$AOD = \tau_{aerosol} = m \ln \frac{I}{I_0} - \tau_{Rayleigh} - \tau_{O_3} - \tau_{trace}. \tag{31}$$

The monochromatic Rayleigh optical depth is given by,

$$\tau_{Rayleigh} = -\beta_\lambda m \frac{p}{p_0}, \tag{32}$$

where p/p_0 is the ratio of the station pressure to the mean sea level pressure. The β_λ term can be parameterized as a function of the wavelength and the local elevation, z, (Stephens (1994)) as,

$$\beta_\lambda = 0.0088\lambda^{-4.15+0.2\lambda} \exp\left[-0.118z - 0.00116z^2\right], \tag{33}$$

The ozone optical depth is given by,

$$\tau_{O_3} = -\alpha_\lambda \Omega \mu, \tag{34}$$

where α_λ are the wavelength dependent ozone absorption coefficients, Ω is the total ozone column (TOC) and μ is the air mass Gao et al. (2001).

Previous Work The UV-MFRSR measures voltages, V, which are then converted into irradiances, F. Voltages can be substituted for radiances, I, in Beer's Law (Eqn. 17) with no change in the functional form. This technique has been employed by the UVMRP to produce values of AOD at the 7 UV channels of the UV-MFRSR instrument (Slusser et al. (2000)) following the algorithm described by Harrison *et al.* Harrison and Michalsky (1994). Comparisons between UVMRP derived and optimal estimation derived AOD values will be presented in Chapter 6, which discusses the results of this research.

Wenny *et al.* used the Langley technique to determine AOD for a 6-month period in 1999 at a site in the Blue Ridge Mountains of North Carolina Wenny et al. (2001). The retrieved values of AOD_{332-nm} showed a distinct seasonal dependence (refer to Fig. 3 in Wenny et al. (2001)), with higher mean AOD in July (≈ 0.7) and August (≈ 0.65) than in September (≈ 0.25), October (≈ 0.2) and November/December (≈ 0.15). They then used the AOD as inputs into the TUV model for cloud free days to calculate UV Index (UVI) values for comparison with those produced by the National Weather Service (NWS).

At the time of that research the NWS was using a fixed, wavelength independent AOD value of 0.2 as well as a non-absorbing aerosol assumption ($\omega = 1.0$; this parameter, the aerosol single scattering albedo, will be discussed in Section ii) to forecast UVI at major cities across the United States. The results indicated that for relatively high AOD (AOD $\approx$1) the NWS is overestimating the UVI by about 12%, 20% and 36%, depending on the model assumed aerosol absorbing properties, i.e., for ω = 1.0, 0.90 and 0.75, respectively.

The Langley technique was also employed by Wetzel *et al.* using a UV-MFRSR at the Poker Flat Research Range in central Alaska (65.12°N, 147.43°W), to retrieve AOD during August 2000. The values of AOD were analyzed as a function of air mass type, which were determined from ancillary measurements of size-resolved aerosol chemical composition and concentrations as well as profiling of aerosol size distributions and atmospheric state variables. The AOD_{368-nm} ranged from 0.05 to 0.06 for summer and spring arctic air, 0.11 to 0.14 for a spring Asian air mass and 0.15 to 0.25 for spring maritime air. These AOD values are low relative to those obtained by Wenny *et al.* in North Carolina, as should be expected for a remote site in Alaska.

Total uncertainty budget Uncertainties can be calculated for Langley derived AOD values based on the uncertainties in the terms on the right hand side of Eqn. 31 (with V substituted for I). The first term has uncertainties given by the standard error of the mean in the Langley calculated V_0 value ($\Delta V_0 \approx \sigma_V \div \sqrt{N_V}$) Wenny et al. (2001), the estimated error in the measured voltage V and the estimated error in the air mass factor.

The second term on the RHS of Eqn. 31 is given by Eqn. 32, which has uncertainty associated with the finite bandpass of the instrument and uncertainty in the approximate elevation of the instrument site used in the parameterization equation (Eqn. 33). There are also uncertainties associated with the air mass factor and station pressure.

The third term on the RHS of Eqn. 31, the ozone term, has uncertainties associated with the error in the ozone absorption coefficients, α_λ, error in the total column ozone,

Ω, and error in the calculated air mass, m. Since the value for Ω used in calculating the AOD was obtained from the direct sun technique of Gao *et al.* Gao et al. (2001), and their error budget for Ω included the uncertainty due to measurement error of the ozone absorption coefficients, α_λ, only the uncertainty in Ω ($\pm 2\%$) needs to be used.

The final term on the RHS of Eqn. 31 represents the contribution to AOD due to absorption by trace gases such as NO_2 and SO_2. As mentioned previously, model studies have indicated that the sensitivity to these parameters is small, allowing their contribution to the AOD error to be ignored.

Although Langley derived AOD uncertainties are reported in Table 2 of Petters *et al.* Petters et al. (2003) and a reference is made to the previous work performed by Wenny *et al.* Wenny et al. (2001), it is unclear exactly how they carried out their analysis. In fact some errors have been discovered in the later work which indicates that they may have in fact used some incorrect uncertainties in calculating the AOD errors. For example they report the estimated uncertainty in the ozone retrieval technique as detailed by Gao *et al.* to be $\pm 3.8\%$, when in fact the uncertainty reported by Gao *et al.* is given clearly in the article abstract and text to be $\pm 2.0\%$ Gao et al. (2001).

Abbreviated uncertainty analysis Although the above procedure should be carried out to provide a rigorous uncertainty analysis which can be applied to each measured set of irradiances, an abbreviated analysis was used to estimate error bars for the Langley derived AOD values presented in this research. The total optical depth for a high turbidity (noon on May 12, 2003 at Panther Junction) and low turbidity (noon on May 22, 2003 at Panther Junction) condition was obtained from the UVMRP web site, along with the corresponding Langley derived voltage intercept, V_0=2.100, V_0 uncertainty, σV_0=0.107 and number of points used to calculate V_0, NV_0=180. These later 3 values were the same for both days May 12 and 22. The uncertainty in V_0 was calculated using the standard error of the mean in the Langley calculated V_0 value, ϵ=0.00798. The measured voltages

from the UV-MFRSR were then estimated from Eqn. 29. Next, the uncertainty in AOD was calculated by perturbing the first term on the RHS of Eqn. 31 for both instrument error and calculated V_0 error. The root mean square of these two contributions was used to calculate the total uncertainty in AOD. The error in the measured V was taken to be 3% from Table 1 of Krotkov *et al.* Krotkov et al. (2005), while the error due to air mass calculation in this term was ignored. Contributions to the calculated AOD uncertainty from the Rayleigh, ozone and trace gas terms were also ignored.

The values of τ, m, calculated V, AOD_{368-nm}, ΔAOD_V, ΔAOD_{V_0}, Δ AOD, and $\%\Delta$ AOD are given in Table 1 for the noon-time scan on these two days. The estimated error for high turbidity (AOD_{368-nm} = 1.028) was calculated to be ± 0.133 or 12.9%, while for the low turbidity condition (AOD_{368-nm} = 0.280) the estimated error was calculated to be ± 0.077 or 27.62%. The contribution from the assumed 3% uncertainty in the measurement, ΔAOD_V, dominated the total error. The results from Petters *et al.* indicate an error of ± 0.037 for AOD_{368-nm} due to V_0. This is about twice the estimated error for the V_0 contribution, using the method described here for the high turbidity case. The estimated error in V_0 for the low turbidity case was found to be about one third that determined by Petters *et al.*. Note that the estimated percent error in Langley derived AOD decreases with increasing AOD. It will be shown in the discussion of the results that this is opposite to the AOD dependence in the error from the optimal estimation retrieval.

ii. Aerosol Single Scattering Albedo (SSA) Aerosol single scattering albedo (SSA) is defined as the ratio of the aerosol scattering coefficient to that of the aerosol extinction coefficient;

$$SSA = \omega = \frac{k_{s(aerosol)}}{k_{e(aerosol)}}. \tag{35}$$

Table 1: **Values used in estimating the Langley derived AOD errors for the noon-time case.**

Day	May 12	May 22
τ	1.506	0.757
m	1.0404	1.0332
V	0.4383	0.9606
AOD_{368-nm}	1.028	0.280
ΔAOD_V	$\pm$0.132	$\pm$0.077
ΔAOD_{V_0}	$\pm$0.017	$\pm$0.010
ΔAOD	$\pm$0.133	$\pm$0.077
$\%\Delta AOD$	$\pm$12.9%	$\pm$27.6%

By this definition, if an aerosol absorbs all incident radiation ω=0, while for particles which scatter all incident radiation ω=1. Real atmospheres have SSA values ranging between these extremes, depending on the scattering and absorption characteristics of the particles.

Wenny *et al.* describe a four step iterative method for determining SSA employing a Mie code, a radiative transfer code and measurements of aerosol size distributions Wenny et al. (1998). First lognormal parameters derived from the measured size distributions, along with a first guess of the aerosol refractive index, are used as input into the Mie code. Second, the Mie code calculations provide first guess estimates of the asymmetry factor and SSA_{312-nm}. Third, these values are input into the UV-B radiative transfer code, which is iterated with varying values of SSA until the modeled transmission through the layer matches the transmission measured by an instrument. The final step is then to run the Mie code with varying values of the complex index of refraction (real component held fixed) until the resulting SSA matches that from the UV-B radiative transfer code iterations. The results from 9 days in 1995 at two research stations in North Carolina indicated a range of SSA_{312-nm} between 0.75 and 0.93. The results showed no dependence on air mass type, but a dependence on relative humidity was observed, with

increased scattering at larger humidity levels. They conclude that moist climates, such as the southeastern and northwestern United States, should display larger variations in SSA than arid climates, such as the Midwestern and southwestern United States.

A different technique for retrieving aerosol SSA is outlined in the Petters *et al.* study, performed at a valley site in southern Appalachia Petters et al. (2003). Their method involves iteration of a forward model, in this case TUV, with varying values of SSA while other parameters are held fixed. Iterations are performed until the direct-to-diffuse ratio (DDR) of the modeled irradiances are equivalent to those of the UV-MFRSR measurements. The fixed AOD values were calculated from the Langley method using the UV-MFRSR measurements, while asymmetry factor was set equal to 0.70 obtained from an average of the Wenny *et al.* results Wenny et al. (1998). Surface albedo was assumed to be 0.04 from Schwander *et al.* Schwander et al. (1997). They found SSA_{300-nm} to range from 0.65 to 0.91 and SSA_{368-nm} from 0.80 to 0.99 on cloud free days. Their values had an increasing trend with increasing wavelength and a large variation for a single wavelength due to varying air mass type. Using model calculations the SSA errors were shown to be strongly dependent on AOD. Averaged over the 7 channels SSA error increased from about ± 0.04 at AOD$\approx$1, to ± 0.63 for AOD$\approx$0.05 with the minimum threshold for a reasonable SSA retrieval deemed to be AOD=0.3. That is to say that the retrieval was considered to be of no use when the AOD was smaller than about 0.3 due to the large error in the retrieved SSA.

In the Wetzel *et al.* analysis of aerosol properties in various air masses in central Alaska SSA was retrieved via the Petters *et al.* DDR technique Wetzel et al. (2003). Their results showed that SSA_{368-nm} ranged from 0.63 for a spring Asian air mass composed of large dust particles to 0.95 for a spring maritime air mass. This supports the theory that small particles have larger scattering coefficients and hence lead to larger values of SSA. Since the minimum threshold of AOD$\approx$0.3 is higher than the majority of the reported

values of AOD at the Alaska site, it can be deduced that the DDR SSA retrieval method will not be useful for determining a background aerosol SSA climatology.

iii. Asymmetry Factor (g) As described previously in Section i, the asymmetry factor, g, as given by Eqn. 7 quantifies the directionality of the forward scattering from spherical particles. It takes on values ranging from +1 for complete forward scattering to -1 for complete backscattering, while Rayleigh scattering produces g=0.

In the Wenny *et al.* study in North Carolina retrieved values of g ranged from 0.63 to 0.76 with no correlation on air mass type Wenny et al. (1998). Their sensitivity studies showed that the UV-B radiative transfer modeled transmissions varied by only 1.5% when input values of g ranged from 0.60 to 0.80. For this reason it is common practice to use a fixed value of g in radiative transfer calculations as was done by Petters *et al.* in their retrievals of SSA described in the preceding section Petters et al. (2003). Petters *et al.* determined that the asymmetry factor was the third most important factor (after AOD and SSA) in determining the change of the DDR in model calculations.

iv. Ångstrom Exponent (α) The contribution to the total optical depth due to aerosols is referred to as a measure of the turbidity of the atmosphere. Although several definitions of turbidity exist, e.g., Linke and Volz, the formulation of Ångstrom is the most commonly used in the current literature Stephens (1994). It is given by,

$$AOD = \tau_{aerosol} = \beta_t \lambda^{-\alpha} \tag{36}$$

where β_t is the turbidity coefficient and α is the Ångstrom exponent. A value for α is determined by the ratio of AOD at two wavelengths. Positive values of α indicate decreasing AOD with increasing wavelength. The Ångstrom exponent can be tied to the aerosol size distribution, $n(r)$, using the assumption that $n(r) = c\, r^{-(\gamma-1)}$, where

r is the particle radius, γ is the slope of the straight line fit through $\log n(r)$ and c is a constant. Large values of α are representative of the presence of small aerosol particles, while smaller values indicate larger aerosol particles. Physically this dependence of α on particle size is explained by the increase in Rayleigh scattering with decreasing particle size and the $1/\lambda^4$ dependence of Rayleigh scattering.

Wenny *et al.* calculated Ångstrom exponents using both the Mie code and the UV-MFRSR measurements for nine different air masses in the Blue Ridge Mountains Wenny et al. (1998). Results from the two methods were in close agreement in five cases, with values ranging between 0.82 and 1.53 for the instrument derived values and between 0.80 and 1.85 for the Mie derived values. The remaining four cases with large disagreement were attributed to uncertainties in the aerosol size distributions used in the Mie code calculation.

Wetzel *et al.* calculated values of α for four different air mass types in their central Alaska experiment. They found that an Asian air mass composed of large dust particles had much smaller values of the Ångstrom exponent (0.06 to 0.15) than the marine, arctic and summer air masses, which had values ranging from 0.68 to 0.99 for noon-time conditions.

3. The Inverse Nature of the Retrieval Problem, Bayes Theorem and the Optimal Estimation Technique

3a. *The General Inverse Problem*

In order to define the inverse problem one must first define the forward problem. The forward problem is that of determining some extrinsic properties of a system given knowledge of intrinsic properties of that same system. For example, calculating electromagnetic properties of the atmosphere from prior knowledge of the atmospheric constituents is a form of the forward problem. Mathematically the forward problem can be expressed in the Forward Function Rodgers (2000) as,

$$\mathbf{y} = \mathbf{F}(\mathbf{x}, \mathbf{b}) + \epsilon, \tag{37}$$

where $\mathbf{y}$ is the vector of measurements, $\mathbf{F}$ is the physical process, i.e., model that converts $\mathbf{x}$ space, i.e., parameters, into $\mathbf{y}$ space, i.e., measurements. The unknown state parameters influencing the value of the measurements and which are allowed to vary in the model are contained in the vector $\mathbf{x}$, while $\mathbf{b}$ contains all parameters to which the model is sensitive but which are not allowed to vary. Finally, the measurement errors are given by ϵ.

The inverse problem is the process of deriving the state parameters, contained in $\mathbf{x}$, from the set of measurements contained in $\mathbf{y}$. This process is oftentimes referred to as retrieval or inversion theory in the general sense, or as indirect or remote sensing in the atmospheric sciences. In the atmospheric sciences the measurements are usually of electromagnetic radiation, but could be, for example, seismic waves or electric potentials.

Formally the inverse problem can be stated as,

$$\hat{\mathbf{x}} = \mathbf{R}(\mathbf{y}, \hat{\mathbf{b}}, \mathbf{x_a}, \mathbf{c}), \tag{38}$$

where circumflexes indicate estimated quantities, $\mathbf{R}$ represents the retrieval process, $\mathbf{x_a}$ represents some *a priori* knowledge of the state and $\mathbf{c}$ represents the retrieval method parameters such as convergence criteria. By substituting Eqn. 37 into Eqn. 38 the Transfer Function can be written;

$$\hat{\mathbf{x}} = \mathbf{R}(\mathbf{f}(\mathbf{x}, \mathbf{b}) + \epsilon, \hat{\mathbf{b}}, \mathbf{x_a}, \mathbf{c}), , \tag{39}$$

This function describes the entire system in terms of the measuring instrument and the retrieval method Rodgers (2000).

Mathematically inversion is the solution of a system of N equations for x unknowns, which can be accomplished using the techniques of linear algebra
Twomey (1977). However, the set of N equations does not always uniquely determine x unknowns, as the equations may be contradictory or contain insufficient information. There is another reason inversion is not as straightforward as the solution of a system of well behaved equations: the atmosphere is complex enough, as are most real physical systems that are of interest, that a one-to-one relationship does not normally exist between any two or more given variables. In this sense a one-to-one correspondence would indicate that knowing one variable leads to an unambiguous value of a second variable.

For example, in the realistic remote sensing problem of obtaining the temperature profile of the atmosphere from satellite measurements of radiances, imagine that there is a one-to-one relationship between the intensity of radiation at wavelength λ and the height h from which this radiation is emitted. Mathematically this hypothetical system could be said to have Delta contribution functions. That is, the contribution to the measured radiance for some specific λ_i derives solely from the blackbody emittance at height h_i. This problem would be trivial to solve for a profile of temperature with height. However, in the real physical system the radiation at λ_1 actually derives mostly from h_1 based on Planck's blackbody law, but due to complications in the physics, there are contributions

to λ_1 from heights other than h_1.

Although the contribution functions may have reasonably well defined peaks and decay smoothly away from the peak, the off-peak contributions cause a blurring of the delta contribution functions and eliminate the simple one-to-one correspondence among the variables. In the temperature profile example a measured radiance at λ_1 no longer uniquely determines the temperature at height h_1 due to contributions from other levels.

Mathematically we now have to deal with the integration of the product of the distribution being sought with that of the contribution function;

$$\int K_i(x)\, f(x)\, dx, \tag{40}$$

where K_i represents the contribution function at the i^{th} position and $f(x)$ represents the distribution being sought. In the temperature profile example the distribution being sought is temperature (T) as a function of height (h) and the i^{th} position is given by wavelength λ_i. This information, along with the fact that the value of the previous integral is obtained from an instrument measurement allows it to be expressed as an equation;

$$S = \int_{h=z_1}^{h=z_2} K_{\lambda_i}(h)\, T(h)\, dh, \tag{41}$$

where S is the measured signal (e.g., volts or irradiance or radiance, depending on the instrument) and integration takes place from level z_1 to level z_2. In the multivariate problem the individual contribution functions, K_i, are contained in the mxn matrix $\mathbf{K}$ which is termed the kernel or Jacobian.

Complications to the retrieval process arrive in cases where the contribution functions K_{λ_i} are no longer simple delta functions as discussed previously. In fact K_{λ_i} may take on any number of forms such as behaving in non-smooth ways away from a single maxima, or having peaks at similar heights but different shapes away from the peak, or each

having multiple maxima, etc. The job of the retrieval is to determine the best solution to the problem (a distribution of $f(x)$, or in this example $T(h)$) from the given physics of the forward model and the information contained in the measurements, which possibly contains many combinations of viable solutions.

Now that the inversion problem has been expressed in terms of an integral equation due to the complexity of the physics, it must again be transformed into a system of linear equations in order for the techniques of linear algebra to be employed for obtaining solutions. This is done via quadrature, i.e., the reduction of integral equations to that of a set of linear ones, most commonly by subdividing the domain of $f(x)$ into N-1 regions, and allowing $f(x)$ to take the values f_1 at x_1, ... , f_N at x_N where $f(x)$ varies linearly across each region. As demonstrated in Chapter 2 of Twomey Twomey (1977), by summing the contributions from each subinterval the quadrature formula is obtained which allows the following expression to be written;

$$S(y) = \int K(y_i, x)\ f(x)\ dx \cong \sum_j a_{ij}\ f(x_j)\ \Rightarrow \mathbf{S} = \mathbf{Af}, \tag{42}$$

where $\mathbf{A}$ contains the a_{ij} quadrature coefficients for the i^{th} kernel. To be consistent with the notation used by Rodgers Rodgers (2000), the right most expression in Eqn. 42 will now be re-expressed with no change in its meaning as follows;

$$\mathbf{S} = \mathbf{Af} \Rightarrow \mathbf{y} = \mathbf{Kx}, \tag{43}$$

where $\mathbf{y}$ is the matrix of measurement vectors, $\mathbf{x}$ is the matrix of unknown state parameters and $\mathbf{K}$ is the matrix of contribution functions, i.e., the kernel.

Now that the problem is once again expressed in terms of a system of equations the condition of the problem can be classified in terms of being ill- or well-posed. Ill-posed problems can be subdivided into under- or over-determined systems (synonymous with

Table 2: **Constraint classifications of retrieval systems expressed in terms of the number of measurements m, number of unknown state parameters n and the rank p.**

	Condition	Class	Description
1.	$p = m = n$	Well-posed	Same # of meas. as unkn. All meas. indep.
2.	$p < m = n$	Under. + Over.	Same # of meas. as unkn. Meas. not indep.
3.	$p = m < n$	Under.	More unkn. than meas. All meas. indep.
4.	$p < m < n$	Under. + Over.	More unkn. than meas. Meas. not indep.
5.	$p = n < m$	Over.	More meas. than unkn. Unkn. all in row space
6.	$p < n < m$	Under. + Over.	More meas. than unkn. Unkn. not in row space

under- and over-constrained). These terms are used to describe the state of the system with regard to the mathematical ability to determine a solution. The classifications are defined by eigenvalue analysis of the kernel $\mathbf{K}$ to determine the row space, with rank = p and null space of the system and are intimately related to the various degrees of freedom of the retrieval to be discussed later in Section ii. Six distinct classifications are identified by Rodgers Rodgers (2000), and are listed in Table 2, with rank, p, identifying the number of fully independent equations in the linear system. In summary, if $p < n$ then a null space exists and the system is under constrained. If $p < m$ then the system is over constrained in some part of the row space. Note that in the current retrieval problem in this study, $n = 16$, $m = 14 \Rightarrow m < n$, confining the classification of the problem to cases 3 and 4.

Another serious complication when dealing with the inverse problem is that of the propagation of small errors within the system. As demonstrated lucidly in Chapter 1 of Stephens' text Stephens (1994) even minute changes in the measurements due to uncer-

tainties can lead to solutions which are dramatically different Stephens (1994). When spurious information, no matter how slight, is admitted into the system of equations, numerical instabilities may form in the calculations due to small values of the determinants. This easily leads to the solutions of the problem being driven by the errors rather than the real part of the information contained in the measurements Twomey (1977).

3b. *Bayes Theorem*

A better framework for dealing with large and complex systems is to pose the inversion problem in terms of probability distributions. In this new basis the various spaces (measurement, solution, error, etc.) are described mathematically using probability distribution functions (PDFs) rather than discrete values. Specifically Bayes Theorem assigns PDFs to the measurement space, $P(y)$, and state space, $P(x)$, as well as to the combined measurement and state space, $P(x, y)$. PDFs are also assigned to the two conditional spaces of measurement for a known state, $P(y|x)$ and state for a known measurement, $P(x|y)$. Note that $P(y, x)$ has the same meaning as $P(x, y)$.

A schematic diagram is shown in Figure 8 to illustrate the relationship between these PDFs in the one dimensional case. Based on this figure, an expression for Bayes Theorem is easily derived by first recognizing that the conditional probability $P(y|x)$ is given by the ratio of the combined space to the combined space integrated over the measurement domain, i.e.,

$$P(y|x) = \frac{P(x, y)}{\int P(x, y)dy}. \tag{44}$$

Similarly,

$$P(x|y) = \frac{P(x, y)}{\int P(x, y)dx}. \tag{45}$$

Using the definitions of $P(x)$ and $P(y)$ given by,

$$P(x) = \int_{-\infty}^{+\infty} P(x,y)dy \tag{46}$$

and

$$P(y) = \int_{-\infty}^{+\infty} P(x,y)dx \tag{47}$$

respectively, Eqns. 44 and 45 can be rewritten as,

$$P(y|x) = \frac{P(x,y)}{P(x)}, \tag{48}$$

and

$$P(x|y) = \frac{P(x,y)}{P(y)}. \tag{49}$$

Solving Eqn. 48 for $P(x,y)$ and substituting into Eqn. 49, yields the formal definition of Bayes theorem, stated as,

$$P(x|y) = \frac{P(y|x)P(x)}{P(y)}. \tag{50}$$

Eqn. 50 can be described in the following way; the determination of a PDF describing the state space from a known measurement space, i.e. the solution to the retrieval, $P(x|y)$, can be obtained if we know the relationship between the measurements given some state, i.e., the forward model, $P(y|x)$, and also have some *a priori* distribution of the state space, $P(x)$, and measurement space, $P(y)$.

Now we formally introduce the measurements into a vector $\mathbf{y}$ with covariance $\mathbf{S_y}$ and the unknown state parameters into a vector $\mathbf{x}$ with *a priori* values $\mathbf{x_a}$ and covariance $\mathbf{S_a}$. The *a priori* set of values represents our previous knowledge of the atmospheric state of the parameters of interest and may be thought of as a set of virtual measurements as

Figure 8: Bayesian PDFs. From Rodgers (2000).

discussed by Rodgers Deepak (1977). In atmospheric sciences the *a priori* typically consists of the statistics of other measurements, i.e., the climatology or mean and covariance of an ensemble of states of the parameters of interest, but may also be composed from other sources such as arbitrary restrictions or restraints due to the physics of the problem Rodgers (2000). Let $\mathbf{K}$ represent the contribution functions from the linear forward model as defined in Eqn. 43. A solution for the expected value of the PDF $P(x|y)$, which is represented by,

$$\hat{\mathbf{x}} = \int \mathbf{x} P(x|y) d\mathbf{x} \tag{51}$$

can be written in the Bayesian framework by expressing $P(y|x)$ in terms of error weighted variances between the measured and modeled irradiances as,

$$-2 \ln P(y|x) = (\mathbf{y} - \mathbf{K}\mathbf{x})^T \mathbf{S}_\mathbf{y}^{-1} (\mathbf{y} - \mathbf{K}\mathbf{x}) + c_1. \tag{52}$$

Similarly $P(x)$ can be expressed in terms of the error weighted variances in the estimated and *a priori* state parameters as,

$$-2\ln P(x) = (\mathbf{x}-\mathbf{x_a})^T\mathbf{S_a^{-1}}(\mathbf{x}-\mathbf{x_a}) + c_2, \tag{53}$$

where c_1 and c_2 are constants. Substituting these last two expressions into the Bayesian statement (Eqn. 50) yields for the posterior PDF,

$$-2\ln P(x|y) = (\mathbf{y}-\mathbf{Kx})^T\mathbf{S_y^{-1}}(\mathbf{y}-\mathbf{Kx}) + (\mathbf{x}-\mathbf{x_a})^T\mathbf{S_a^{-1}}(\mathbf{x}-\mathbf{x_a}) + c_3. \tag{54}$$

Discussion of this equation with regard to achieving actual solutions will be postponed to Section 3c.

Conceptually we can imagine the retrieval problem in the Bayesian framework as depicted in Figure 9 for a three-dimensional problem, i.e. for three unknowns. This figure can be visualized piecemeal by first selecting the two perpendicular planes in state space corresponding to the *a priori* values of the unknown parameters, $\mathbf{x_a}$. The solution to the problem is then predicted to exist within some relatively large state space which is defined by the volume of the *a priori* covariance, $\mathbf{S_a}$, which surrounds the origin of $\mathbf{x_a}$. In general this will be an elliptical volume but could be a perfect sphere if all three parameters spanned the same range. Next we introduce the measurements and forward model into the problem which narrow the region in *a priori* space to which the solution is to be found and which is represented as an infinitesimal line through the state space. This line will be referred to as the "information line", as it represents the information added to the problem via the measurements and forward model. In Figure 9 the information line is drawn perpendicular to the x-y plane to represent two measurements, but it would cut through at some other angle if three or more measurements were used. The information line is blurred by way of the uncertainties of both the measurements and forward model

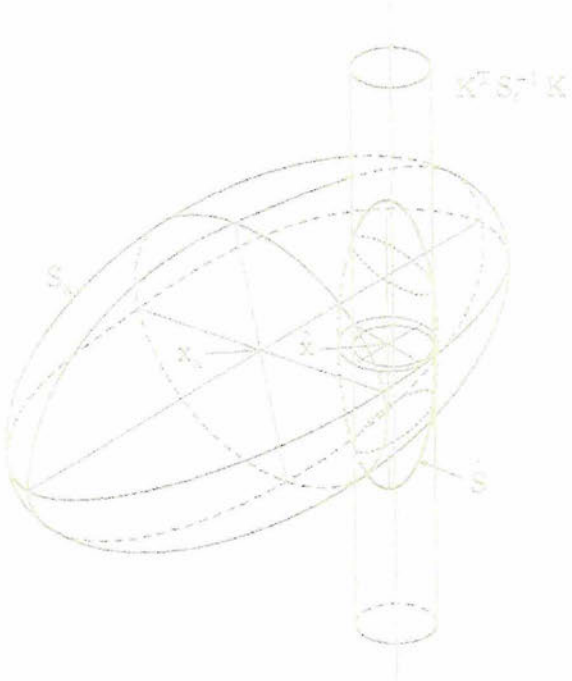

Figure 9: Interpretation of the Bayesian problem in terms of PDFs for the *a priori*, measurement, solution and error spaces. From Rodgers (2000).

(i.e., $\mathbf{K}^{\mathrm{T}}\mathbf{S}_{\mathrm{y}}^{-1}\mathbf{K}$), which is represented as a cylinder surrounding the measurement. The plane determined by the intersection of the information cylinder and the *a priori* plane leaves us with some estimated PDF of the parameters, $\hat{\mathbf{x}}$, in the *a priori* state plane. Note that the origin of $\hat{\mathbf{x}}$ does not necessarily coincide with the intersection of the measurement in the *a priori* plane. The difference in the two is a measure of the influence of the *a priori* values in determining the solution. Finally, the estimated uncertainty in the retrieval, $\hat{\mathbf{S}}$, is then represented by the ellipse formed around the estimated values in *a priori* space, $\hat{\mathbf{x}}$. More discussion of $\hat{\mathbf{S}}$ is to follow in Section 3c

3c. *Linear Optimal Estimation*

i. Selecting a Solution Out of State Space To be of much use however a more exact technique must be implemented within the Bayesian framework to select a specific answer at each grid point or time point within the domain. In our particular case we need an algorithm to select values of the desired atmospheric variables for each set of instrument irradiance measurements contained in the full data set.

The Maximum *a Posteriori* Solution A particular selection from the PDF of state space can be made by optimizing some component of the system, which normally entails minimizing or maximizing some quantity. The maximum *a posteriori* technique, used in this research, represents the solution as the most likely state (the state which maximizes $P(x|y)$) or the expected state (the mean state averaged over the PDF) along with the uncertainty of the solution in the form of the width of the PDF. For a Gaussian distribution the most likely (maximum) and expected (mean) state are equivalent due to the symmetry of the PDF. The form of the PDF to be maximized has already been obtained (Eqn. 54), which can be rewritten in the general sense, with $\mathbf{F}(\hat{\mathbf{x}})$ replacing $\mathbf{Kx}$, as,

$$\Phi = [(\mathbf{y} - \mathbf{F}(\mathbf{x}))^T \mathbf{S_y}^{-1} (\mathbf{y} - \mathbf{F}(\mathbf{x}))] + [(\mathbf{x} - \mathbf{x_a})^T \mathbf{S_a}^{-1} (\mathbf{x} - \mathbf{x_a})]. \tag{55}$$

Gauss-Newton Method The mathematical expression which is to be minimized (or maximized) is termed the cost function (Eqn. 55), and provides the most likely estimated state of the parameters from the Gaussian PDF, $P(x|y)$. Nominally an inflection point of the cost function is found by equating the derivative to zero. Letting $\nabla_{\mathbf{x}}\mathbf{F}(\mathbf{x}) = \mathbf{K}$, the derivative of the cost function is,

$$\mathbf{g}(\mathbf{x}) = -\mathbf{K}^{\mathbf{T}}(\mathbf{x})\mathbf{S}_{\mathbf{y}}^{-\mathbf{1}}[\mathbf{y} - \mathbf{F}(\mathbf{x})] + \mathbf{S}_{\mathbf{a}}^{-\mathbf{1}}(\mathbf{x} - \mathbf{x}_{\mathbf{a}}) = 0. \tag{56}$$

Now we introduce Newton's method which iteratively generates a sequence of approximations which converge to the solution of $f(x) = 0$. The general form of Newton's method is written as;

$$\mathbf{x_{i+1}} = \mathbf{x_i} - [\nabla_{\mathbf{x}}\mathbf{g}(\mathbf{x_i})]^{-1}\mathbf{g}(\mathbf{x_i}), \tag{57}$$

where $\mathbf{g}(\mathbf{x})$ is the first derivative given in Eqn. 56 and $\nabla_{\mathbf{x}}\mathbf{g}$ is the second derivative, or Hessian, given as,

$$\nabla_{\mathbf{x}}\mathbf{g} = \mathbf{S_a^{-1}} + \mathbf{K^T S_y^{-1} K} - [\nabla_{\mathbf{x}}\mathbf{K^T}]\mathbf{S_y^{-1}}[\mathbf{y} - \mathbf{F}(\mathbf{x})] \tag{58}$$

Substituting Eqns. 56 and 58 into Eqn. 57 and ignoring the terms in the Hessian involving the second derivative of the Forward model, $\nabla_{\mathbf{x}}\mathbf{K}$, produces the iterative equation,

$$\mathbf{x_{i+1}} = \mathbf{x_i} + (\mathbf{K_i^T S_y^{-1} K_i} + \mathbf{S_a^{-1}})^{-1}[\mathbf{K_i^T S_y^{-1}}(\mathbf{y} - \mathbf{F}(\mathbf{x_i})) - \mathbf{S_a^{-1}}(\mathbf{x_i} - \mathbf{x_a})] \tag{59}$$

where $\mathbf{i}$ represents the iteration number and $\mathbf{K}$ represents the Jacobian matrix calculated at the previous estimated state with terms given by

$$\mathbf{K}_{i,j} = \frac{\partial \mathbf{F}_i(\mathbf{x})}{\partial \mathbf{x}_j}, \tag{60}$$

where i and j refer here to the rows and columns of $\mathbf{K}$, respectively.

The estimated retrieval error covariance is introduced in Eqn. 59 as,

$$\hat{\mathbf{S}} = (\mathbf{K^T S_y^{-1} K} + \mathbf{S_a^{-1}})^{-1}, \tag{61}$$

which is substituted into a computational form of the iteration equation, allowing it to be

re-expressed as,

$$\hat{\mathbf{x}} = \hat{\mathbf{x}}_{\mathbf{i-1}} + \hat{\mathbf{S}}[\mathbf{K}^{\mathbf{T}}\mathbf{S}_{\mathbf{y}}^{-1}(\mathbf{y} - \mathbf{F}(\hat{\mathbf{x}}_{\mathbf{i-1}})) + \mathbf{S}_{\mathbf{a}}^{-1}(\mathbf{x}_{\mathbf{a}} - \hat{\mathbf{x}}_{\mathbf{i-1}}))] \tag{62}$$

The $\hat{\mathbf{S}}$ matrix is referred to as the retrieval covariance matrix which gives associated errors in the retrieved values due to the selection of one solution vector out of the total possible solution space described by the Bayesian statistics. It is equivalent to the Fisher information matrix. Fisher information theory tells us that for the Gaussian linear case the inverse covariance of the solution is the sum of the information matrices for the independent sources.

Iterations of Eqn. 62 proceed until the convergence criteria given by,

$$(\hat{\mathbf{x}} - \hat{\mathbf{x}}_{\mathbf{i-1}})^T \hat{\mathbf{S}}^{-1}(\hat{\mathbf{x}} - \hat{\mathbf{x}}_{\mathbf{i-1}}) \ll n \tag{63}$$

where n is the number of retrieval parameters, is fulfilled. Ignoring the $\nabla_{\mathbf{x}}\mathbb{K}$ term is allowed in linear and nearly-linear problems as it approaches zero for subsequent iterations. This approximate numerical method for finding the zero of the gradient of the cost function is called Gauss-Newtonian iteration. It is common, but not necessary, to start the first iteration with $\mathbf{x_0} = \mathbf{x_a}$. In this study the first iteration of the first set of measurements (the term 'scan' will be used to represent any particular set of measurements) for each day is initialized with $\mathbf{x_0} = \mathbf{x_a}$. However, if the retrieval successfully converges on some scan, the following scan is initialized with $\mathbf{x_0} = \hat{\mathbf{x}}$. A minimum of two iterations are performed for each scan and if convergence is not successful by iteration six the iteration process is terminated and the scan is considered to have failed convergence. The subsequent scan would then be initialized with $\mathbf{x_0} = \mathbf{x_a}$. Six iterations was chosen as the maximum number allowed based on testing which indicated that scans which did not converge by about five iterations were unable to converge even by iteration ten or greater.

ii. Interpreting the Results from Optimal Estimation Retrievals The power of the optimal estimation technique is that these associated errors, as well as other diagnostics which characterize the usefulness of the retrieval, are mathematically linked to the estimated state vector. Once the retrieval has converged on a solution for each particular grid or time point, several valuable diagnostic components can be calculated from various combinations of the retrieval inputs; $\mathbf{y}$, $\mathbf{S_y}$, $\mathbf{x_a}$, $\mathbf{S_a}$, the iterative terms in the retrieval; $\mathbf{F(x)}$, $\mathbf{K}$ and the retrieval outputs; $\hat{\mathbf{x}}$, $\hat{\mathbf{S}}$. The full set of diagnostics are the chi-squared statistical significance (χ^2), the correlation matrix, the Gain matrix, the Averaging kernel or *a priori*-matrix, the Shannon information content (H) and the degrees of freedom (dof) for *a priori*, signal and measurement.

Covariance error When the convergence criteria given by Eqn. 63 is satisfied, the left hand term ($\hat{\mathbf{x}}$) of Eqn. 62 contains the newly estimated values of the n state parameters. Implicit in the optimal estimation technique is the idea of associated errors in the input measurements, the *a priori* state parameters and the retrieved values due to the selection of one solution vector out of the total possible solution space described by the Bayesian statistics. Mathematically the associated errors are contained in the nxn $\hat{\mathbf{S}}$ matrix, known as the error covariance matrix. Eqn. 61 shows that the error covariance matrix is calculated as a combination of the *a priori* error and measurement error covariances weighted with the Jacobian of the forward model.

Letting k represent the element of the corresponding vector or matrix, the diagonal values of $\hat{\mathbf{S}}$ are transformed into percent error in the retrieved values via,

$$\xi_k = \sqrt{\frac{\hat{\mathbf{S}}_{(k,k)} * 100}{\hat{\mathbf{x}}_k}}, \tag{64}$$

thereby allowing error bars to be placed on the estimated state parameters.

The correlation in the retrieval errors is also calculated from $\hat{\mathbf{S}}$ as,

$$\mathbf{C}_{(i,j)} = \frac{\hat{\mathbf{S}}_{(i,j)}}{\sqrt{[\hat{\mathbf{S}}_{(i,i)} * \hat{\mathbf{S}}_{(j,j)}]}}, \tag{65}$$

where i and j represent the rows and columns of the matrix.

Chi-squared Under the assumption that the population distribution is normal, the population variability is assumed to follow that of the χ^2 distribution allowing the Pearson χ^2 test for goodness of fit to be applied Johnson and Bhattacharyya (1996), which tells us if a particular random vector belongs to a given Gaussian distribution. The chi-squared value is determined by,

$$\chi^2 = [(\mathbf{F}(\mathbf{x}) - \mathbf{y})^T)\mathbf{S_y}^{-1}(\mathbf{F}(\mathbf{x}) - \mathbf{y})] + [(\hat{\mathbf{x}} - \mathbf{x_a})^T\mathbf{S_a}^{-1}(\hat{\mathbf{x}} - \mathbf{x_a})], \tag{66}$$

which is a linear combination of the error weighted difference in the modeled and measured irradiances and the error weighted difference between the estimated state parameter and the *a priori* value. Note that the form of χ^2 equation is identical to that of the scalar cost function to be minimized (Eqn.55). If the assumption of Gaussian error statistics is valid then χ^2 should be approximately equal to the number of independent parameters in the retrieval (a number which can be obtained from the degrees of freedom of the retrieval as discussed below). More precisely a table of percentage points can be consulted in order to determine the statistical probability that a value of χ^2 was obtained by chance. According to the table of percentage points using 15 degrees of freedom, a value of χ^2 is considered significant (falls in the rejection region) at the 95% level if the χ^2 values fall between 27.5 and 6.3, while the values are considered significant at the 80% level if the χ^2 values fall between 22.3 and 8.6. Underestimating the input error budget tends toward large χ^2, while small χ^2 is indicative of overestimating the error budget L'Ecuyer

and Stephens (2002).

Gain matrix The Gain matrix is calculated as,

$$\mathbf{G} = \hat{\mathbf{S}}\mathbf{K}^{\mathrm{T}}\mathbf{S}_{\mathrm{y}}, \tag{67}$$

the columns of which are the contribution functions. As can be interpreted from the equation, the contribution functions are an error weighted form of the retrieval covariances and indicate the contribution to the retrieval solution from the measurement and model errors. The larger the contribution functions, the greater the contribution from measurement and model error in retrieving the solution and therefore the less well defined the solution space.

A-matrix Another useful diagnostic tool implicit within the OE algorithm is determining the relative contribution of the measurements versus the *a priori* to the estimated state value for each particular parameter. The fractional use of the measurements in estimating each parameter from each retrieval is contained in the diagonal elements of a matrix referred to as the Averaging kernel or Apriori-matrix (A-matrix for short). As shown in Rodgers' text Rodgers (2000) the A-matrix is calculated as a product of the Gain matrix (G) and the Jacobian $\mathbf{K}$ as follows,

$$\mathbf{A} = \mathbf{G}\mathbf{K} = \hat{\mathbf{S}}\mathbf{K}^{\mathrm{T}}\mathbf{S}_{\mathrm{y}}^{-1}\mathbf{K}. \tag{68}$$

The A-matrix values can be thought of as simply error weighted forward model sensitivities. A value for which the model has high sensitivity will have high A-matrix values, assuming constant error.

A more lucid interpretation of the A-matrix can be gleaned from the 1-D case as discussed in Engelen and Stephens Engelen and Stephens (1997) where A is a scalar

which weights the estimated state determined from the measurements and the *a priori*,

$$\hat{x} = Ax + (1 - A)x_a + D_y\epsilon_y, \tag{69}$$

where D_y is the derivative of the inverse model with respect to y and ϵ_y is the error in the measurements. This expression clearly shows how the estimated state is calculated as a linear combination of the measurement and *a priori* values. An A-value of 1 indicates complete reliance on the measurements when determining the newly estimated state parameter and hence high usefulness of the retrieval. Conversely an A-value of zero indicates that the measurements provided no useful information in determining the estimated state parameter which is therefore set equal to the *a priori* value.

Analyzing the A-values for each retrieval parameter allows quantification of when the measurements are providing useful information in determining the estimated values, but also gives the relative strength of information contained in each retrieved parameter type. For example one parameter type in a multi-parameter retrieval may continuously return A-values very close to zero, indicating that this parameter cannot successfully be retrieved from the provided measurements. It is possible to establish some minimum threshold for determining a "good" retrieval by use of the A-values as will be discussed later.

Degrees of freedom Since solving the optimal estimation problem is synonymous with solving a system of algebraic equations in the framework of linear algebra, that branch of mathematics can be used to characterize the condition of the system through the use of eigenvector/eigenvalue analysis. This is done by first determining the error weighted Jacobian matrix as,

$$\tilde{\mathbf{K}} = \mathbf{S_y}^{-1/2}\mathbf{K}\mathbf{S_a}^{1/2} \tag{70}$$

In practice $\mathbf{S_y}^{-1/2}$ and $\mathbf{S_a}^{1/2}$ are computed through pre-whitening via Cholesky decomposition to make the problem tractable. The matrix $\tilde{\mathbf{K}}$ is then solved via singular value decomposition to obtain the i eigenvalues, $\tilde{\lambda}_i$. These eigenvalues contain information pertaining to the various degrees of freedom (dof) of the system.

The number of dof for signal, dof_s, is given by Rodgers as,

$$dof_s = \sum_n \frac{\tilde{\lambda}_i^2}{(1.0 + \tilde{\lambda}_i^2)}, \tag{71}$$

indicating the number of useful independent observations in the retrieval
Rodgers (2000). This value can be regarded as the effective rank of the problem in measurement space.

The degrees of freedom in the *a priori*, dof_a, given by the trace of the normalized $\mathbf{S_a}$ matrix, indicates the number of free parameters which actually need to be retrieved during inversion, i.e., the number of independent parameters [T. L'Ecuyer, personal communication]. For example, if $\mathbf{S_a}$ is a diagonal matrix (off-diagonals set equal to zero), indicating no *a priori* knowledge of the covariances between parameters, then $dof_a = n$, meaning that there are n parameters which need to be determined from the retrieval. However, if some correlations between parameters are introduced via off-diagonal values in $\mathbf{S_a}$, such as occurs for vertical temperature profiles at adjacent levels or AODs at adjacent wavelengths, then dof_a will have some new value, $n - q$, indicating that there are less than n parameters which need to be determined from the retrieval. This is consistent with the idea of adding information to the retrieval *a priori*, which in turn means that more information, i.e., parameters, can be extracted from the same number of input measurements.

A measure of the level of constraint of the retrieval (under, over or fully constrained) is provided by the ratio of the independent measurements available to the independent

number of variables being sought:

$$dof_R = \frac{dof_s}{dof_a}. \tag{72}$$

Monitoring the change in this ratio due to changes in the retrieval parameterizations allows for the quantification of the usefulness of adding information into the retrieval [T. L'Ecuyer, personal communication]. Ideally a retrieval scenario will have $dof_R = 1$, indicating that the retrieval is fully constrained, but realistically retrievals are by nature somewhat ill-posed problems. The reader is referred back to Table 2.

Finally the dof for measurement, dof_m is given as the number of eigenvalues greater than one, i.e., $\tilde{\lambda} > 1$, which quantifies the number of useful independent quantities which can be retrieved from the measurements. This value can be regarded as the effective rank of the problem in state space. The ratio of dof_m to the dimensions of the retrieval vector $\mathbf{x}$ gives a crude indication of the fraction of the estimated state parameters determined completely from the measurements. This quantification is crude in the sense that it contains no information as to which parameters were successfully retrieved and which were not. It is important to note that dof_m is an integer and therefore has reduced resolution relative to the dof_s and dof_a. The value of dof_s will always be larger than that of dof_m, and the residual of the two gives the degrees of freedom for noise, dof_ϵ. That is, dof_s is composed of two components, dof_m with the addition of dof_ϵ.

Information content Information theory quantifies the amount of information contained in some system and can be expressed using several different definitions. One way is the Shannon information content (H), which utilizes the concept of the entropy of a system, and is developed in direct analog to that of the Gibb's thermodynamic entropy given by,

$$S(P) = -k \sum_i p_i \ln p_i, \tag{73}$$

where p_i is the probability of the system being in state i. In information theory $k = 1$ rather than Boltzmann's constant and $\log_2$ is used so that the information content is expressed in terms of the number of bits required to uniquely identify the state. Using this definition of entropy allows quantification of the information contained in a retrieval in terms of distinguishing the size of the posterior solution space from the *a priori* solution space. The IC is then expressed as the difference in entropy between the *a priori* state space and the retrieved state space as,

$$H = S(P_a) - S(P_x), \tag{74}$$

where S represents entropy, P_a is the *a priori* PDF and P_x is the posterior PDF. Since the difference in the entropy of these two states is due to the addition of information through the retrieval process, it follows that the IC is a quantification of the reduction of disorder due to forward model and the measurements.

It is a useful exercise to show the similarity of information content to that of the signal-to-noise ratio in the simple scalar Gaussian case in order to fully appreciate and interpret the parameter. Also, in order to calculate actual values of H it is desirable to derive a calculation for the entropy of the *a priori* and posterior states, which can be done in terms of signal-to-noise, i.e., the eigenvalues related to $\mathbf{K}$. Defining the entropy of a continuous PDF as,

$$S(P) = -\int P(x) \log_2[P(x)/M(x)]dx, \tag{75}$$

a measure of entropy for the scalar case is found by simple substitution of the definition of the PDF of a Gaussian distribution, followed by integration to be,

$$S = \ln \sigma(2\pi e)^{1/2}. \tag{76}$$

With initial state P_a and final state P_x, the difference in entropy, or information content of the retrieval becomes,

$$H = S(P_a) - S(P_x) = \ln \sigma_1 (2\pi e)^{1/2} - \ln \sigma_2 (2\pi e)^{1/2} = \ln \frac{\sigma_1 (2\pi e)^{1/2}}{\sigma_2 (2\pi e)^{1/2}} = \ln \frac{\sigma_1}{\sigma_2}, \quad (77)$$

where σ_1^2 is the variance of the *a priori* Gaussian distribution and σ_2^2 is the variance of the posterior Gaussian distribution. This indicates that the retrieval information content in the scalar Gaussian case is represented by the logarithm of the signal-to-noise ratio.

The more complicated multi-variate case can be interpreted similarly and will be used to derive a form of H in terms of the eigenvalues introduced in the previous section. Letting the m eigenvalues of $\mathbf{S_y}$ represent the variances of the individual variables in the vector with m elements, then the previously determined expression for the scalar entropy (Eqn. 76), with σ replaced by $\tilde{\lambda}$, can be rewritten as,

$$S[P(y)] = \sum_{i=1}^{m} \ln (2\pi e \tilde{\lambda}_i)^{\frac{1}{2}} \quad (78)$$

where $S[P(y)]$ now represents the total entropy of the combined m variables. By assuming that the total entropy of independent combined PDFs is equivalent to the sum of the entropy of the individual PDFs, that is,

$$S[\prod_{i=1}^{m} P(i)] = \sum_{i=1}^{m} S[P(i)], \quad (79)$$

Eqn. 78 can again be re-expressed as,

$$S[P(y)] = m \ln (2\pi e)^{\frac{1}{2}} + \frac{1}{2} \ln \prod_i \tilde{\lambda}_i, \quad (80)$$

by replacing the individual entropy sums with the combined product.

Since the determinant of a matrix is equal to the product of the eigenvalues, the final

expression for the entropy of the multi-variate state becomes,

$$S[P(y)] = m \ln (2\pi e)^{\frac{1}{2}} + \frac{1}{2} \ln |\mathbf{S_y}|, \tag{81}$$

Using $\mathbf{S_a}$ and $\hat{\mathbf{S}}$ as the covariance of the prior and posterior state spaces, respectively, the information content of a retrieval is given by

$$H = S(P_a) - S(P_x) = [m \ln (2\pi e)^{\frac{1}{2}} + \frac{1}{2} \ln |\mathbf{S_a}|] - [m \ln (2\pi e)^{\frac{1}{2}} + \frac{1}{2} \ln |\hat{\mathbf{S}}|] = \frac{1}{2} \ln |\mathbf{S_a}\hat{\mathbf{S}}^{-1}|. \tag{82}$$

Using Eqn. 80 and the knowledge that each eigenvalue is proportional to the square of the principal axis of the ellipsoid represented by the surface of the constant PDF, Eqn. 81 allows the entropy to be physically interpreted as the volume of state space occupied by the PDF. This in turn allows the information content (Eqn. 82) to be interpreted as the amount of change in the occupied volume in state space due to the retrieval. Referring back to Figure 9, the IC of any particular retrieval can be interpreted as the difference in the volume of the *a priori* ellipsoid ($\mathbf{S_a}$) relative to the smaller retrieval covariance ellipsoid ($\hat{\mathbf{S}}$).

The measurement of information content can take place in either measurement space or in state space, in both cases yielding the same result. In practice the equation for H is rewritten in terms of the eigenvalues of the $\tilde{\mathbf{K}}$ matrix and calculation of the value is traditionally performed in terms of binary bits as,

$$H = \frac{1}{log_2} \frac{1}{2} \sum_i ln(1 + \tilde{\lambda}_i^2), \tag{83}$$

where 2^H is the magnitude of the reduction in the uncertainty of the retrieved state due to addition of the measurements L'Ecuyer et al. (2005).

iii. The Optimal Estimation Framework Applied to the Aerosol Problem in the Ultra-Violet As mentioned previously the optimal estimation framework has been built up specifically for determining aerosol optical properties (AOD, SSA, TOC) from the irradiance measurements of the UV-MFRSR instruments which are providing continuous measurements of direct and diffuse solar irradiances at approximately 30 sites in the U.S.A. via the UVMRP Goering et al. (2005). In order to build a useful retrieval it is important to include as many of the parameters as possible explicitly into the algorithm to which the retrieval is sensitive. It is equally important however not to force a nearly-well-posed problem into a highly ill-posed one by heedlessly adding parameters to the state vector without adding additional information into the retrieval. Ways of adding information into the retrieval include addition of off-diagonal elements into the model-measurement and/or *a priori* covariance matrices, addition of independent or semi-independent measurements or addition of physics into the forward model. Any parameters which are not included explicitly in the retrieval but to which there is some sensitivity ($\mathbf{b}$ in Eqns. 37 and 39) must be represented in the retrieval error budget by incorporating estimated uncertainties into the model-measurement covariance matrix.

As was shown in the previous work by Goering *et al.* the 7 channels direct and diffuse irradiance measurements provide sufficient information for the retrieval of the aerosol optical depth and aerosol single scatter albedo at the 7 wavelengths plus the total ozone column Goering et al. (2005). Due to the physics of the problem the direct beam provides the most useful information for determining the aerosol optical depth since this component contains unscattered radiation. Similarly the aerosol single scattering albedo is provided mostly from the measurement of the diffuse component as it contains information related to the scattering of the radiation as it interacts with the aerosols. As discussed previously, ozone contains strong absorption lines in the UV-B region and therefore building this parameter into the retrieval vector, rather than relying

on a fixed value of TOC, was found to increase the usefulness of the retrieval. The short wavelength channels contribute most significantly to determining the estimated value of TOC. Furthermore it was found that the asymmetry factor g could also be retrieved from the algorithm using the same 14 input measurements by adding some information into the physics of the problem in the way of covariances between the parameters in the $\mathbf{S_a}$ matrix.

With the explicit retrieval of AOD, SSA, TOC and g, the remaining parameters to which the algorithm is most sensitive under clear sky conditions, and which are therefore characterized in the input error budget are; 1.) approximations in the method used to obtain a solution to the radiative transfer equation in the forward model, 2.) the local surface albedo, α_s, 3.) the error in the Langley method used to calibrate the instrument's radiometric sensitivity and 4.) other instrument measurement and calibration errors. Other parameters which are contained in the model but for which little or no testing was undertaken include; vertical distributions of water vapor or relative humidity, vertical distributions of the ozone and aerosol layer, vertical distributions and column amounts of other trace gases such as NO_2 and SO_2. A detailed account of the sensitivity testing follows in Section 4b. Explicit discussion of the inputs to the OE algorithm for the initialization site can be found in Section 6a.

4. The Measurements and Forward Model

4a. *Instrumentation and Measurements*

The measurements, y, used in the retrieval (Eqn. 62), are the direct and diffuse irradiances measured by an Ultraviolet Multi-Filter Rotating Shadow Band Radiometer (UV-MFRSR), which is operated by the National Resource Ecology Laboratory's (NREL) UV Monitoring and Research Program (UVMRP) at Colorado State University (CSU). A detailed description of the original visible wavelength version of the instrument is provided by Harrison *et al.* Harrison et al. (1994). A UV wavelength version of the instrument has since been developed and implemented operationally Bigelow and Slusser (2000). The center wavelengths of the 7 ion-assisted-deposition filters are 300-, 305-, 311-, 317-, 325-, 332- and 368-nm with an approximate Full Width at Half Max (FWHM) of 2-nm.

Since its inception in the mid-1990s usage of this relatively simple and inexpensive instrument has expanded to include hundreds of units located at sites worldwide [M. Beaubien, personal communication]. The UVMRP alone operates approximately 80 MFRSR instruments (half UV and half visible versions) at field sites spaced in a roughly 5° by 10° latitude/longitude resolution grid which divides the continental United States into 26 regions with site emphasis on agricultural and forested areas Bigelow et al. (1998). More detailed information concerning the operational sites is available at the UVMRP web site http://uvb.nrel.colostate.edu/UVB/home_page.html.

The instruments in the UVMRP network are carefully calibrated and characterized for stray light leakage, filter response and detector angular correction by personnel from the UVMRP and the National Oceanic and Atmospheric Administration's (NOAA) Central UV Calibration Facility (CUCF) Lantz et al. (1999) before being deployed into the field. Several additional uncertainties in the instrument measurements exist, including quantization error of the analog voltage signal, nighttime bias voltage, temperature drift

and shadowband alignment Krotkov et al. (2005). Although the total measurement error budget as discussed in Krotkov *et al.* (ref. Table 1 therein) shows slight dependence on SZA and AOD, in this study it is taken to be independent of wavelength, SZA, AOD and SSA for simplicity. The mean value of instrument uncertainty from that table (0.023) is used to represent the instrument measurement error for all conditions.

To calibrate the radiometric response of the instrument either Langley or standard lamp calibrations are used, both of which are described in Slusser et al. (2000). Lamp calibrations are performed in the laboratory by the CUCF following the procedures outlined in Early et al. (1988a) and Early et al. (1988b). A total lamp calibration uncertainty of +/- 2.5% was determined to exist for all 7 channels. Langley calibrations are performed by extrapolating the instrument's measured voltage signal versus air mass to the top of the atmosphere (TOA) (air mass = 0) to obtain voltage intercepts ($V_{0,\lambda}$), which are then divided into the mean TOA insolation to obtain a measure of $(W/(m^2nm)/V)$. Statistical analysis are performed to reject outliers and reduce uncertainties following the algorithm of Harrison and Michalsky Harrison and Michalsky (1994). Results indicate that the Langley calibrations have an accuracy of $\pm 3.8\%$ at 300-nm and $\pm 2.1\%$ at 368-nm, with repeatability of $\pm 3.3\%$ and $\pm 0.7\%$, at 300- and 368-nm respectively Slusser et al. (2000). The stability and quality of the instruments have been thoroughly explored by the UVMRP Bigelow and Slusser (2000) and determined to have drifts in sensitivity of -1.2% at 300-nm, -4.8% at 305-nm, -2.6% at 311-nm, -3.0% at 317-nm, -4.8% at 325-nm, -4.9% at 332-nm and -3.7% at 368-nm in the filter response Janson and Slusser (2003).

A detailed account of the corrections made by the UVMRP to the measured raw voltages is given in Krotkov *et al.* Krotkov et al. (2005). The instruments make a diffuse (shadow-band blocking the sun) and total (no shadow-band) measurement every 20 seconds and the direct beam component is obtained via subtraction of these two mea-

surements, followed by correction for SZA. Then the instrument dark count (night time bias) is subtracted from the diffuse voltage data, which are then normalized by the cosine of the zenith angle to produce the horizontal component of the beam. Corrections are made to the direct component for deviations of the horizontal detector from perfect cosine response following the work of Harrison *et al.* Harrison et al. (1994). Corrections to the diffuse component are made using the isotropic sky assumption following the work of Leszczynski *et al.* Leszczynski et al. (1998). The total horizontal component is then recalculated based on the "cosine corrected" direct and diffuse values. The resulting voltages are averaged into 3 minute bins for each of the direct, diffuse and total components. These 3 minute average voltages are then transformed into units of irradiance via either the filter calibration functions or by the Langley calibrations described earlier. The irradiance measurements used in this work were calibrated via the Langley technique and therefore only uncertainties for this calibration are used in creating the input error budget. Fourteen of the resulting 21 irradiances (7 direct, 7 diffuse) are the final products used in the measurement vector $\mathbf{y}$ of the retrieval algorithm.

4b. *The Forward Model (TUV)*

The retrieval framework was built around the Tropospheric Ultraviolet-Visible (TUV) radiative transfer model which was developed by Sasha Madronich at the National Center for Atmospheric Research (NCAR), located in Boulder, Colorado
Madronich (1993). As discussed in Goering *et al.* this model was chosen based on its flexibility and previous use in other research projects for ultra-violet studies Goering et al. (2005). Extensive sensitivity studies were undertaken to first determine the ideal version of the radiative transfer solver used in TUV. The model, as provided by NCAR, can solve the radiative transfer equation using either the 2-stream method or the multi-stream Discrete-Ordinate method (DOM). Recall that the 2-stream method implies that

the radiative transfer equation is solved by treating only a single upward and downward component of the beam. There are nine different approximations available within TUV for solving via the 2-stream method but only the Delta-Eddington approximation Toon et al. (1989) was tested. The DOM solves the basic radiative transfer equation by discretizing it into a set of first-order differential equations, which can be done for both isotropic and anisotropic scattering Liou (2002). The n-stream DOM within the TUV code, can be set to run in a number of modes, where 'n' is an even integer between 2 and 32 Stamnes et al. (1988). In general, the larger the value of "n" the more accurate the results, but the slower the computation time.

Based on the studies to be presented in Section ii, the 4-stream DOM was selected as the ideal operational mode. After the ideal operational mode was determined, testing was undertaken to assess the relative importance of the various physical assumptions used as inputs (constraints) in the model. Furthermore, as discussed in the following sections, several modifications were implemented to the code framework in order to enhance the time efficiency of the retrieval algorithm. All of these changes involved input parameters which are fed into the model as well as loops over which the model is iterated. No changes were made to the actual Discrete Ordinate or Delta-Eddington radiative transfer subroutines within the code.

i. TUV Settings User defined inputs to the operational version of the TUV model include the date, time and SZA, which in this case, are all read from the input irradiance data file. The site latitude, longitude, altitude and time-offset from GMT are all specified in a model input file. The input file also contains settings for the spectral range, which is set to 296- to 372-nm, spectral increment, the number of atmospheric levels, 51 in this study and the level increments. The model can also treat clouds, but all input data are cloud screened in this study, so these settings were nullified. The vertical temperature

profile used in the TUV code is that of the U.S. Standard Atmosphere (1976) which are annual means calculated at 45° North latitude. The vertical distribution of air molecules currently used in the model is provided by scaling the U.S. Standard Atmosphere number density profile from the given local site altitude and sea level pressure. Rayleigh scattering cross sections are then calculated from the WMO 1985 report (which are taken from the original work by Nicolet Nicolet (1984)). For the O_3 vertical profile the total column amount from the current iteration of the algorithm is scaled to the U.S. Standard Atmosphere ozone number density profile. From this profile ozone optical depths are calculated at each level using the temperature profile for temperature corrections. Absorption optical depths of NO_2 and SO_2 are calculated at each layer in the model atmosphere by scaling the user inputted column amount to a fixed vertical profile. A vertical profile of O_2 absorption is calculated assuming 21% by volume of the air density.

A sensitivity study of the TUV forward model similar to that performed by Schwander *et al.* using the STAR radiative transfer model Schwander et al. (1997) was undertaken. For all of the forward model testing the model was iterated over 10 values of AOD (0.1 to 2.0 in increments of 0.21) and 10 values of SSA (0.65 to 0.95 in increments of 0.033) for SZA 25°, 45° and 65°. Contour maps of the modeled irradiances over the AOD-SSA domain space were created for each of the 7 channels for both direct and diffuse beams. As an example, Figure 10 shows the irradiance maps over the AOD-SSA domain space for the direct beam at wavelengths 300- and 368-nm and for SZA 25°, 45° and 65° produced from the 32-DOM model run. The attenuation is strongly dependent on both the wavelength and SZA, as should be expected due to absorption by ozone and to traversing more atmosphere, respectively. For the direct beam, the irradiances are independent of SSA, as deduced from the vertical striations in the plots, consistent with the fact that the direct beam is a measure only of photons which have not been scattered in the atmosphere.

Figure 11 shows the diffuse irradiances calculated using the same model conditions as for the direct beam. By comparing Figure 10 with Figure 11 it is apparent that the values of the diffuse irradiance component are of the same order of magnitude as the direct component, indicating that diffuse scattering is a significant phenomena within the UV spectral range, as was discussed previously in Chapter 2. As with the direct beam, the diffuse beam is attenuated by approximately two orders of magnitude from 300- to 368-nm and is attenuated by about half from 25° to 45° SZA. At SZA 65° there is virtually zero signal at 300-nm. A major difference between the direct and diffuse irradiances is the SSA dependent features present in the diffuse beam, indicating that there is some information available in the measurements pertaining to the SSA of the local atmosphere.

Percent differences, or uncertainties in modeled irradiances, are calculated from irradiance maps such as those presented in Figures 10 and 11. This is done by comparing modeled irradiances from a "truth" run to irradiances from a "perturbed" run, where all other parameters are held fixed. Testing of this sort was performed for the radiative transfer solver approximation, as well as for various physical parameters, i.e., ozone, asymmetry factor, etc., as will be discussed in the following sections.

ii. Testing of the Radiative Transfer Solver To test the sensitivity of the calculated irradiances to the particular radiative transfer solver, TUV was run using several different solvers that are available within the code. Irradiance data was obtained for the Panther Junction, Texas site (see Sec. 6a for more details concerning the site) and the following constraints were set in the model: TOC = 286 DU, asymmetry factor (g) = 0.7 and surface albedo (α_s) = 0.10. Percent differences in irradiances over the domain space due to the mode approximation relative to the 32-stream DOM approximation, which was taken to represent "truth", were calculated as,

Table 3: **Percent error in the 4-stream DOM approximation.**

300nm	305nm	311nm	317nm	325nm	332nm	368nm
1.08%	0.42%	0.45%	0.73%	0.58%	0.52%	0.73%

$$\Delta(I) = \frac{I_{(n=x)} - I_{(n=32)}}{I_{(n=32)}} * 100, \tag{84}$$

4-stream vs. 32-stream DOM The percent difference maps of the diffuse irradiances (direct irradiances are not affected) for the 4-DOM versus 32-DOM at wavelengths 300-nm (left column) and 368-nm (right column) are shown in Figure 12 for SZA 25° (top row), SZA 45° (middle row) and SZA 65° (bottom row). These figures indicate that at SZA 25° and 45° there is very little error in the 4-DOM approximation relative to the 32-DOM for all AOD, SSA and wavelength. At SZA 65° the dependence in error on AOD becomes somewhat pronounced, ranging from about +1% at AOD 0.2 to about +4% at AOD 1.0 at 300nm, but still shown no dependence on SSA. At 368-nm the range in error is much smaller and flatter with AOD, ranging from about -2% to +1% over the domain space. Based on these results, an uncertainty value for each wavelength was calculated to represent all AOD, SSA and SZA conditions by averaging the error at 2 points in the AOD-SSA domain for the 3 SZA. The final wavelength-dependent averaged error values are presented in Table 3.

Although it might be considered desirable to implement an input error budget dependent on AOD, SSA and SZA, the range of the errors due to the 4-DOM approximation is relatively small over these realistic domains, making the approximation of a domain-independent error budget justified. A more accurate representation of the input error would not much alter the retrieval results, and may unnecessarily complicate the retrieval code. Furthermore, it should be noted that the current cloud screening algorithm is based

Table 4: **Forward model run times for various radiative transfer solvers.**

Model mode	Delta-Eddington	DOM-2	DOM-4	DOM-8	DOM-32
seconds	120	1060	1138	1709	26,177
minutes	2	17.7	19	28.5	436

on variability in AOD Smirnov et al. (2000) and, as such, most of the cloud screened scans remaining have SZA $< 65°$.

8-stream vs. 32-stream DOM Shown in Figure 13 are the irradiance uncertainties calculated for the 8-DOM versus 32-DOM model runs. The irradiance uncertainties are essentially zero over the entire AOD-SSA domain space for both 300- and 368-nm and all SZA, indicating excellent accuracy relative to the 32-stream mode. Although the original Goering *et al.* algorithm relied on the 8-DOM version of the radiative transfer code Goering et al. (2005), the studies discussed here indicate that the 4-DOM approximation gives the ideal combination of accuracy and speed. As shown in Table 4, the 4-DOM model required 19 minutes to run calculations over the 100 point domain space, the 8-DOM required 28.5 minutes while the 32-DOM mode required 436 minutes on a 3 GHz desktop processor.

Delta-Eddington vs. 32-stream DOM For comparison the percent difference in irradiances for the Delta-Eddington versus the 32-DOM mode over the AOD-SSA domain space are shown in Figure 14 for wavelengths 300- and 368-nm at SZA 25°, 45° and 65°. The Delta-Eddington approximation gives a large variability in the percent differences, which are also strong functions of wavelength, SZA and AOD. For example, even at 25° the range in percent difference spans from about +1% to about -10% over AOD-SSA domain for the 300-nm case. For the 368-nm case the error is flatter with AOD at 25° and 45° but the range in error is about 6%, while at 65° the AOD dependence

becomes stronger and spans from about +3% to about +15% over AOD-SSA domain space. These results indicate that, although the Delta-Eddington approximation provides a much faster retrieval, the magnitude of the input error budget is significantly larger and more variable than that of the 4-DOM approximation. In fact the size of the errors for the Delta-Eddington approximation, relative to the 32-DOM, become larger than those of the instrument measurement and calibration uncertainties. Thus the uncertainty in the radiative transfer solver would become the dominant source of error in the retrieval algorithm if the Delta-Eddington approximation were used.

However, use of the Delta-Eddington mode is beneficial under certain conditions due to its speed. For example, the retrieval algorithm was modified to require a minimum of 2 iterations, even if convergence occurred on the first (which rarely happens), with the Delta-Eddington approximation used on the first iteration. This method allows for a nudging towards the solution using the relatively fast Delta-Eddington approximation, followed by the more accurate, but slower, 4-DOM approximation on all subsequent iterations. Typically a retrieval converges on 3 to 4 iterations.

There is also a possibility that the Delta-Eddington approximation can provide a self consistent means of cloud screening the irradiance data set by way of failed convergences or out of bound statistical significance. This would be done in lieu of relying on precalculated values of AOD from the Langley method as used in the Smirnov cloud screening algorithm Smirnov et al. (2000). Initial testing of this method is described in Section v.

iii. Perturbation testing In order to calculate the mxn elements of the Jacobian matrix, $\mathbf{K}$, the radiative transfer code within the forward model is actually evaluated $n + 1$ times per iteration of Eqn. 62, where n is the number of unknown retrieval parameters. The additional call to the forward model is required to produce the values for $\mathbf{F}(\mathbf{x})$ using the unperturbed values of the state parameters. For each of the n model runs one

of the state variables is perturbed by some predetermined percentage (2% in the current algorithm based on the work of Goering *et al.*), a range over which the forward model is approximately linear. In the Goering *et al.* scheme, $n = 15$, whereas $n = 16$ in the new scheme due to the introduction of the asymmetry factor into the retrieval vector as will be discussed later. The minimum allowed iterations of the retrieval equation (Eqn. 62) in the current algorithm is 2 while the maximum allowed is 6. However a typical retrieval requires 3 to 4 iterations for successful convergence, yielding $17 * 3 = 51$ or $17 * 4 = 68$ calls to the radiative transfer calculation. Recall that we are interested in time efficiency as this algorithm is to be implemented operationally on a suite of approximately 30 instruments, each collecting a daily data set consisting of approximately (10 hours/day) * (20 scans/hour) = 200 scans/day per instrument. This yields a total of approximately 6000 non-cloud screened scans/day which will need to be run through the algorithm.

As discussed in Rodgers' text Rodgers (2000) the weighting functions, which are taken from the rows of $\mathbf{K}$, contain information of the sensitivity of the model to perturbations in the state parameters. In other words it is a model sensitivity covariance matrix. Recall from Eqn. 60 that the elements of $\mathbf{K}$ are produced within the retrieval algorithm by first slightly perturbing the state parameter and then running the forward model to produce irradiances at each wavelength channel used in the retrieval. The perturbation to a single parameter has little effect on the modeled irradiances at the other channels as deduced from the sharp spikes in the weighting functions as shown in Figure 15 for the noon-time test scan. For example, a 2% perturbation to the value of AOD_{368-nm} produces only non-zero values in the AOD_{368-nm} element of the row in the $\mathbf{K}$ matrix corresponding to the 368-nm direct beam. Therefore it was determined that the number of evaluations of the radiative transfer code could be reduced to a single call for all seven AOD by perturbing all seven simultaneously. The same was done for the seven values of SSA, resulting in a total number of runs of the model per retrieval iteration to 1 (AOD)

Table 5: **Range of values and increments of the physical parameters inputted to the TUV forward model.**

Parameter	Min	Max	Number	Increment
AOD	0.1	2.0	10	0.21
SSA	0.65	0.95	10	0.033
SZA	25	65	3	15
TOC	200	400	5	50
TOC	260	300	5	10
g	0.6	0.9	7	0.05

+ 1 (SSA) + 1 (TOC) + 1 (g) + 1 (unperturbed) = 5.

This modification produced no perceptible changes to $\mathbf{K}$, and hence negligible changes in the retrieved parameters or in the diagnostic outputs. As shown in Figure 16, there is no difference in the retrieved state vectors from the noon time test scan, but the algorithm computation time was reduced from 197 seconds to 56 seconds (3.5 times faster) for a 3 iteration retrieval. This reduced perturbation scheme was incorporated into all subsequent versions of the retrieval code.

iv. Physical parameter testing To test the sensitivity of the model to the physical input parameters the forward model was evaluated over the same 100 grid-point domain in AOD-SSA space at SZA 25°, 45° and 65° using the 4-DOM approximation for various values of ozone, asymmetry factor, and surface albedo. To determine the appropriate range of values of these three physical input parameters current literature was consulted, e.g., Wenny et al. (1998), Wenny et al. (2001), Wetzel et al. (2003), Petters et al. (2003), Goering et al. (2005). The range of values and increments used for AOD, SSA, SZA, TOC and g are summarized in Table 5, while Table 6 summarizes the surface albedo regimes tested.

The testing shows that the forward model sensitivity to realistic values of the parameters (in decreasing order) is TOC, g then α_s. TOC had already been incorporated as a

Table 6: **Surface albedo regimes inputted into the TUV forward model.**

Regime 1	Regime 2	Regime 3	Regime 4	Regime 5	Regime 6
0.04	DG desert	DG pine	DG grnfarm	DG brnfarm	DG snow

retrieval parameter in the original version of the retrieval algorithm. Since the sensitivity of the model is comparably large to asymmetry factor as it is to TOC, as will be shown, it was decided that the retrieval would be greatly improved if asymmetry factor could successfully be added without harming the error budget, the statistical significance or the information content. Forthcoming discussion indicates that asymmetry factor was added into the retrieval and that it increased the value of the results.

Total Column Ozone Although TOC was already incorporated into the algorithm as a retrieval parameter, model sensitivity testing to changes in TOC were performed so that the relative importance of this parameter could be assessed. Table 5 shows the size and range of TOC for the two different scenarios; large, 50 Dobson Units (DU) and small, 10 DU, increments. The percent differences in modeled irradiances at the 7 diffuse wavelengths for a thin atmosphere (AOD = 0.311 and SSA = 0.850) are summarized in Table 7 for both incremental scenarios. Note that the results are essentially the same for any point in domain space so, for brevity, only the one point (in this case the thin atmosphere) is listed. Furthermore the percent difference in modeled irradiances is nearly the same for the direct and diffuse beams so only the numbers from the diffuse beam are shown for clarity.

The first scenario allowed TOC to vary in relatively large increments of 50 DU. This lead to a large change in modeled irradiances compared to the test case of 300 DU, and as expected there is a strong wavelength dependence to the change since ozone absorbs much more strongly near 300-nm than at 368-nm. It can be noted from comparing the

percent differences at 300-nm for this scenario that the model is not linear with respect to these large deviations and has decreasing sensitivity with increasing TOC. For example the percent difference at 300-nm when TOC is decreased from 300 to 200 DU is +205%, while the difference is only -66% when TOC is increased from 300 to 400 DU.

Since TOC is a relatively slowly varying parameter in the atmosphere it is assumed that a best guess value could be assigned to the algorithm based on a monthly average for any given site, for example from TOMS satellite data or from the direct sun method Gao et al. (2001). This would allow the TOC to be guessed to an accuracy better than 50 DU and therefore the second testing scenario was a variation in TOC in 10 DU increments to better simulate real discrepancies. In this case 280 DU was used as the reference. In this scenario the percent differences at 300-nm indicate that the model is linear with respect to these smaller deviations. The results agree well with sensitivity testing of the STAR radiative transfer model (see Figure 2 of Schwander et al. (1997)) and indicate that the model is moderately sensitive to the TOC at the three lower wavelengths for discrepancies of 10 to 20 DU. Again, due to the logarithmic decline of the ozone absorption cross section with increasing wavelength, the error in TOC decays by an order of magnitude from 300- to 317-nm and is non existent at 368-nm.

Asymmetry Factor (g) To test the forward model sensitivity to changes in the asymmetry factor, g, the value was iterated from 0.60 to 0.90 in increments of 0.05 and the percent differences in irradiances over the domain space were calculated relative to g = 0.70. Note that the direct beam is composed of only unscattered light, and therefore, is not affected by changes in asymmetry factor, which is a function of scattering. The values for the standard thin and thick atmosphere for the diffuse beam at 300- and 368-nm are shown in Table 8. There is virtually no wavelength dependence of model sensitivity to asymmetry factor so only the values at 300- and 368-nm are reported. For the thin atmosphere the sensitivity is slight, spanning an irradiance range of about 8% as asym-

Table 7: **Percent differences in modeled irradiances for various TOC values.**

Versus 300 DU at domain point AOD = 0.311, SSA = 0.850				
λ	**200 DU**	**250 DU**	**350 DU**	**400 DU**
300nm	+205	+74.0	-42.2	-66.3
305nm	+70.6	+30.5	-23.2	-40.7
311nm	+28.3	+13.2	-11.1	-21.3
317nm	+11.3	+5.4	-4.8	-10.1
325nm	+3.6	+2.0	-1.6	-3.2
332nm	+1.0	+0.3	-0.7	-1.0
368nm	0.0	0.0	0.0	0.0
Versus 280 DU at domain point AOD = 0.311, SSA = 0.850				
λ	**260 DU**	**270 DU**	**290 DU**	**300 DU**
300nm	+24.8	+11.6	-10.4	-19.8
305nm	+11.1	+5.3	-5.3	-10.2
311nm	+4.5	+2.7	-2.7	-5.4
317nm	+1.7	+0.6	-1.2	-2.3
325nm	+0.8	+0.4	-0.4	-0.8
332nm	+0.3	+0.3	0.0	0.0
368nm	0.0	0.0	0.0	0.0

metry factor varies from 0.60 to 0.90. As the atmosphere becomes optically thicker the sensitivity increases, spanning an irradiance range of about 23% as asymmetry factor varies from 0.60 to 0.90.

These results indicate that the retrieval sensitivity to changes in asymmetry factor will be on the same order of magnitude as changes in TOC of 10 to 20 DU. Furthermore a single value of asymmetry factor can be used to represent all wavelengths due to the lack of wavelength dependence of this parameter in the model. As discussed later the asymmetry factor was therefore added to the retrieved state vector in order to reduce the estimated errors in the retrieval input. The non-linear nature of the sensitivity of the model to asymmetry factor with respect to AOD indicates that the retrieval will better be able to pick the true value as the AOD increases, a suspicion that will be corroborated in the discussion of the synthetic retrievals in Sec. 5a.

Table 8: **Percent differences in modeled irradiances for various asymmetry factor values versus g = 0.70.**

Thin atmosphere (AOD = 0.311, SSA = 0.850)						
λ	g = 0.60	g = 0.65	g = 0.75	g = 0.80	g = 0.85	g = 0.90
300nm	-2.4	-1.2	+1.2	+2.4	+3.6	+5.0
368nm	-2.7	-1.2	+1.2	+2.4	+3.6	+4.8
Thick atmosphere (AOD = 1.156, SSA = 0.850)						
λ	g = 0.60	g = 0.65	g = 0.75	g = 0.80	g = 0.85	g = 0.90
300nm	-6.7	-3.4	+3.6	+7.4	+11.4	+15.7
368nm	-6.6	-3.4	+3.4	+7.1	+11.0	+15.2

Surface Albedo (α_s) The surface albedo in the UV spectrum has an important role in the radiative transfer calculations of the ground fluxes due to the added complication of the reflection of the incident beam, some of which is radiated back to the surface. To test the sensitivity of the TUV model to this parameter the work of Doda and Green was used in which reflected irradiances above various surfaces were measured at discrete points in the wavelength range 290- to 400-nm using a double monochromator mounted on an airborne platform Doda and Green (1980). They were able to neglect atmospheric contributions by measuring the reflectances at a minimum of three altitudes and using a linear least squares regression to extrapolate to the surface, yielding values of α_s. The wavelength dependence of the surface reflectances were then fit in non-linear least squares fashion to produce an analytical expression of the form

$$R(\lambda) = \frac{R_0 \exp\left[(\lambda - \lambda_0)\right]/\delta]}{\beta + \exp\left[(\lambda - \lambda_0)/\delta\right]}, \tag{85}$$

where $\lambda_0 = 0.300\mu$m, λ = wavelength in microns, and R_0, β and δ are adjustable parameters Doda and Green (1981).

The measurements were made over a broad variety of surfaces including desert sand, pine forest, green farmland, brown farmland and snow cover. Modifications to the TUV

code were performed in order to express the wavelength dependent surface albedos using these analytical forms for each of these surface types. The forward model was then evaluated, i.e., irradiances were calculated, over the AOD-SSA domain space with $g = 0.7$ and TOC = 280 for SZA 25°, 45° and 65° for each of the five surface types listed above with perturbations of ± 0.015, an uncertainty which was taken as half the uncertainty from Schwander *et al.*, as well as for the wavelength independent albedo of 0.04 ± 0.03, exactly as was done in the Schwander *et al* study Schwander et al. (1997). The percent variability in modeled irradiances over the AOD-SSA domain space were then calculated as,

$$\Delta(I) = \frac{(I_{(+)} - I_{(-)})}{I} * 100, \tag{86}$$

where $I_{(+)}$ and $I_{(-)}$ represent the irradiances I calculated with positively perturbed and negatively perturbed α_s, respectively.

Tables 9 and 10 show the percent variability in irradiance for each albedo case at the 7 wavelength channels for three SZA for both a thin atmosphere (AOD=0.311, SSA=0.850) and a thick atmosphere (AOD=1.156, SSA=0.850), respectively, extracted from the uncertainty maps similar to those shown in Figure 17.

The values in the first data column show that when α_s=0.04 is perturbed by ± 0.03, the modeled irradiances are different by less than 2% for both the thick and thin atmosphere for all SZA. These results agree well with those found by Schwander *et al.* in their model uncertainty analysis Schwander et al. (1997). It is clear from these tables that uncertainties in modeled irradiances for the various terrain types are not too different from one another, excepting the case of snow cover. Ideally each instrument site will be classified into one of the four dry types and the corresponding wavelength dependent values of α_s, based on Eqn. 85, will be used in the retrieval scheme. A snow-covered scenario of the retrieval algorithm will also be necessary for most of the sites since the values of α_s and the input error budget will be drastically different under this condition.

Table 9: **Percent differences in modeled irradiances for various surface albedo types with α_s perturbed by $\pm$0.015.**

Thin atmosphere, AOD = 0.311, SSA = 0.85							
SZA	λ	**0.04**	**desert**	**pine**	**grnfarm**	**brnfarm**	**snow**
25°	**300nm**	-1.57	-1.74	-2.96	-1.39	-1.57	+13.0
	305nm	-1.73	-1.73	-3.21	-1.48	-1.72	+17.0
	311nm	-2.73	-1.82	-3.64	-1.82	-2.72	+20.0
	317nm	-1.79	-1.79	-3.57	-1.79	-1.79	+23.8
	325nm	-2.00	-1.60	-3.60	-2.00	-2.40	+25.6
	332nm	-2.11	-1.40	-3.51	-1.75	-2.10	+27.0
	368nm	-1.86	-0.62	-3.10	-2.17	-2.48	+26.6
45°	**300nm**	-0.96	-1.44	-2.40	-0.96	-0.96	+11.1
	305nm	-1.34	-1.35	-2.69	-1.34	-1.34	+14.3
	311nm	-1.74	-1.60	-2.94	-1.47	-1.74	+17.4
	317nm	-1.56	-1.56	-3.12	-1.56	-1.56	+19.5
	325nm	-1.49	-1.00	-2.99	-1.49	-1.49	+21.9
	332nm	-1.69	-1.27	-2.97	-1.69	-2.12	+22.4
	368nm	-1.81	-0.72	-2.89	-2.17	-2.17	+22.0
65°	**300nm**	-0.63	-0.63	-1.89	-0.63	-0.63	+8.2
	305nm	-1.30	-1.30	-2.16	-1.08	-1.30	+10.8
	311nm	-1.10	-1.10	-2.20	-1.09	-1.10	+13.6
	317nm	-1.27	-1.11	-2.22	-1.11	-1.27	+15.3
	325nm	-1.72	-1.72	-2.59	-1.72	-1.72	+16.4
	332nm	-0.69	-0.69	-2.08	-0.69	-1.39	+17.4
	368nm	-1.09	-0.54	-2.17	-1.09	-1.63	+15.8

For each of the five dry surface albedo types the results as a function of wavelength and SZA were similar. Figure 17 shows the results for the select case using the Doda and Green desert sand albedos. These plots of percent variability in irradiance (shown only for 300- and 368-nm) span a range of about 0 to 3% across the entire domain space for both wavelengths and all SZA tested. An average value calculated from the thin (AOD=0.311) and thick (AOD=1.156) atmosphere case (averaged for all 5 surface conditions) was calculated at each wavelength for the direct and diffuse beam for use in the model input error budget.

Table 10: **Percent differences in modeled irradiances for wavelength dependent surface albedo types versus the wavelength independent α_s = 0.07.**

Thick atmosphere, AOD = 1.156, SSA = 0.85

SZA	λ	0.04	desert	pine	grnfarm	brnfarm	snow
25°	300nm	-1.05	-1.05	-1.92	-0.87	-1.05	+8.9
	305nm	-1.23	-1.23	-2.22	-0.99	-1.23	+11.1
	311nm	-0.90	-0.90	-2.70	-0.90	-0.90	+12.6
	317nm	-1.16	-1.16	-2.31	-1.16	-1.16	+14.5
	325nm	-1.14	-0.76	-1.89	-1.13	-1.14	+15.5
	332nm	-0.97	-0.65	-1.94	-0.97	-1.29	+15.8
	368nm	-1.24	-0.25	-1.73	-1.24	-1.49	+15.1
45°	300nm	-1.08	-1.08	-1.61	-0.54	-1.08	+8.1
	305nm	-1.00	-1.00	-2.00	-1.00	-1.00	+10.0
	311nm	-1.04	-1.04	-1.92	-1.04	-1.04	+11.7
	317nm	-0.85	-0.85	-1.70	-0.85	-0.85	+13.7
	325nm	-1.06	-0.53	-1.59	-1.06	-1.06	+14.3
	332nm	-0.88	-0.88	-1.76	-0.88	-1.32	+14.1
	368nm	-0.99	-0.33	-1.66	-1.32	-1.32	+13.2
65°	300nm	-0.78	-0.78	-1.56	-0.78	-0.78	+7.0
	305nm	-0.85	-0.85	-1.71	-0.85	-0.85	+8.8
	311nm	-0.98	-0.98	-1.95	-0.98	-1.46	+9.8
	317nm	-0.85	-0.85	-1.70	-0.85	-1.06	+11.5
	325nm	-1.03	-0.79	-1.71	-0.91	-1.03	+12.1
	332nm	-0.90	-0.90	-1.80	-0.90	-0.90	+12.6
	368nm	-0.65	-0.00	-1.31	-0.65	-1.30	+11.1

The Schwander *et al.* sensitivity study of the STAR radiative transfer model showed that the uncertainties in modeled irradiances due to a change in surface albedo are independent of solar zenith angle for a Lambertian surface Schwander et al. (1997). Our current study using the TUV model agrees reasonably well with this notion for the snow free surfaces out to at least 65°. This supports the claim made by Doda and Green that there has been evidence in the literature indicating isotropic scattering for green farmland and pine forest out to 75° Doda and Green (1980). However for the snow covered surfaces our current study shows that the magnitude of change in modeled irradiance

is inversely proportional to increasing SZA. For the snow version of the retrieval algorithm it is therefore important to characterize the model input error as a function of SZA. This discussion highlights the importance of having a semi-daily, accurate and repeatable assessment of snow conditions in order to characterize the input errors during snowy scenes. This could be of great importance to the quality of the retrieval at particular sites during cold seasons of the year. Each site in the UVMRP network contains a downward looking photometer which can be used to identify snowy scenes.

Unknown sources of error Based on the study of Schwander *et al.*, the remaining sources of error in modeling UV irradiances are derived from vertical profiles of temperature, air density and humidity as well as the vertical profile of ozone, NO_2, SO_2 and the aerosol extinction. Initial testing was performed on the TUV model with perturbations to column amounts of NO_2 and SO_2, with the result that the model is fairly insensitive to these quantities at 368-nm. However this may not be true at lower wavelengths where sensitivity to SO_2 is more significant (see Figure 5 of Schwander et al. (1997). Sensitivity testing was not undertaken for the vertical distributions of the remaining quantities. All of the untested sources were assigned a combined estimated uncertainty of 2.5% at all channels.

4c. *Combined Estimated Uncertainties*

Based on the current study estimates for the total errors due to the model and measurements were made for both the direct and diffuse beams at each of the seven wavelengths for the snow-free surface version of the algorithm. Assuming random and independent errors, uncertainties are calculated by the square-root of the sum of the squares of the individual uncertainties,

$$\delta = \sqrt{\sum_{i=1}^{x} (\delta_i)^2}, \tag{87}$$

where, in this particular case $\delta_1 = \delta_{Langley}$, $\delta_2 = \delta_{measurement}$, $\delta_3 = \delta_{rad\ tran}$, $\delta_4 = \delta_{albedo}$ and $\delta_5 = \delta_\epsilon$ which result from the Langley calibration correction factor, the uncertainties in the instrument measurements, the error in the 4-stream Discrete Ordinate approximation, the error associated with a ± 0.015 uncertainty in α_s and error due to all other unaccounted for sources, respectively.

Table 11 summarizes the various assumed dependences of each of the five uncertainty types as was discussed in the text. Note that although some of the uncertainties were calculated as average values for AOD-SSA and/or SZA, the retrieval itself uses only an error budget depending on wavelength and beam type, meaning entries for the last two columns in Table 11 are "No" for all uncertainty types. As an example, the uncertainty due to the Langley calibration factor was calculated individually for each of the 7 wavelengths, but no discrepancy was made between the direct and diffuse beams or changes in the AOD, SSA or SZA. That is, the same value of uncertainty for each wavelength was used in the $\mathbf{S_y}$ matrix, regardless of the AOD, SSA and SZA. Although incorporation of a AOD-SSA-SZA dependent error budget would be slightly more realistic, deviations in the errors are small enough that minimal effect would be seen on the retrieved values. Based on this analysis the final error budget was calculated from Eqn. 87 for the 7 channels, direct and diffuse, and is shown in Table 12.

The final values for the snow free retrieval have been used as inputs into the model-measurement error matrix ($\mathbf{S_y}$) used in the retrieval algorithm. Currently all off-diagonal elements have been assigned values equal zero since cross-correlations have yet to be determined.

Table 11: **Assumed dependences of the five uncertainty types used in creating the model-measurement error budget for the retrieval algorithm.**

Uncertainty	λ	Beam	AOD-SSA	SZA	Note
Langley	Yes	No	No	No	λ-dep. values from Slusser et al. (2000)
Measurements	No	No	No	No	Avg of 2 AOD and 2 SZA from Krotkov et al. (2005)
Model Mode	Yes	Yes	No	No	No contribution to direct beam
Albedo	Yes	Yes	No	No	No contribution to direct beam
Unknown	No	No	No	No	2.5% for all channels

Table 12: **Averaged percent uncertainties in model-measurement error budget (S_y) used in the retrieval.**

	300nm	305nm	311nm	317nm	325nm	332nm	368nm
Direct	5.11%	5.03%	4.89%	4.82%	4.68%	4.54%	4.01%
Diffuse	5.56%	5.25%	5.11%	5.11%	4.97%	4.83%	4.37%

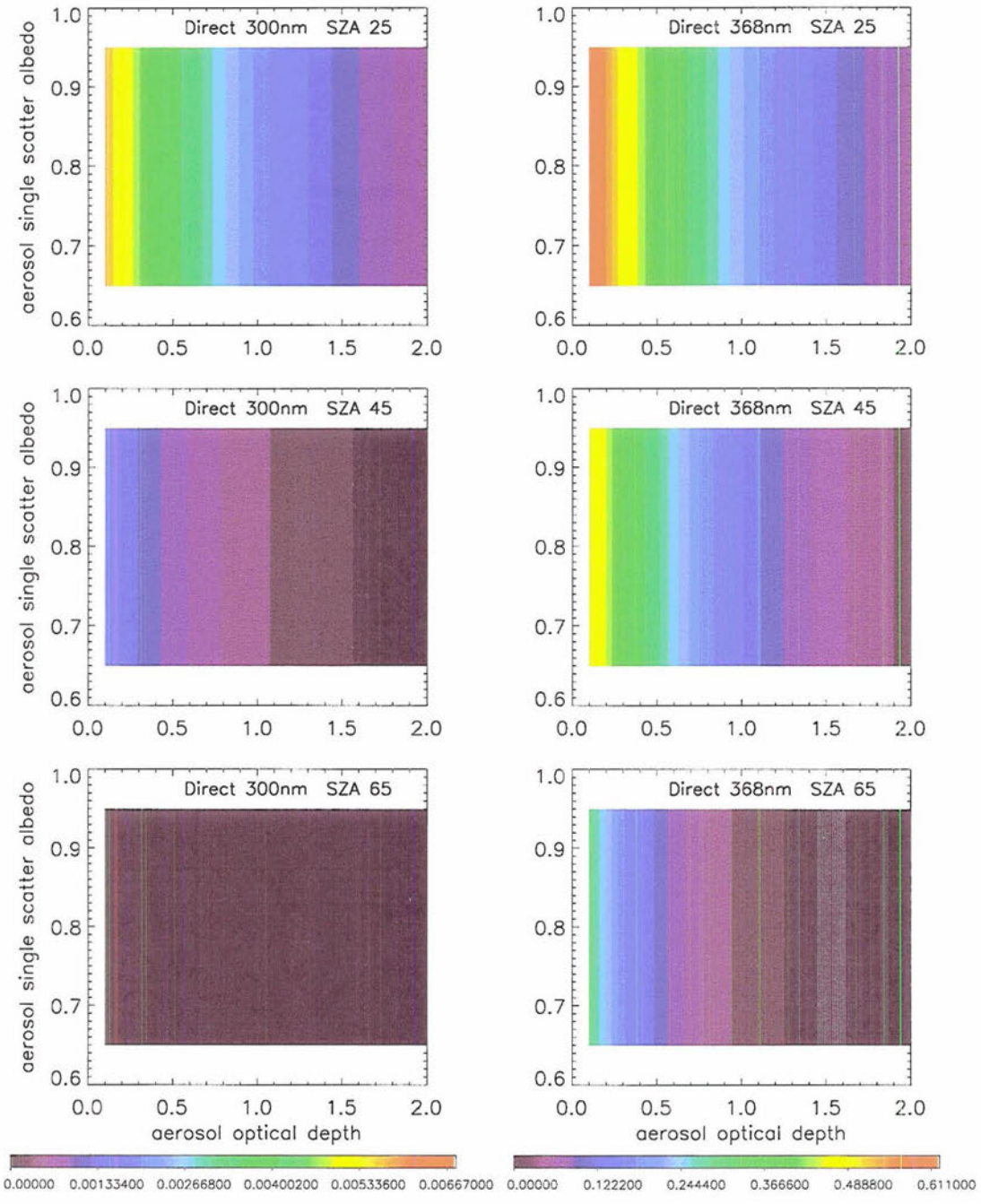

Figure 10: Irradiance maps of the direct beam produced by TUV using the 32-stream Discrete Ordinate approximation. All plots are in AOD-SSA space with a common color scheme. Left column corresponds to 300-nm and right column to 368-nm. Top row corresponds to SZA 25°, middle row to SZA 45° and bottom row to SZA 65°.

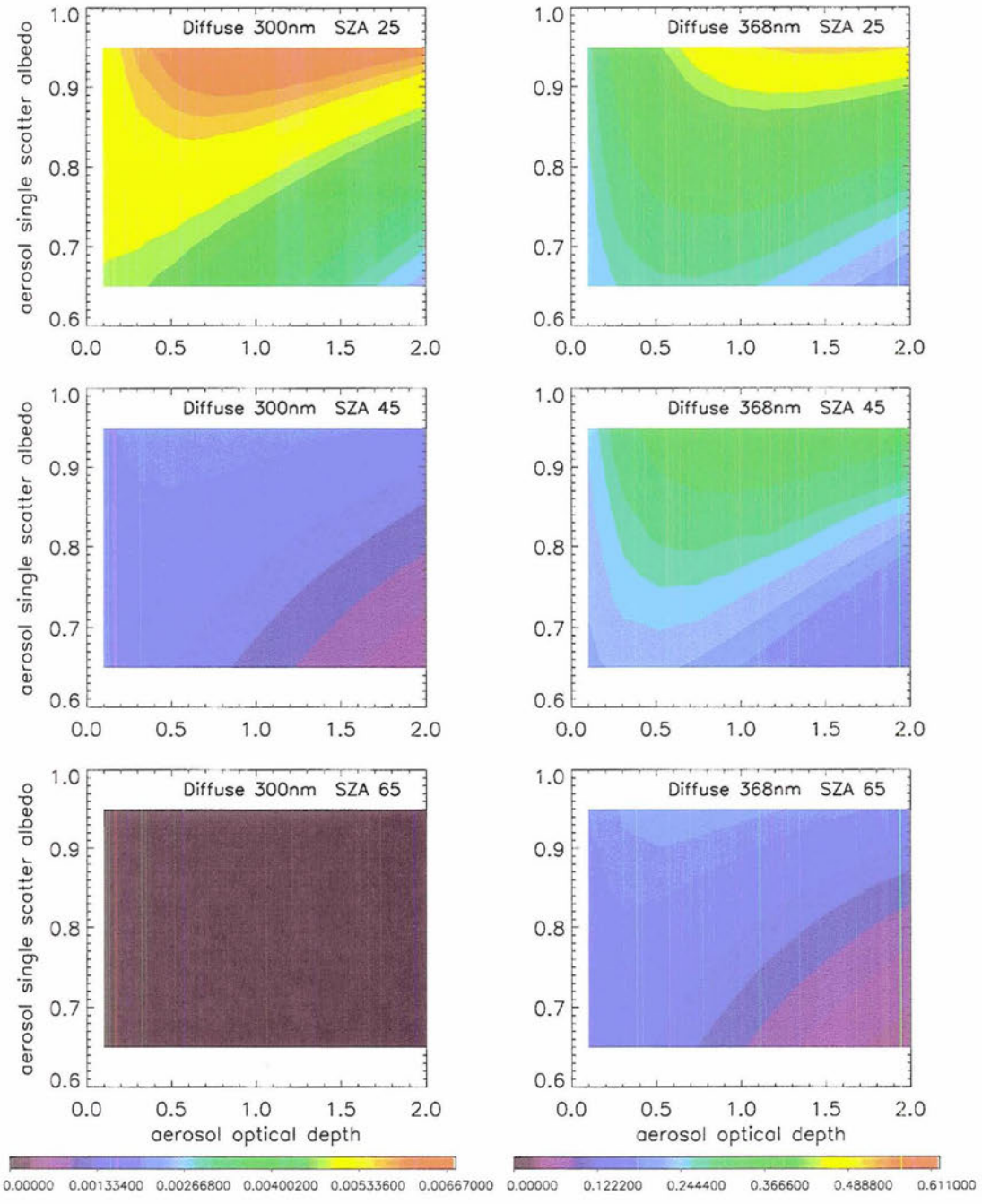

Figure 11: Same as Figure 10, but for the diffuse component of radiation. All plots are in AOD-SSA space with a common color scheme. Left column corresponds to 300-nm and right column to 368-nm. Top row corresponds to SZA 25°, middle row to SZA 45° and bottom row to SZA 65°.

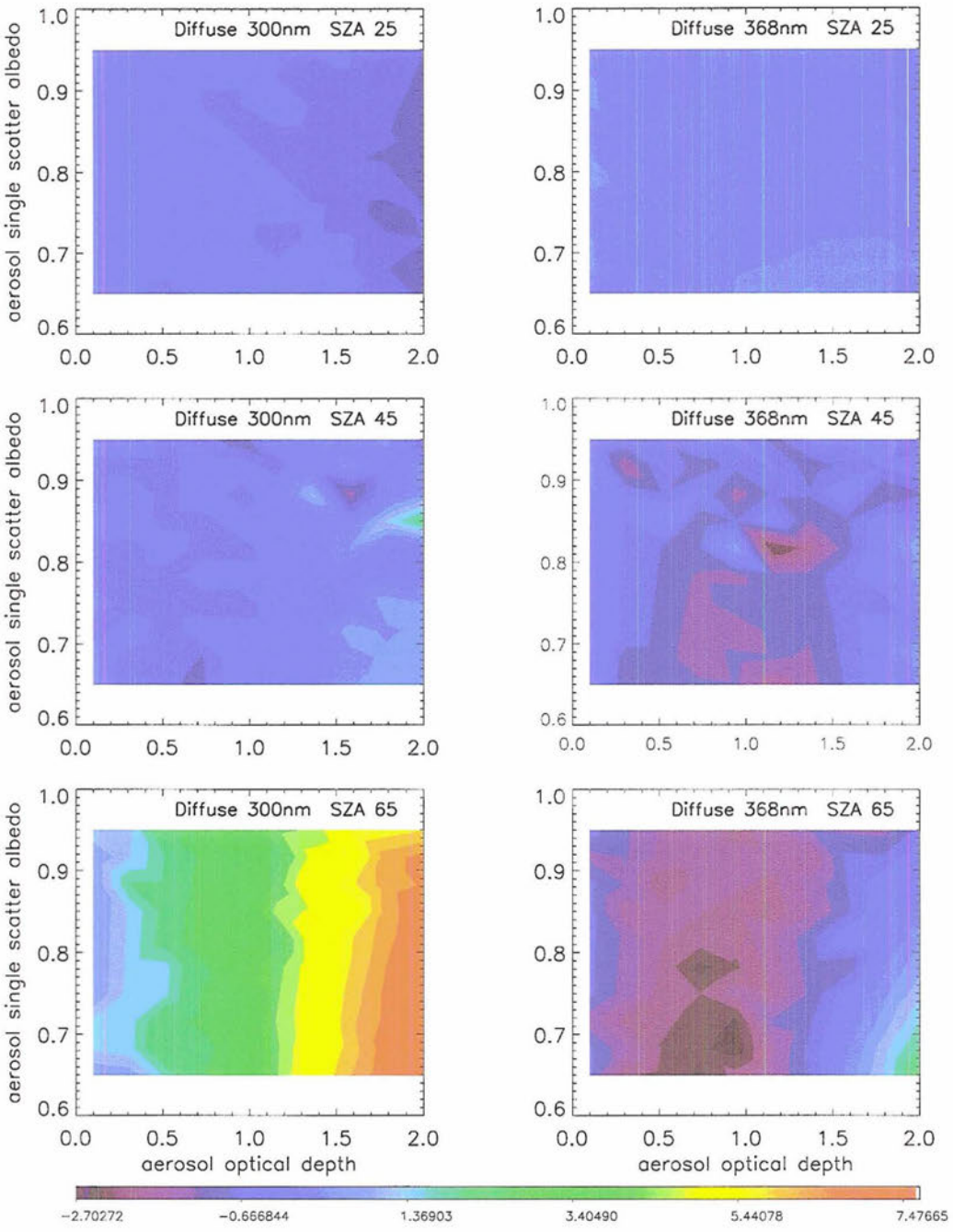

Figure 12: Percent differences in modeled irradiances produced by the 4-stream versus the 32-stream Discrete Ordinate approximation used in the TUV model. All plots are in AOD-SSA space with a common color scheme. Left column corresponds to 300-nm and right column to 368-nm. Top row corresponds to SZA 25°, middle row to SZA 45° and bottom row to SZA 65°.

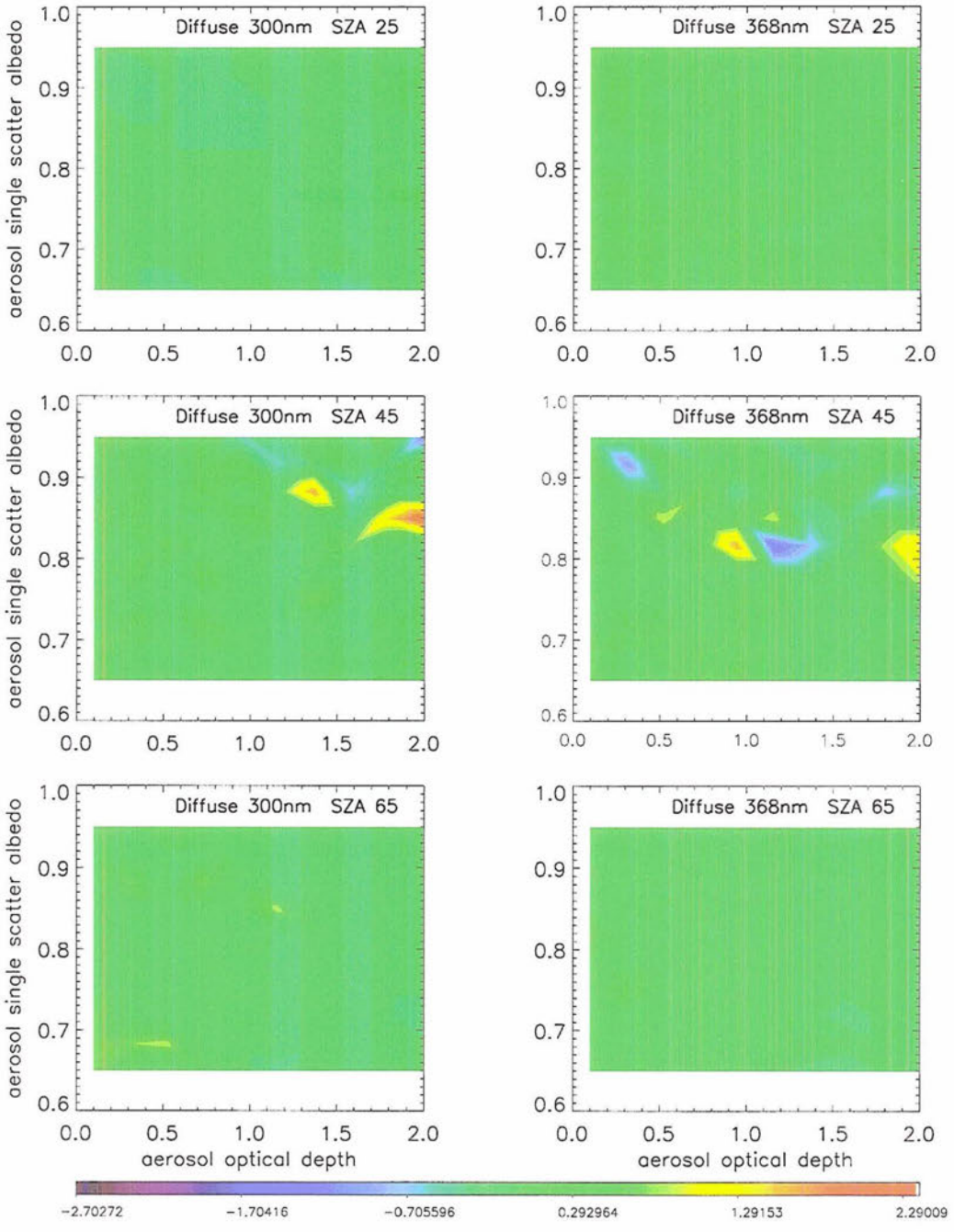

Figure 13: Same as in Fig 12, but for the 8-stream versus the 32-stream Discrete Ordinate approximation. All plots are in AOD-SSA space with a common color scheme. Left column corresponds to 300-nm and right column to 368-nm. Top row corresponds to SZA 25°, middle row to SZA 45° and bottom row to SZA 65°.

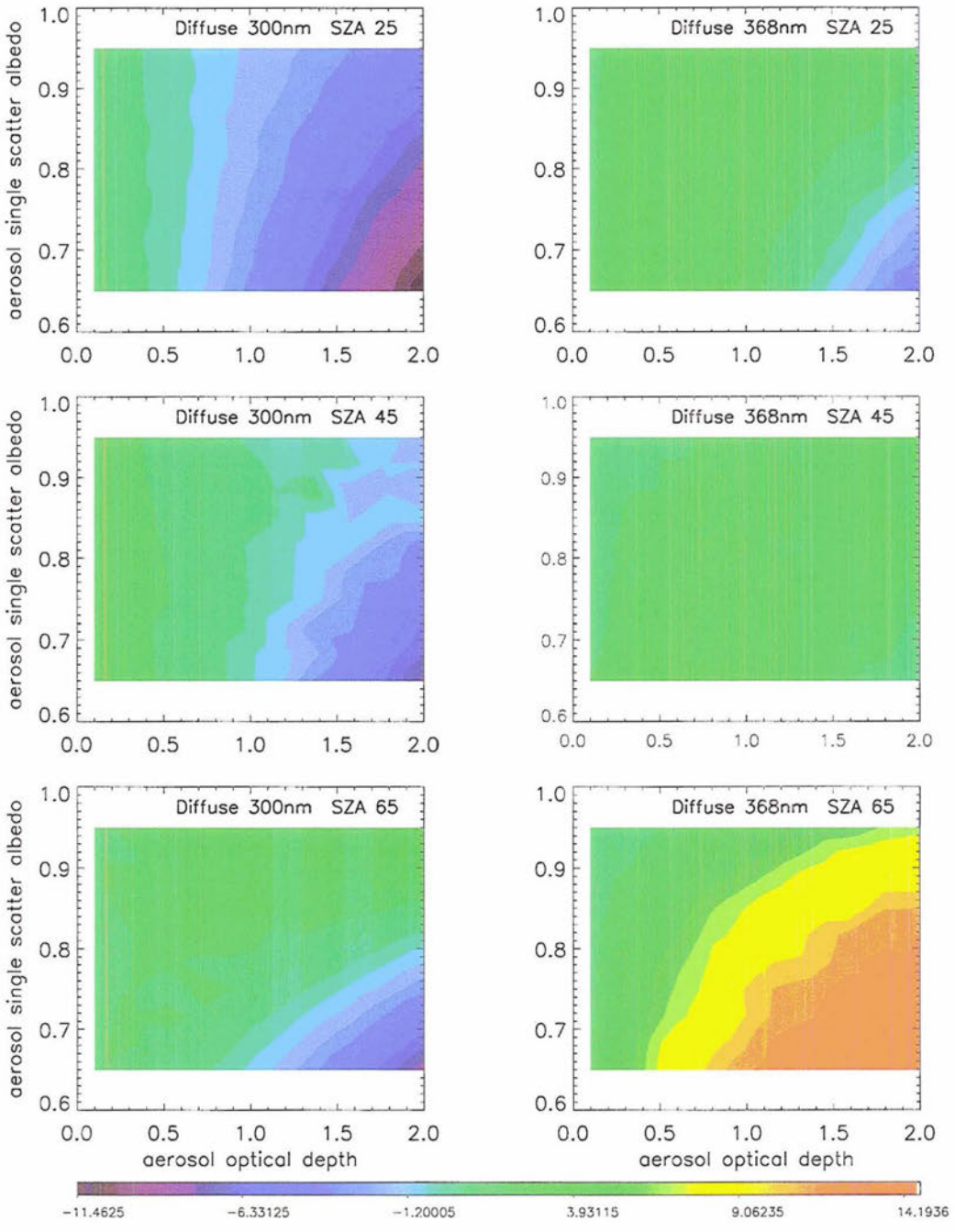

Figure 14: Same as in Fig 12, but for the 2-stream Delta-Eddington approximation versus the 32-stream Discrete Ordinate approximation. All plots are in AOD-SSA space with a common color scheme. Left column corresponds to 300-nm and right column to 368-nm. Top row corresponds to SZA 25°, middle row to SZA 45° and bottom row to SZA 65°.

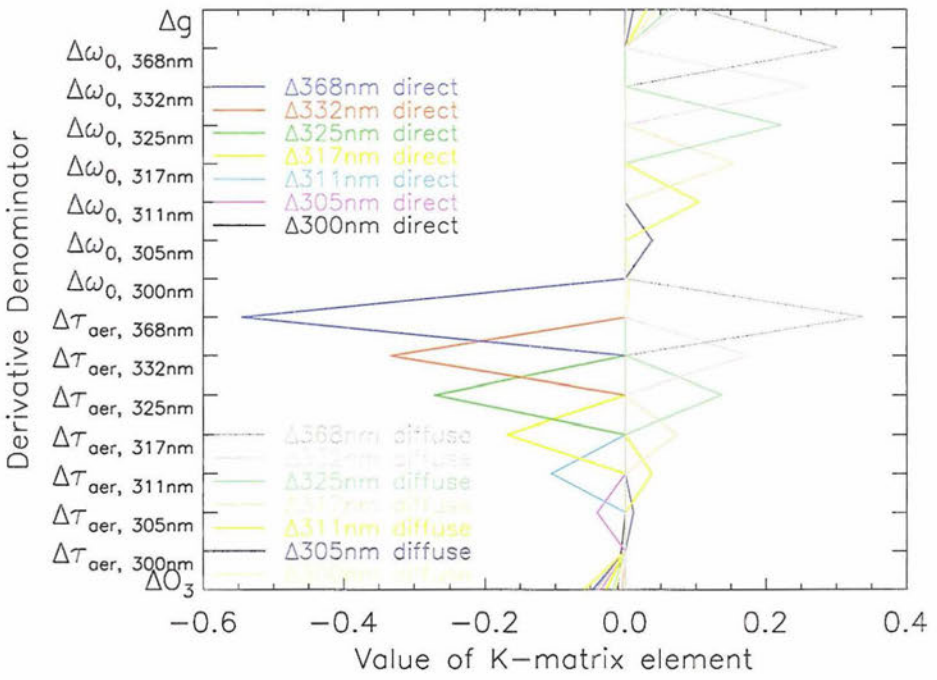

Figure 15: Weighting functions for the noon time test scan retrieval at Panther Junction, Texas. Each channel, direct and diffuse, is plotted as a different color and represents the change in the modeled irradiances at all other channels to a small perturbation in the particular state parameter. Sharp spikes in each channel indicate the independence of the model sensitivity to other channels to changes in the state.

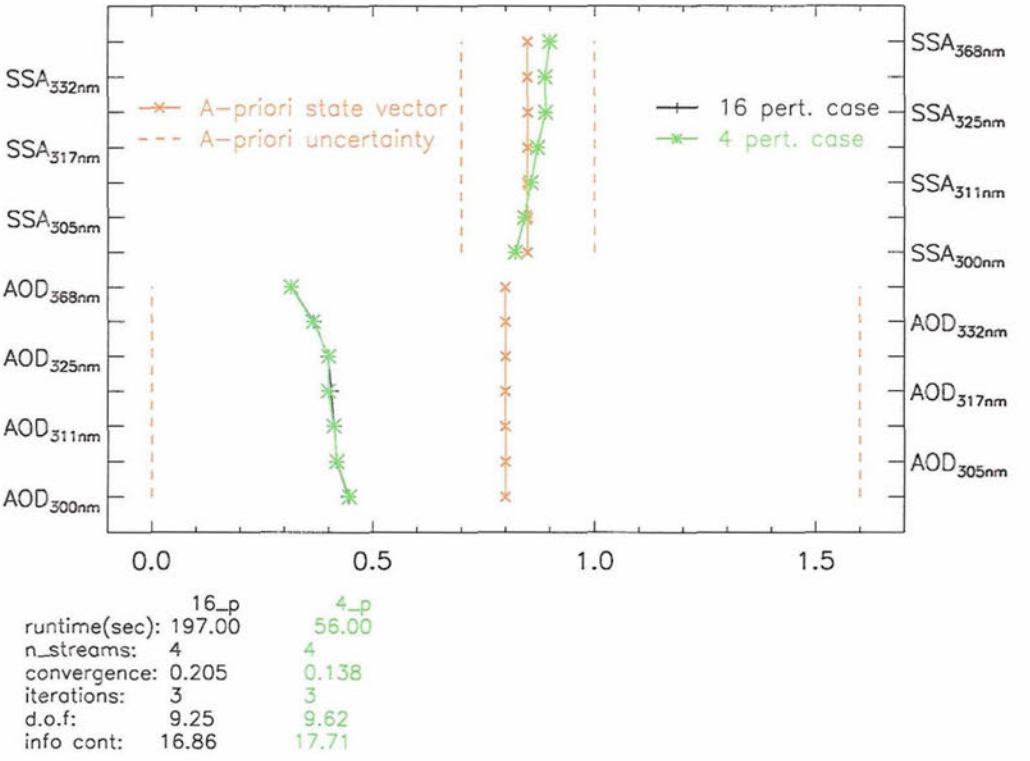

Figure 16: Comparison of retrieved AOD and SSA for two perturbation methods. The *a priori* values are plotted as red "x" and *a priori* uncertainties are shown as dashed lines. Plotted as black stars with connecting solid lines are the results from the original method in which each of the 16 parameters is perturbed independently (16_p). Plotted as blue stars with connecting solid lines are the results from the updated method for which both the 7 AOD are perturbed at once and the 7 SSA are perturbed at once (4_p). The model run-time, DOM stream number, retrieval convergence values, number of retrieval iterations, dof_s and Shannon information content are also listed below the plot in the corresponding colors.

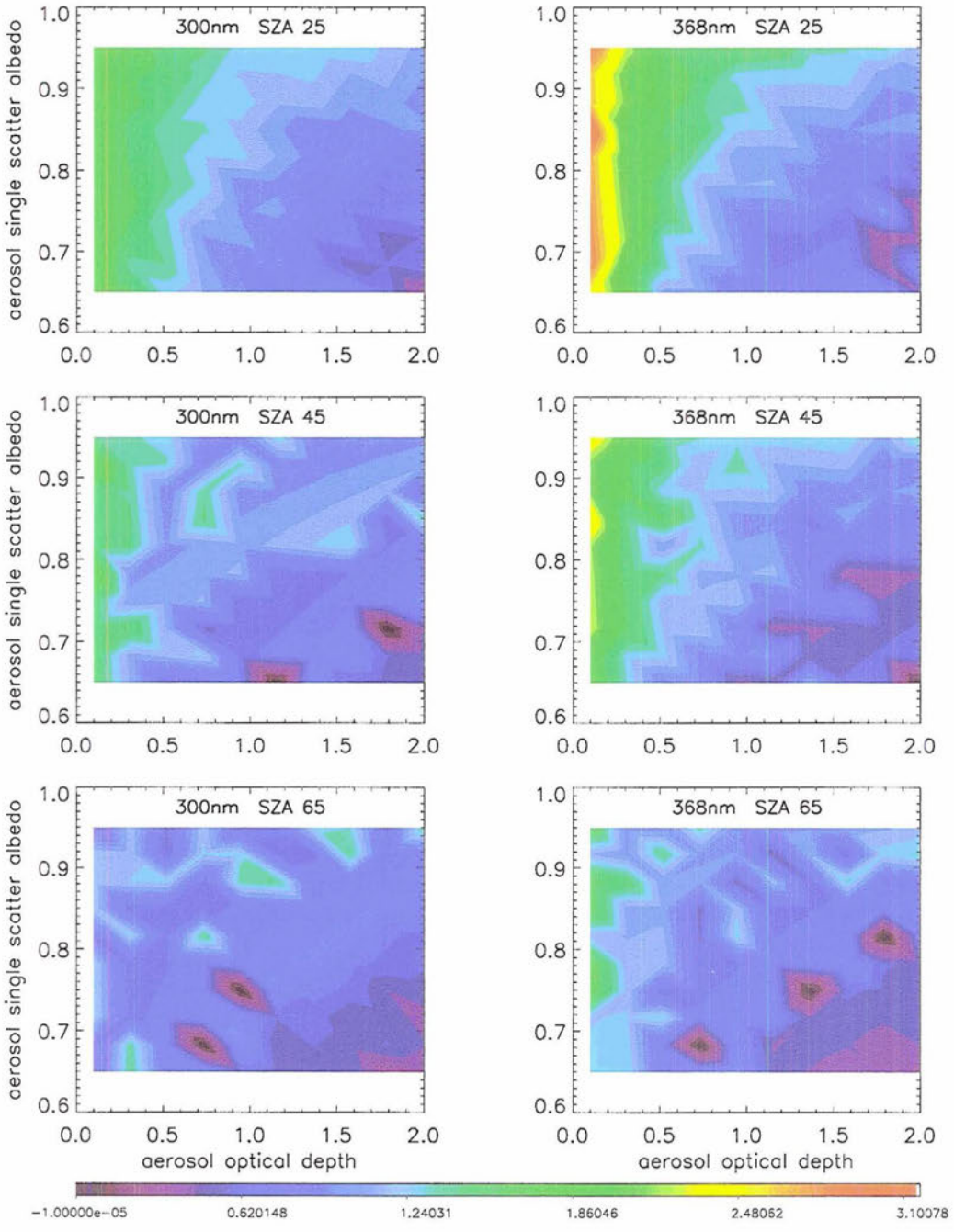

Figure 17: Percent uncertainty in modeled irradiances resulting in perturbations of ± 0.015 in the Doda and Green wavelength dependent desert sand surface albedos, α_s Doda and Green (1980), Doda and Green (1981). All plots are in AOD-SSA space with a common color scheme. Left column corresponds to 300-nm and right column to 368-nm. Top row corresponds to SZA 25°, middle row to 45° and bottom row to 65°.

5. Synthetic Testing of the Retrieval Algorithm

Prior to running the retrieval algorithm on real irradiance measurements, two important studies were undertaken to verify the usefulness and validity of the retrieval algorithm. First, synthetic retrievals were performed to determine the ability of the algorithm to find "truth" under known conditions. Second, the uniqueness of the solution space of the retrieval was investigated by analyzing the scalar cost function over the standard 100 grid point AOD-SSA domain space defined in the forward model testing. For both of these tests the forward model settings from the UVMRP site located at Panther Junction, Texas (29.130°N, 103.51°W, 670 meters elevation) were employed.

5a. *Synthetic Retrievals*

i. Defining the Atmospheric Scenarios To perform the synthetic retrievals, sets of values of aerosol single scattering albedo, SSA, and asymmetry factor, g, were selected to simulate varying scattering conditions of the atmosphere. As discussed in Section 2c, the SSA gives the relative amount of aerosol scattering to aerosol extinction, with SSA=1 indicating complete scattering (zero absorption) by the particle, and SSA=0 indicating no scattering (complete absorption) by the particle. The directionality of the scattering is quantified using g, with g=1 indicating complete forward scattering and g=0 indicating symmetrical scattering about the assumed spherical particle, as is the case for Rayleigh scattering. These two parameters are allowed to vary independently within the retrieval code. Each scattering scenario, defined by values of SSA and g, was subdivided into three atmospheric turbidity cases, defined by varying values of AOD such as to represent low, moderate and high turbidity conditions. Testing was also performed with the model set to several different local times to test the SZA dependence.

Total column ozone for all scattering scenarios and turbidity conditions was assigned

an *a priori* value of 350 Dobson Units (DU) with a standard deviation of 23 DU, based on the annual average and standard deviation of the daily values calculated by the UVMRP using the direct sun method Gao et al. (2001). Synthetic values of AOD were constructed to decrease with increasing wavelength, while synthetic values of SSA were constructed to increase with increasing wavelength, so as to match the wavelength dependences reported in the current literature, e.g., Wetzel et al. (2003), Petters et al. (2003), respectively. Using the synthetic values of the state parameters to represent truth, the forward model was run off-line to calculate synthetic values of the irradiances. These synthetic irradiances were then treated as real measurements, and used in the retrieval algorithm's $\mathbf{y}$ vector. The resulting estimated state parameters contained in the $\hat{\mathbf{x}}$ vector were compared to the "truth" values.

Two extreme atmospheric conditions tested will be discussed in detail. One was a "highly scattering" atmosphere, in which SSA and g were assigned relatively large values as given in Table 13. The second scenario was that of a "weakly scattering" atmosphere, in which SSA and g were assigned relatively low values, as given in Table 14. Several atmospheric cases intermediate to these two extremes were tested as well.

ii. The "highly scattering" Scenario Shown in Figure 18 are the retrieval results for the "highly scattering" scenario at local noon (SZA = 14°) at Panther Junction, Texas on May 22. The state parameters are plotted along the ordinate axis, with asymmetry factor at the bottom, followed by the 7 AOD in order of increasing wavelength, then the 7 SSA, and finally the TOC at the top of the ordinate. Note that the TOC has been normalized by 200 in order to fit on the abscissa scale of the plot, and that the normalized TOC are used in the retrieval algorithm so that all the input values of the state parameters in the $\mathbf{x}$ and $\mathbf{x_a}$ vectors are of the same order of magnitude to avoid mathematical complications. The values of "truth" are plotted as green triangles ($\triangle$), the *a priori* values as red "x" and the

Table 13: **"Truth" values of state parameters and associated *a priori* values used as retrieval inputs for synthetic testing of "highly scattering" atmospheric scenario.**

Truth	Thin Atmos.	Mod. Atmos	Thick Atmos	A priori	All scenarios
300nm AOD	0.18	0.78	1.48	300nm AOD	0.80
305nm AOD	0.16	0.76	1.46	305nm AOD	0.80
311nm AOD	0.14	0.74	1.44	311nm AOD	0.80
317nm AOD	0.12	0.72	1.42	317nm AOD	0.80
325nm AOD	0.10	0.70	1.40	325nm AOD	0.80
332nm AOD	0.08	0.68	1.38	332nm AOD	0.80
368nm AOD	0.06	0.66	1.36	368nm AOD	0.80
300nm SSA	0.85	0.85	0.85	300nm SSA	0.85
305nm SSA	0.86	0.86	0.86	305nm SSA	0.85
311nm SSA	0.87	0.87	0.87	311nm SSA	0.85
317nm SSA	0.88	0.88	0.88	317nm SSA	0.85
325nm SSA	0.89	0.89	0.89	325nm SSA	0.85
332nm SSA	0.90	0.90	0.90	332nm SSA	0.85
368nm SSA	0.91	0.91	0.91	368nm SSA	0.85
g	0.85	0.85	0.85	g	0.70
TOC	350	350	350	TOC	22.8
Norm. TOC	1.75	1.75	1.75	Norm. TOC	0.11

synthetically retrieved values as blue boxes. The 1σ and 3σ values for each parameter, as defined by the *a priori* and *a priori* error covariances, are plotted as red dotted and red dashed lines, respectively. The low turbidity atmosphere is shown in the top panel, the moderate turbidity in the middle panel and the high turbidity atmosphere in the bottom panel.

For the "highly scattering" scenario the retrieved values of AOD are very close to truth for all three turbidity conditions, except at the lowest wavelength channels. At 300- and 305-nm, where ozone absorption is strongest, the algorithm slightly overestimates the AOD values due to underestimation of the TOC. The condition is worse for the moderate turbidity case and best for the high turbidity case. The retrieval of SSA tends to

Table 14: **"Truth" values of state parameters and associated *a priori* values used as retrieval inputs for synthetic testing of "weakly scattering" atmospheric scenario.**

Truth	Thin Atmos.	Mod. Atmos	Thick Atmos	A priori	All scenarios
300nm AOD	0.18	0.78	1.48	300nm AOD	0.80
305nm AOD	0.16	0.76	1.46	305nm AOD	0.80
311nm AOD	0.14	0.74	1.44	311nm AOD	0.80
317nm AOD	0.12	0.72	1.42	317nm AOD	0.80
325nm AOD	0.10	0.70	1.40	325nm AOD	0.80
332nm AOD	0.08	0.68	1.38	332nm AOD	0.80
368nm AOD	0.06	0.66	1.36	368nm AOD	0.80
300nm SSA	0.75	0.75	0.75	300nm SSA	0.85
305nm SSA	0.76	0.76	0.76	305nm SSA	0.85
311nm SSA	0.77	0.77	0.77	311nm SSA	0.85
317nm SSA	0.78	0.78	0.78	317nm SSA	0.85
325nm SSA	0.79	0.79	0.79	325nm SSA	0.85
332nm SSA	0.80	0.80	0.80	332nm SSA	0.85
368nm SSA	0.81	0.81	0.81	368nm SSA	0.85
g	0.65	0.65	0.65	g	0.70
TOC	350	350	350	TOC	22.8
Norm. TOC	1.75	1.75	1.75	Norm. TOC	0.11

improve with increasing AOD, as there is more information in the diffuse beam with increasing turbidity, caused by the increased incidences of photon scattering. The retrieved value of asymmetry factor is much closer to truth for the moderate and high turbidity cases than for the low turbidity case since the quantification of the forward scattering is improved by the increase in the number of photon scattering events. In the moderate turbidity case g is slightly underestimated, while in the high turbidity case it is slightly overestimated.

Retrieval Errors Shown in Figure 19 are the input model-measurement percent uncertainties, used in the $\mathbf{S_y}$ matrix diagonal values, as well as the estimated error in the retrieved parameters (derived from $\hat{\mathbf{S}}$) for the highly scattering atmosphere with low tur-

bidity (top panel), moderate turbidity (middle panel) and high turbidity (bottom panel). The left ordinate and bottom abscissa show the input model-measurement errors for each of the 14 channels plotted as blue pluses ("+") with a solid interconnecting line. These are the values that were determined from the model sensitivity testing and instrument measurement analysis performed in Chapter 4, which were identical for all turbidity conditions. They have a slight wavelength dependence, decreasing with increasing wavelength, and range from about 4% to 6%. The uncertainties used for the diffuse beam are slightly higher than for the direct beam. The ordinate and top abscissa of the plots show the estimated percent uncertainty in each of the 16 retrieved parameters plotted as red asterisk ("$*$") with a dotted interconnecting line. There is a clear decrease in the percent error with increasing turbidity, especially for the 7 AOD, which decrease from about 25% - 40% at low turbidity to about 5% at moderate and high turbidities. The error in retrieved SSA is about 5% for low turbidity and decreases to about 2.5% at high turbidity. The error in TOC is always very close to zero, while the error in g decreases from about 20% for low turbidity to 12% for moderate and high turbidities.

A-matrix and χ^2 Values Shown in Figure 20 are the A-matrix values for each retrieval parameter plotted against the left ordinate as blue pluses with a solid interconnecting line. The χ^2 values for each retrieval are plotted against the right ordinate as green asterisk. The 80% and 95% confidence intervals for χ^2 are plotted as black dotted and red dashed lines, respectively. Note that each retrieval returns only one unique value of χ^2, but this single value has been plotted versus each parameter type in these plots to form a line. This is done solely as a visual aide in interpreting the results relative to the various significance levels.

The A-matrix values for AOD are between about 0.9 and 1.0 for all but the AOD_{300-nm}. There is not much change in the values with changing turbidity, indicating sufficient information in the measurements and good sensitivity of the forward model to AOD under

all conditions. The A-matrix values for all seven channel SSA are near to zero for the low turbidity case, indicating that little information is available from the measurements and forward model to determine these variables given this conditions. However, as turbidity increases, more information is available in the measurements due to the increased number of photon scattering events, leading to higher A-matrix values for all seven channel SSA. The A-matrix values for g increase with increasing turbidity for the same reasons. The A-matrix values for TOC are highest at low turbidity, decreasing from about 0.95 to about 0.70 from the low to high turbidity condition. This is due to the strong attenuation of the direct beam at the lower wavelengths with increasing turbidity; the same channels which are used to retrieve TOC.

The χ^2 values for both the low and high turbidity cases are above both the 80% and 95% confidence intervals, indicating that for these retrievals the model-measurement error budget is likely underestimated (Refer to χ^2 discussion in Section ii). The moderate turbidity atmosphere has a retrieved χ^2 value which falls in the middle of both the 80% and 95% confidence intervals, indicating strong significance of the estimated retrieval parameters in this case, and indicating that the input error budget is optimized for the moderate turbidity condition.

SZA Testing Testing for the "highly scattering" state was repeated for 9:30 a.m. local time (SZA = 46°). The results (not shown) indicate almost identical values of the retrieval parameters compared to the noon case, including a slightly better estimate of g for low and moderate turbidities. The A-matrix values showed slight improvement as well. Furthermore, retrieval error in AOD was slightly decreased. The testing performed for 8:00 a.m. local time (SZA = 66°) also indicated retrieved results (not shown) almost identical to those from the noon case, but with slight improvement in retrieved TOC and hence improvement in low wavelength AOD for the moderate turbidity atmosphere. A-matrix values for the retrieved SSA were significantly higher for the 8:00 a.m. case than

for the noon case. Retrieval errors were significantly reduced, especially in AOD, for the morning case versus the afternoon case. In general retrieval results improved with increasing SZA for the "highly scattering" atmospheric scenario.

iii. The "weakly scattering" Scenario Shown in Figure 21 are the retrieval results for the "weakly scattering" scenario. For all three turbidity conditions the retrieval of TOC and AOD are similar to the "highly scattering" case. However, the retrieved values of SSA are very close to the *a priori* values, and relatively far from truth, in all three conditions, indicating the inability of the retrieval to return accurate values of SSA given these atmospheric conditions. The retrieved value of asymmetry factor (0.57) for the "weakly scattering" atmosphere is very poor as it falls well below the "truth" value of 0.65, which was close to the chosen *a priori* value of 0.70. The quality of the retrieval does not change much with increasing turbidity as it did in the "highly scattering" scenario.

When the synthetic retrieval was performed at 9:30 a.m. local time (SZA=44°) under the "weakly scattering" condition the retrieved parameters (not shown) had values almost identical to those from the noon scan. The A-matrix values were very similar as well. The retrieval error was somewhat reduced, most notably for the 7 AOD. For the case performed at 8:00 a.m. local time (SZA=67°) the retrieved values (not shown) of AOD remained similar to those from the noon case. However there was significant improvement in the retrieved SSA values relative to "truth". Also of note was an almost perfect retrieval of g for the low turbidity case in the morning, whereas retrieved g for moderate and high turbidities was still different from "truth" by about the same amount as it was in the noon case. The A-matrix values were similar for SSA compared to the noon case, while some improvement was made in the AOD and TOC A-matrix values. However, the A-matrix values for g experience a degradation relative to the noon case. Some improvement in the AOD error was seen, especially for the low turbidity case.

In summary, the retrieval algorithm has low skill in estimating SSA and g under the "weakly scattering" atmospheric condition. This is due to the combination of insufficient information contained in the diffuse component of radiation and the low sensitivity of the forward model under these conditions. The direct-to-diffuse ratio (DDR) of the measured irradiances can be used to parameterize this condition.

iv. The "minimum threshold" Scenario With the two extreme scattering conditions thus defined, several intermediate atmospheric scattering scenarios were analyzed to deduce the atmospheric conditions which serve as limits for a "successful" retrieval. The results from this testing can be summarized fairly succinctly as follows. When the forward scattering is decreased ($g = 0.65$) but scattering efficiency remains high (SSA $\simeq 0.85 \rightarrow 0.91$ from 300- to 368-nm), the retrieved values of SSA improve with increasing turbidity, while the retrieved values of g lie between truth and *a priori*. In contrast, if the forward scattering remains large ($g = 0.85$) but the scattering efficiency decreases (SSA $\simeq 0.75 \rightarrow 0.81$ from 300- to 368-nm) then the retrieved values of g are usually in the opposite direction from *a priori* to truth, while the retrieval of SSA is generally reliant on the *a priori* values, even for the high turbidity condition.

Based on this analysis it is clear that the retrieval is reliant on relatively highly scattering conditions in order to provide sufficient information in the diffuse beam to determine SSA and g. Several variations of a "moderately scattering" atmosphere were thus tested by systematically altering the synthetic values of SSA and g to determine the lower boundary, or "minimum threshold", of these parameters required for a successful retrieval. If SSA $> 0.83 \rightarrow 0.89$ from 300- to 368-nm, and $g > 0.65$, then the retrieval of all parameters was reasonably accurate. In general, all retrieval values are improved (less error, higher A-matrix values) as turbidity conditions increase and as SZA increases out to $65°$.

Using the "minimum threshold" atmosphere a lower boundary limit on retrieved AOD was determined to be AOD $\simeq 0.1 \rightarrow 0.07$ from 300- to 368-nm. This limit was based on the "truth" values which returned an estimated retrieval error of close to 50% in the retrieved AOD values, i.e., for smaller values of AOD the estimated retrieval error was larger than 50%. The aerosol study of Wenny *et al.* reported a range of 368-nm AOD from 0.030 to 1.2 at Black Rock Mountain in North Carolina Wenny et al. (2001). The ranges reported in central Alaska by Wetzel *et al.* for 368-nm AOD were 0.15 to 0.25 for a spring marine air mass, 0.11 to 0.14 for a spring Asian air mass, and 0.05 to 0.06 for both a summer and spring Arctic air mass. Comparison of the lower OE AOD boundary ($\simeq 0.1 \rightarrow 0.07$) to previous research indicates that the retrieval algorithm may produce very high errors on the estimated parameters at some of the UVMRP sites with pristine environments, e.g., the site in Alaska.

The boundary condition values of AOD, SSA and g given here can be used to provide a post-algorithm screening of the retrieval results, as will be discussed in Sec 7b.

5b. *Uniqueness of the Solution Space*

i. Description of the Testing A simplified method for showing that the retrieval has a unique solution within some reasonable domain of physical parameter space is described. Uniqueness here is defined by the cost function (Equation 55) having a single minimum value or region in domain space towards which the retrieval will converge. This testing is simplified in the sense that only the AOD and SSA physical parameters have been tested. Testing of TOC and asymmetry factor have not been performed, i.e., these two values were held fixed. In brief, the solution space testing is performed by first producing maps of irradiance space via iteration of the forward model. The scalar cost function is then calculated over the domain space using selected values of AOD and SSA to serve as *a priori*, while another set of AOD and SSA values are chosen to represent "truth". This

produces maps of the scalar cost function value over the AOD-SSA domain space, which can be analyzed as described below.

Specifically, the solution space testing was performed as follows. First a set of *a priori* values and synthetic values of AOD and SSA were selected from the domain space to fill the $\mathbf{x_a}$ and $\mathbf{x}$ vectors, respectively. Two simulations were performed; one set consisted of low *a priori* (AOD=0.4, SSA=0.85) with a turbid atmosphere (AOD=1.2 , SSA=0.817), while the second set consisted of high *a priori* (AOD=1.4, SSA=0.85) with a low turbidity atmosphere (AOD=0.311, SSA=0.817). Modeled irradiances were then calculated over the standard 100 point AOD-SSA domain at 25°, 45° and 65° SZA using constant values of TOC and g with all other parameters (e.g., latitude, longitude) set to the values corresponding to the Panther Junction, Texas test site. The direct and diffuse irradiances from the precalculated model run corresponding to the selected domain points were then assigned to fill the $\mathbf{y}$ vector, which remained fixed. The scalar cost function (refer to Eqn. 55) at each point in domain space (a, b) was then calculated with the $\mathbf{F(x)}$ vector containing the associated precalculated modeled irradiances, i.e., $\mathbf{F(x_{(a,b)})}$, which vary at each point in the domain.

The described procedure produces a map of cost function values over the AOD-SSA domain, providing a snap-shot of the retrieval solution on the first iteration of the algorithm. Again, since TOC and g were not allowed to vary within the retrieval, it is not exactly clear that the complete solution space will be this well behaved. Contour plots of the cost function values provide visualization of the retrieval solution as a surface in space, providing insight about the condition of the retrieval. The mechanical analog is that of a 3-D surface in physical space on which a marble is placed initially at the *a priori* point and is allowed to roll freely towards an equilibrium point on the surface (the solution) governed by the physics of the problem, namely gravity and friction. In the case of the retrieval algorithm the mechanical laws are replaced by the physics of the forward

model. The quantity of local minima indicate the number of distinct possible solution sets of the retrieval, i.e., uni-modal or multi-modal. The magnitudes of the local maxima and minima indicate the resolution of the retrieval. The relative contribution to the solution from the measurement term and the *a priori* term can be evaluated, in analogy with the A-matrix values, since the total solution is a sum of these two components. The magnitude of the contour gradient can be interpreted as a measure of how quickly the retrieval should converge, i.e., the number of iterations required for convergence.

ii. Results of the Testing Solution spaces were calculated separately for each of the 7 wavelengths so that the relative contributions from each could be analyzed. Calculations were also performed at 25°, 45° and 65° to determine the SZA dependence. Figure 22 shows the solution space maps for SZA 25°. The figure is divided into 4 quadrants containing three panels each. The left side of the figure shows results at 300-nm while the right side corresponds to 368-nm. The top half of the figure shows results for the turbid atmosphere (red asterisk) with low *a priori* (white box) while the bottom half of the figure corresponds to a low turbidity atmosphere (red asterisk) with high *a priori* (white box). In each of the quadrants the 3 stacked panels correspond to the total solution space (top), the contribution from the measurement term (middle) and the contribution from the *a priori* term (lower). Recall that the *a priori* values of the state parameters are used as a first guess in the iterative equation such that the retrieval can be interpreted as beginning at the *a priori* point (shown as white boxes in the figure) and moving toward the solution (plotted as red asterisk in the figure). The contours are plotted in AOD-SSA space using a logarithmic color scale to highlight the gradient.

From this figure it can be observed that for both thick and thin atmospheres at 300- and 368-nm the total solution space has a smooth gradient from the *a priori* to the synthetic value with respect to AOD and SSA. This indicates that the retrieval algorithm will

always move towards the solution when minimizing the cost function and that only one solution exists, i.e., the retrieval solution is uni-modal. For each particular simulation the contribution from the measurements to the total solution is substantially larger than that from the *a priori* as is evident from the magnitude of the scales. Comparing the results from 300-nm to those from 368-nm is can be seen that the contribution to the solution is greatest at longer wavelengths. This information is consistent with the model sensitivity testing explored thoroughly in Section 4b. That is, the greatest amount of information is contained in the longer wavelengths for retrieving AOD and SSA.

Figures 23 and 24 show the results for solution space testing at 45° and 65°, respectively. For both wavelength and turbidity scenarios the gradient of the scalar cost function increases with increasing SZA, as evidenced by the larger magnitude of the scale. This indicates better resolution of the retrieval for larger SZA, and possibly faster convergence of the algorithm. The increase in gradient is more pronounced for the high turbidity case than for the low case as the model sensitivity increases more due to increased photon scattering. Note that the gradient with respect to SSA for the low turbidity case is reduced with increasing SZA, an indicator that the attenuation of the beam is too large. The retrieval may therefore have problems successfully retrieving SSA at low turbidity and high SZA, as was shown by the synthetic retrieval testing. Overall however, these solution space maps indicate the well-behaved nature of the retrieval problem concerning AOD and SSA, and the possibility of obtaining estimated values of the state parameters that are reasonably accurate.

It is feasible to calculate a sort of "movie" of the retrieval algorithm as it converges on a solution by calculating solution space maps at each iteration and viewing the maps sequentially in time. The resolution of the retrieval, analogous to the information content (IC), could perhaps be studied by analyzing the ratio of the area below some minimum threshold on the first iteration to the area of the minimum on the final iteration. Further-

more, it would be ideal to incorporate TOC and g as variables in this testing to determine if the retrieval solution remains well behaved and/or unique. Incorporation of these two parameters, however, means that simple 2-D maps could not be used for visualizing the results. A more clever interpretation would be required, or many more maps of the type described would be necessary to glean the desired information.

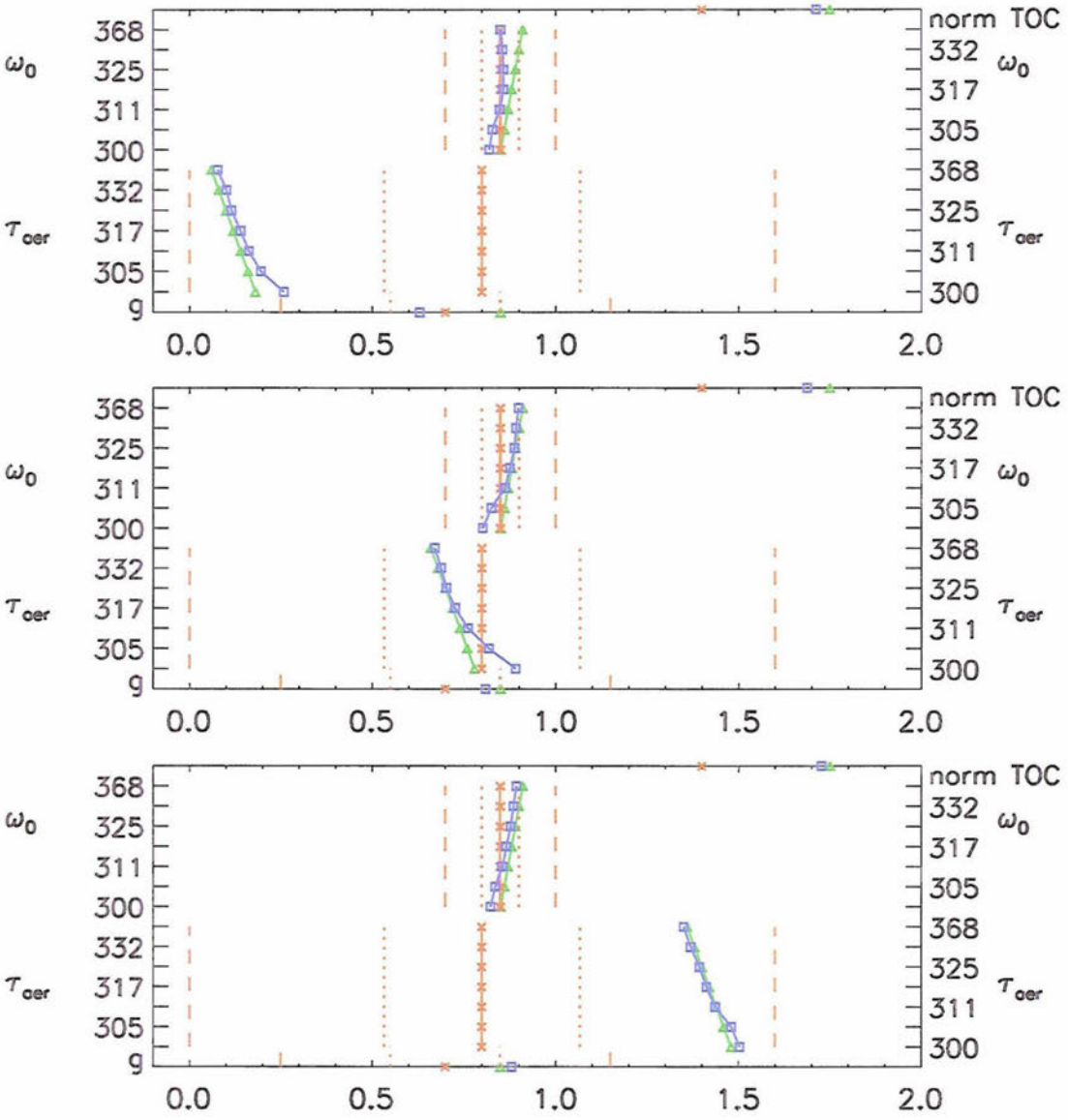

Figure 18: Synthetically retrieved parameters for a highly scattering atmosphere with low turbidity (top panel), moderate turbidity (middle panel) and high turbidity (bottom panel) at local noon (SZA=14.4°) at Panther Junction, Texas on May 22. A priori plotted as red "x", "truth" values plotted as green triangles and retrieved values plotted as blue squares. 1 and 3 σ deviations from the *a priori* plotted as red dotted and dashed lines, respectively. Ordinate arranged such that asymmetry factor is the lowest plot element followed by 7 AOD and then 7 SSA in order of increasing wavelength, and normalized TOC (TOC/200) as uppermost plot element. For clarity, every other element on each side of the ordinate is labeled.

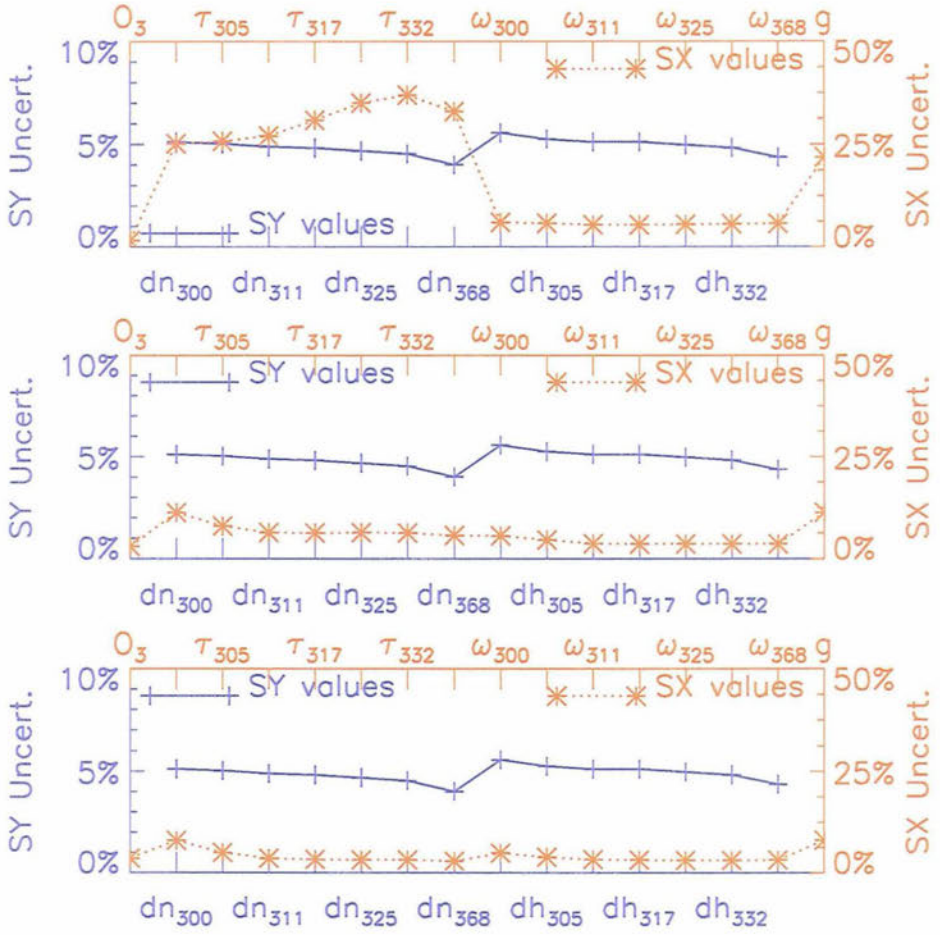

Figure 19: Input model-measurement errors and estimated retrieval errors in synthetically retrieved parameters for a highly scattering atmosphere with low turbidity (top panel), moderate turbidity (middle panel) and high turbidity (bottom panel) at local noon (SZA=14.4°) at Panther Junction, Texas for May 22. The left ordinate and bottom abscissa show the input model-measurement errors for each of the 14 channels plotted as blue pluses with solid interconnecting line. The ordinate and top abscissa show the estimated percent uncertainty in each of the 16 retrieved parameters plotted as red asterisk with dotted interconnecting line.

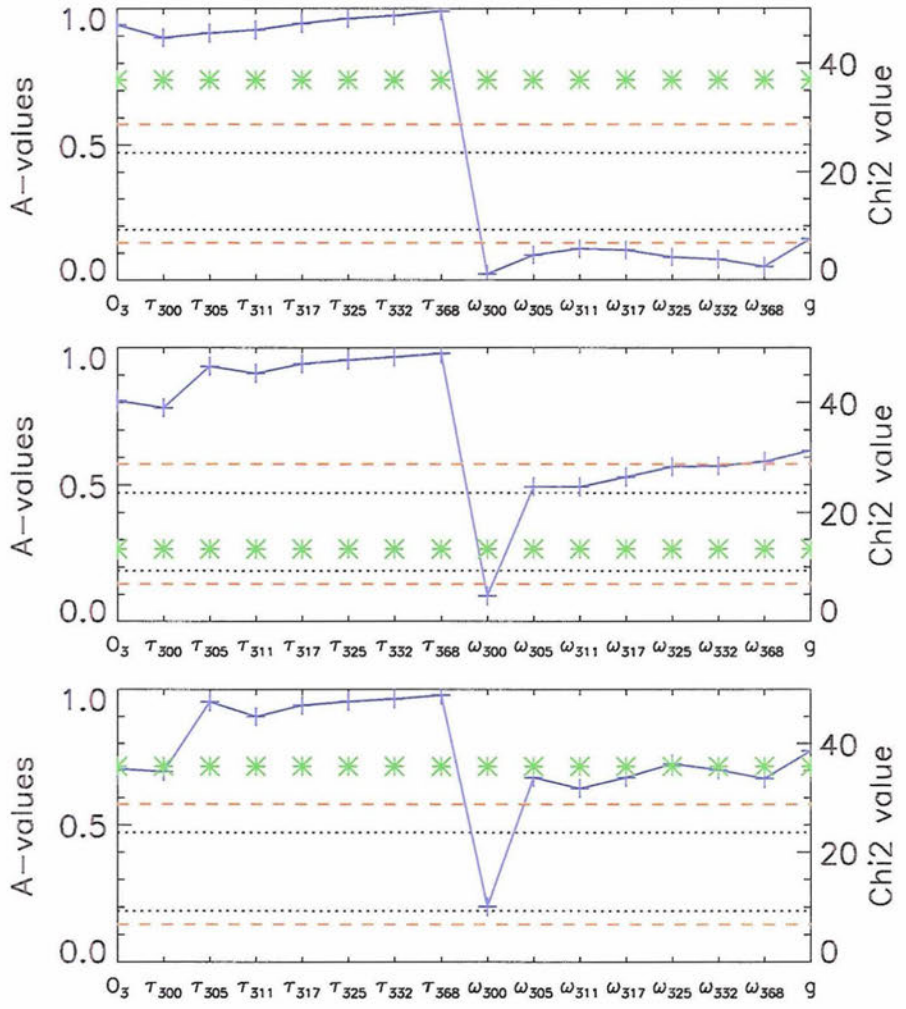

Figure 20: A-matrix and χ^2 values for synthetically retrieved parameters for a highly scattering atmosphere with low turbidity (top panel), moderate turbidity (middle panel) and high turbidity (bottom panel) at local noon (SZA=14.4°) at Panther Junction, Texas for May 22. A-matrix values plotted against the left ordinate as blue pluses and values of χ^2 are plotted as green asterisk against the right ordinate. The 80% and 95% confidence intervals are plotted as black dotted and red dashed lines, respectively, against the right ordinate.

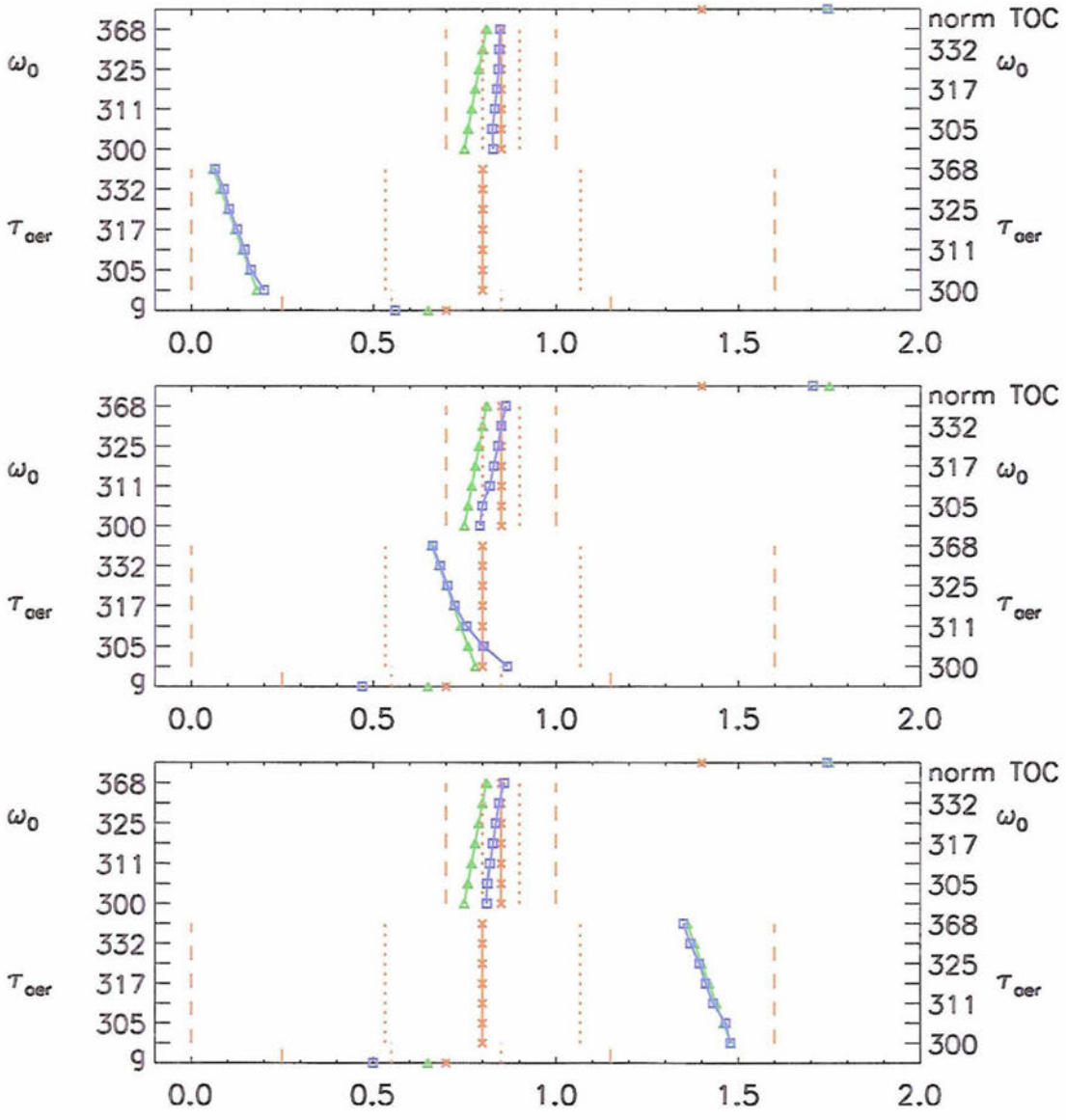

Figure 21: Same as Fig. 18, but for the "weakly scattering" atmospheric scenario.

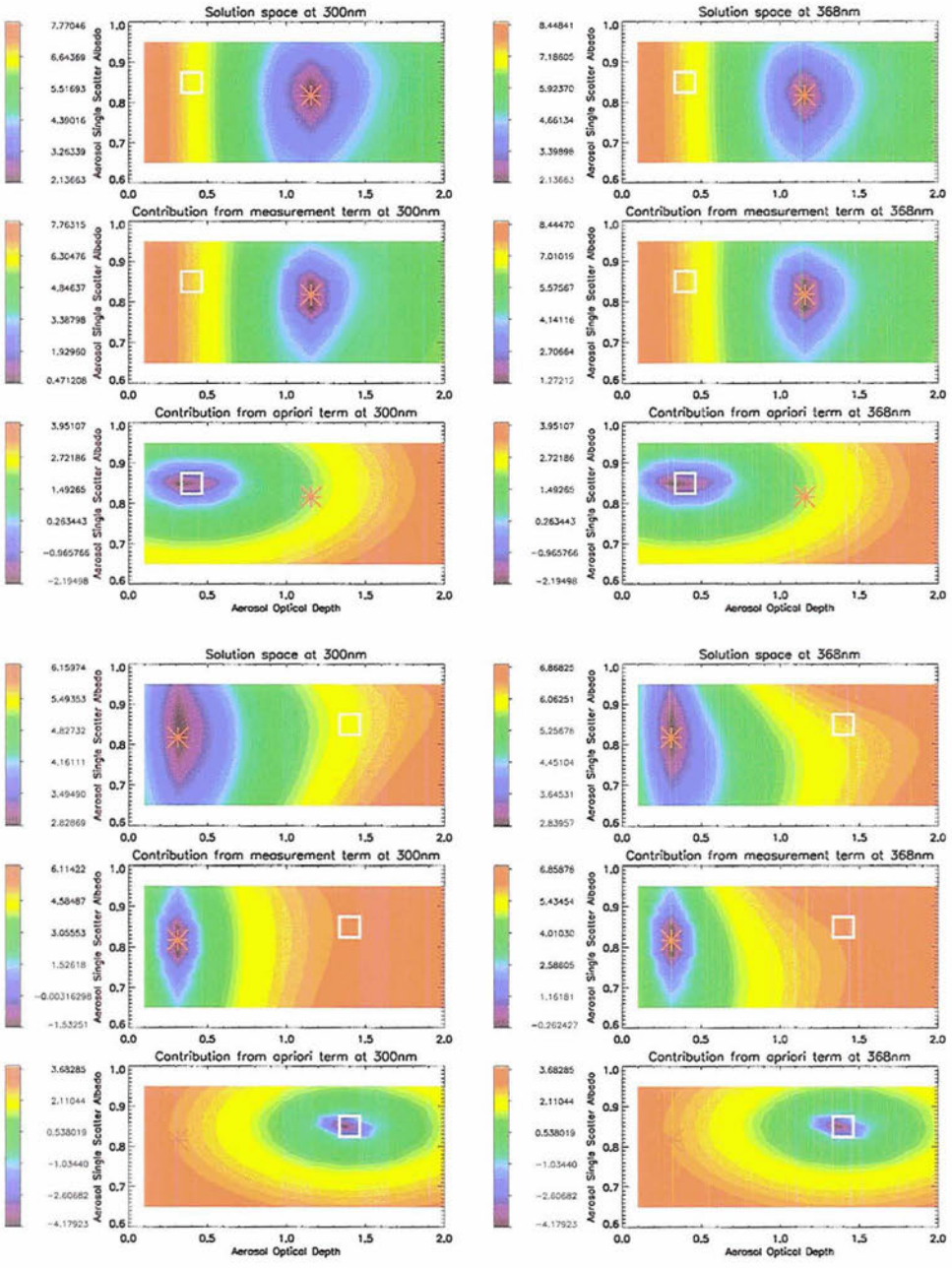

Figure 22: Contours of the scalar cost function representing the retrieval solution space in the AOD-SSA domain at SZA 25° for 300-nm (left panels) and 368-nm (right panels). Top six panels each represent a moderate turbidity condition with a low *a priori* while the bottom six panels represent a low turbidity condition with high *a priori*. Each quadrant consists of three vertically stacked plots showing, from top to bottom, the total solution space, the contribution to the solution from the measurements and the contribution to the solution from the *a priori* term of the cost function, respectively. The white boxes represent the *a priori* values of AOD and SSA, while the red asterisk represent the "truth" or solution values. AOD is labeled on the abscissa and SSA is labeled on the ordinate in all plots. The scale is represented in logarithmic space to highlight the features of the contours.

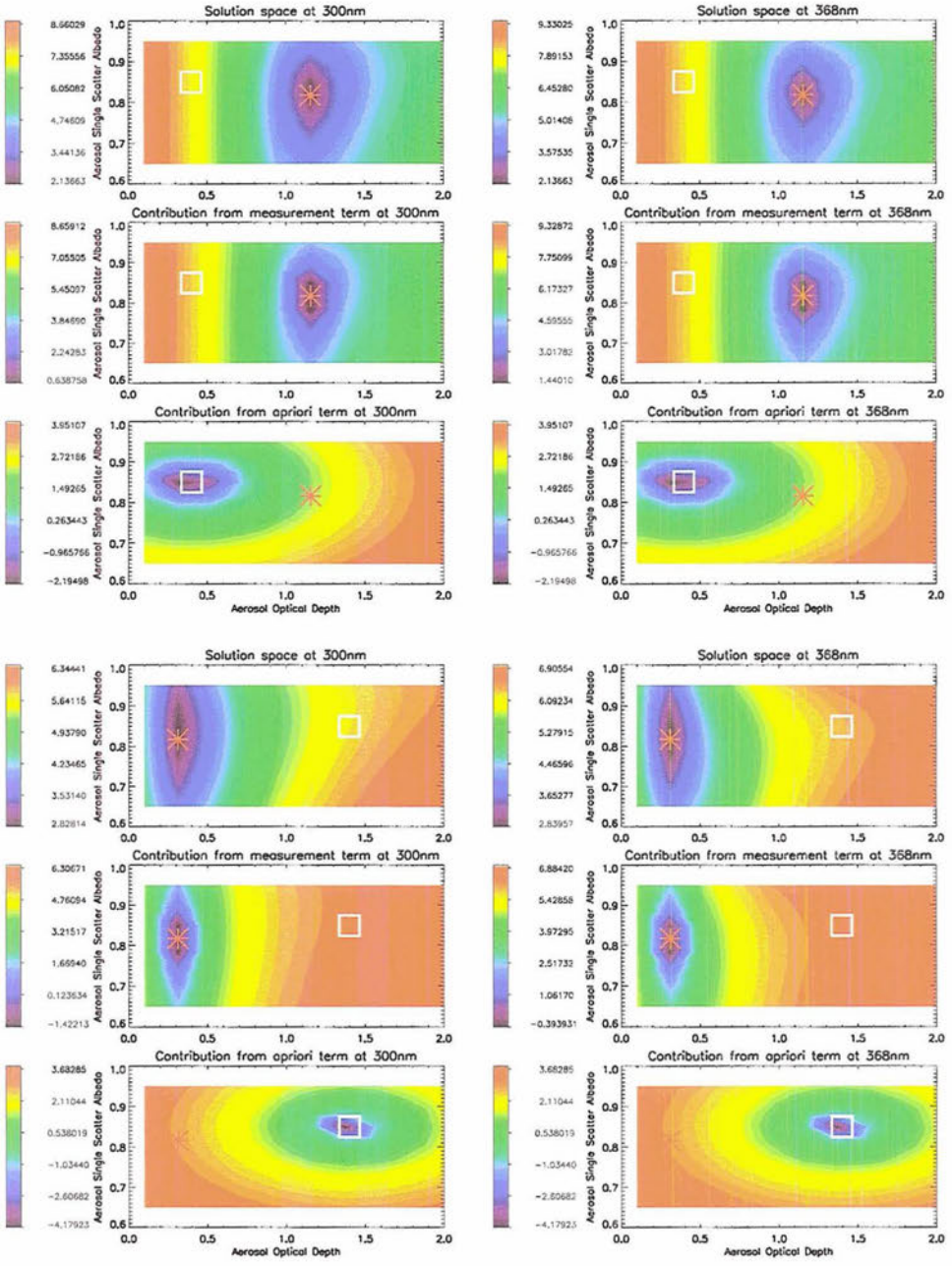

Figure 23: Same as Figure 22 but for SZA 45°

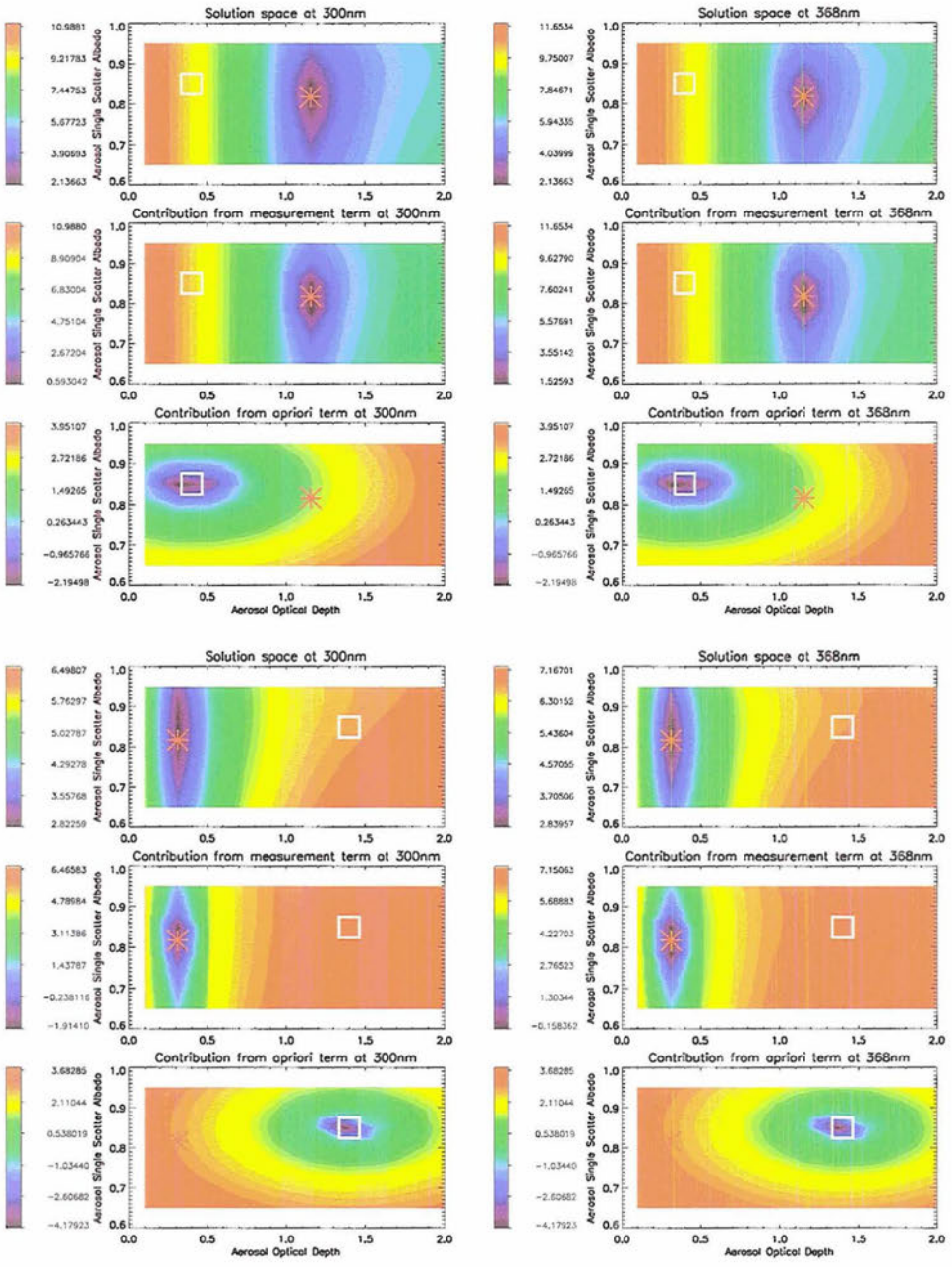

Figure 24: Same as Figure 22 but for SZA 65°.

6. Retrieval Analysis

6a. *Setting up the Retrieval at Panther Junction, Texas*

Initial testing of the modified retrieval was performed using data from the UVMRP site at Panther Junction, Texas in Big Bend National Park, located in the southwestern region of the state (29.130N, 103.51W, 670 meters elevation). This remote park is part of the Chihuahan Desert, and in spite of its isolation from major industrial or urban centers, has been ranked among those with the poorest visibility in the U.S. park system Hand et al. (2002). May 22, 2003 was selected as the initial test case, as it was verified to be a mostly cloud free day with the exception of the late afternoon. This is indicated in Figure 25 which shows a plot of the Langley derived values of AOD_{368-nm}, as calculated by the UVMRP, before and after the cloud screening was applied.

To adapt the retrieval code and forward model to the Panther Junction site the appropriate latitude, longitude, time zone and altitude of the site were set in the input text file. The spectral responsivity file corresponding to the instrument of interest (#393) was loaded into the TUV model and the analytical function for the Doda and Green desert sand albedo was programmed into the appropriate TUV subroutine Doda and Green (1981). The values of total column NO_2 and SO_2 were set equal to zero.

The explicitly stated inputs which are necessary to the retrieval are the terms contained in Eqn 62. They are; 1.) the measurement vector $\mathbf{y}$, 2.) the *a priori* state vector $\mathbf{x_a}$, 3.) the model-measurement error covariance matrix $\mathbf{S_y}$ and 4.) the *a priori* error covariance matrix $\mathbf{S_a}$. These terms are now described for the particular test case.

i. Measurement vector The measurement vector has not been altered from that as initially used by Goering *et al.* Goering et al. (2005). It consists of the 14 UV-MFRSR direct and diffuse irradiance measurements, at 7 wavelength channels in the UV spectral

range;

$$\mathbf{y} = \begin{bmatrix} dir_{300-nm} \\ dir_{305-nm} \\ dir_{311-nm} \\ dir_{317-nm} \\ dir_{325-nm} \\ dir_{332-nm} \\ dir_{368-nm} \\ dif_{300-nm} \\ dif_{305-nm} \\ dif_{311-nm} \\ dif_{317-nm} \\ dif_{325-nm} \\ dif_{332-nm} \\ dif_{368-nm} \end{bmatrix}$$

ii. Measurement-model error covariance matrix The $\mathbf{S_y}$ model-measurement error covariance matrix is a 14x14 matrix with the diagonal values set equal to the estimated variance of each of the measured irradiances, i.e., the square of the error weighted irradiance measurements using the uncertainties given in Table 12;

$$\mathbf{S_y}(Diagonals) = \begin{bmatrix} (5.11\% * dir_{300nm})^2 \\ (5.03\% * dir_{305nm})^2 \\ (4.89\% * dir_{311nm})^2 \\ (4.82\% * dir_{317nm})^2 \\ (4.68\% * dir_{325nm})^2 \\ (4.54\% * dir_{332nm})^2 \\ (4.01\% * dir_{368nm})^2 \\ (5.56\% * dif_{300nm})^2 \\ (5.25\% * dif_{305nm})^2 \\ (5.11\% * dif_{311nm})^2 \\ (5.11\% * dif_{317nm})^2 \\ (4.97\% * dif_{325nm})^2 \\ (4.83\% * dif_{332nm})^2 \\ (4.37\% * dif_{368nm})^2 \end{bmatrix}$$

The off-diagonals, which represent cross-correlations between the errors in the channels, as might occur due to signal contamination by light leakage for example, were all set equal to zero, as no method is currently known for determining these values.

iii. ***a priori*** **vector** The values of AOD, SSA and g used in the *a priori* vector, $\mathbf{x_a}$, were taken from the work of Goering *et al.* Goering et al. (2005). These values are the mean values of the range of the parameters as determined from various measurement and modeling studies, e.g., Wenny et al. (1998), Petters et al. (2003). The mean annual TOC, calculated by the UVMRP using the direct sun method Gao et al. (2001), was used for the *a priori* value of TOC. The specific form of the *a priori* vector used in this study was;

$$\mathbf{x_a} = \begin{bmatrix} TOC = \overline{TOC} \\ AOD_{300-nm} = 0.80 \\ AOD_{305-nm} = 0.80 \\ AOD_{311-nm} = 0.80 \\ AOD_{317-nm} = 0.80 \\ AOD_{325-nm} = 0.80 \\ AOD_{332-nm} = 0.80 \\ AOD_{368-nm} = 0.80 \\ SSA_{300-nm} = 0.85 \\ SSA_{305-nm} = 0.85 \\ SSA_{311-nm} = 0.85 \\ SSA_{317-nm} = 0.85 \\ SSA_{325-nm} = 0.85 \\ SSA_{332-nm} = 0.85 \\ SSA_{368-nm} = 0.85 \\ g = 0.70 \end{bmatrix}$$

iv. *a priori* error covariance matrix The $\mathbf{S_a}$ matrix is a 16x16 matrix with diagonal elements equal to the variances of each retrieval parameter contained in $\mathbf{x_a}$. These values were taken from Goering *et al.* Goering et al. (2005), and were originally determined from the estimated range of variability in the state parameters allowed in nature (1σ deviations) as reported from current literature, e.g., Wenny et al. (1998), Petters et al. (2003), Wenny et al. (2001), Wetzel et al. (2003). The values used were; $1\sigma_{AOD} = 0.2667$, $1\sigma_{SSA} = 0.05$, $1\sigma_g = 0.1$. The standard deviation of the annual daily averaged TOC for the Panther Junction site was used to calculate the variance in *a priori* TOC.

The $\mathbf{S_a}$ matrix contained the following values in the diagonal elements for all retrievals;

$$\mathbf{S_a}(diagonals) = \begin{bmatrix} \sigma_{TOC} = (\sigma_{\overline{TOC}})^2 \\ \sigma_{AOD_{300-nm}} = (0.267)^2 \\ \sigma_{AOD_{305-nm}} = (0.267)^2 \\ \sigma_{AOD_{311-nm}} = (0.267)^2 \\ \sigma_{AOD_{317-nm}} = (0.267)^2 \\ \sigma_{AOD_{325-nm}} = (0.267)^2 \\ \sigma_{AOD_{332-nm}} = (0.267)^2 \\ \sigma_{AOD_{368-nm}} = (0.267)^2 \\ \sigma_{SSA_{300-nm}} = (0.05)^2 \\ \sigma_{SSA_{305-nm}} = (0.05)^2 \\ \sigma_{SSA_{311-nm}} = (0.05)^2 \\ \sigma_{SSA_{317-nm}} = (0.05)^2 \\ \sigma_{SSA_{325-nm}} = (0.05)^2 \\ \sigma_{SSA_{332-nm}} = (0.05)^2 \\ \sigma_{SSA_{368-nm}} = (0.05)^2 \\ \sigma_g = (0.10)^2 \end{bmatrix}$$

Note that the particular choices of *a priori* and *a priori* standard deviation for AOD gives this parameter a 3σ range from 0.002 to 1.6, while the 3σ range for SSA is 0.7 to 1.0. For asymmetry factor the 3σ range is 0.4 to 1.0. All of these ranges are physically plausible and not too restrictive.

The off-diagonal elements of the $\mathbf{S_a}$ matrix represent the error covariances between each parameter. The error covariances between like parameter types only, i.e. no "cross-talk" amongst AOD, SSA, TOC and g, were constrained using an off-diagonal exponen-

tial decay algorithm given by,

$$\mathbf{S_{a(k,j)}} = \sqrt{(\mathbf{S_{a(k,k)}} * \mathbf{S_{a(j,j)}}) * exp[-(\lambda_{(k-1)} - \lambda_{(j-1)})^2/(scale)^2]}, \qquad (88)$$

where "k" and "j" designate the row and columns of the matrix and *scale* represents a scaling factor dependent on the strength of the correlation between adjacent wavelengths or parameters. The correlation between adjacent wavelengths is proportional to the negative exponential of the inverse square of *scale*. Therefore as *scale* is increased from zero (equivalent to zero correlation between adjacent elements) the correlation between adjacent elements becomes stronger. This off-diagonal correlation among like-parameter types further constrains the retrieval algorithm with regard to the various degrees of freedom as discussed in Section ii. This is a form of additional information into the retrieval, equivalent to adding independent measurements, which partially off-sets the decrease in conditioning of the retrieval problem caused by the addition of asymmetry factor into the retrieval state vector.

No intuitive physical method is known for determining the strength of the correlation in error among adjacent wavelengths or parameters. The retrieval was performed on the test scan (noon 22 May, 2003) with varying values of *scale* and the results were analyzed via the retrieval diagnostics, which were discussed in Section ii. Figure 26 shows plots of the A-matrix and χ^2 values for various cases. Other valuable diagnostics, including dof_a, dof_s, dof_m, dof_R, Shannon information content, and information related to the convergence of the retrieval are listed below for each case in the corresponding color. When *scale* is increased from 0.0 to 4.0, there is almost no change in the A-matrix values and the χ^2 value decreases slightly, becoming just a fraction more significant at the 80% confidence interval. For *scale* equal to 8.0 the correlations in adjacent elements increase, causing a slight decrease in the A-matrix values (less emphasis on measurements) but an improvement in the statistical significance of the result to the middle of the significance

interval. For *scale* equal to 15.0 the correlations among adjacent elements become too strong, forcing the algorithm to rely much more heavily on the *a priori* than the measurements (decrease in A-matrix values), while the χ^2 value remains comfortably within the 80% significance interval.

The value of dof_a decreases with increasing *scale* as a consequence of increased correlations, indicating that the number of independent parameters being retrieved decreases from the full 16 when *scale* equals to 0 to 11.7 when *scale* equals to 15.0. The value of dof_s also decreases with increasing *scale* due to the correlations in $\mathbf{K}$. As *scale* increases past about 8.0 the value of dof_s drops more rapidly than that of dof_a, causing a decrease in the value of dof_R. The ideal dof_R is 1 (1 independent measurement per independent retrieval parameter, yielding a well-posed problem), a number which is most closely achieved for *scale* equal to 8.0.

The Shannon information content of the retrieval is reduced as *scale* increases. This is due to the reduction in the *a priori* state space (recall the large ellipse in Figure 9) caused by the induced correlations. A change in H can be interpreted as a change in the number of distinct states which can be resolved by the retrieval. Increasing *scale* from 0 to 8 yields a change in the number of resolved states of $2^{23.19} - 2^{20.22} = 8.34\text{x}10^6$, which yields about 87% less distinct states. When *scale* is equal to 15, H is reduced even further, yielding only about $8.4\text{x}10^5$ resolvable states; a reduction of about 14 times the original number of resolvable states.

Based on the diagnostic analysis of the A-matrix values, the χ^2, the various values of dof and the information content, a value of *scale* equal to 8.0 was deemed the most ideal and was used in all subsequent retrievals.

6b. *Retrieving 16 Parameters from 14 Measurements*

The optimal estimation retrieval algorithm based on the Bayesian technique estimates values of the state parameters by combining the information contained in the forward model and measurements with previous knowledge of the physics of the problem. During iteration towards a solution, the algorithm can be thought of as moving from the *a priori* towards the solution. Each solution for each retrieval parameter is a linear combination of the *a priori* value and the information contained in the model-measurements, a parameter which is captured in the A-matrix values. A consequence of having an *a priori* value of each state parameter means that as many variables as desired can be set into the retrieval vector, regardless of the amount of model-measurement information available. However, this statement is misleading in the sense that the model-measurements contain only limited information and the introduction of more variables into the retrieval vector will lessen the accuracy of the estimates, assuming that there is even any information available regarding a particular parameter. For example, in the aerosol retrieval described in this research, it is conceivable to add the surface albedo as yet another state parameter to be estimated, bringing the total number of retrieval parameters to 17, using the same 14 measurements. In this case the TUV forward model and measurements do contain information concerning this variable. However, introduction of this parameter would detract from the information available to estimate the other parameters, yielding less accurate results overall, i.e., increased error and lower A-matrix values.

As discussed in the previous section as well as in Section ii, the various degrees of freedom are used to interpret the amount of information available in the model and measurements as well as the number of independent parameters which need to be retrieved. An ideal retrieval has exactly the same amount of available information as the number of independent retrieval parameters, i.e., $dof_R = dof_s/dof_a = 1$. As will be discussed in the upcoming sections, the retrieval described in this work has values of $dof_R < 1$, with

values increasing with turbidity. So, during times of high turbidity it should be expected to see an increase in the A-matrix values, meaning that the state parameters are more determined by the measurements. Likewise, during times of low turbidity, it should be expected that the A-matrix values will decrease, i.e., the retrieval will rely more heavily on the *a priori* values to estimate the state parameters. This will be shown to be true for this retrieval in the analysis of the results.

6c. *Output Analysis*

Once all of the OE algorithm inputs were selected, the full irradiance data set for Panther Junction for the month of May 2003 was cloud screened using the algorithm of Smirnov *et al.* Smirnov et al. (2000). The original irradiance file consisted of 7012 scans measured by the UV-MFRSR at 3 minute time intervals. After the cloud screening was applied, 4015 scans remained. The OE retrieval was then performed over all cloud screened scans for the month of May, 2003, providing 3931 successful convergences (97.9% success rate) in approximately 43 hours on a 3 GHz processor PC. The results were then χ^2 filtered at the 95% confidence interval, leaving 2070 scans for analysis.

i. Monthly retrieval time series The monthly time series of AOD_{368-nm}, SSA_{368-nm}, TOC, asymmetry factor (g) and calculated Ångstrom exponent (α) are shown in Figure 27. Note that only the results for AOD and SSA at one channel (368-nm) are shown for brevity and clarity. The wavelength dependence of AOD will be discussed in terms of the Ångstrom exponent in Section iv, and a detailed analysis of the wavelength dependence of the SSA values will be given in Section v.

AOD_{368-nm} The top panel in the figure shows that AOD_{368-nm} varies between 0.09 and 1.4 with mean 0.36. The variation in monthly AOD is similar to that found by Kylling

et al. over a 22 day period in a field campaign conducted in two locations in Greece Kylling et al. (1998), indicating that the retrieval results are physically reasonable. The envelope of the daily fluctuations are indicative of local changes in air mass as might be due to passing of synoptic scale fronts or perhaps localized dust storms. A strong change in regime is especially pronounced from May 15 to 17. Note that the irradiance data from May 16 was cloud screened due to high variability in the Langley derived AOD values, indicative of cloud cover during this time. It would be ideal to quantify source inventory data of SO_x and NO_x emissions for this time period and region as is discussed by Petters *et al.* in their study at Black Mountain in North Carolina Petters et al. (2003). This information would allow for the demarcation of air mass sectors such as continental, marine and polluted regions. Then back trajectory analysis, which is performed via the use of a specialized model, could be used to determine the origin, and thus composition of aerosol parcels at the local site.

SSA_{368-nm} The second panel shows SSA_{368-nm} varying between about 0.8 and 0.95, indicating significant changes in the scattering properties of the aerosols. The monthly mean value is 0.88. The values here are similar to those for the "highly scattering" atmosphere discussed in Section 5a. Recall that the retrieval performed best under these conditions and that retrieval results improved for SSA and g with increasing turbidity. The change in air mass regime is clearly present from May 15 to 17. Overall these values fall within those reported by other researchers as discussed in Section ii.

TOC The middle panel shows retrieved TOC varying between about 260 and 320 DU over the course of the month, with a monthly mean of 285 DU. There are diurnal fluctuations of about 15 DU with a minimum in the middle of the day. There are two general trends evident in the TOC data set; first a decrease in daily TOC from about 310 DU to 270 DU over the first half of the month followed by a sharp jump in TOC to about 290

DU after the air mass regime change, which then has a roughly parabolic shape over the following 10 days with a minimum around 275 DU on May 21.

Asymmetry Factor (g) Plotted in panel 4 is the retrieved asymmetry factor which varies between about 0.6 and 1.0, with a monthly mean of 0.77. Recall that the *a priori* value was 0.70. Increasing g is correlated with increasing AOD. Larger values of g indicate more forward scattering. This is expected from larger sized particles such as soot and desert dust, which have been shown to have $g \simeq 0.9$ Wenny et al. (1998). The increase in g could therefore be attributed to large dust particles which are likely common at the Panther Junction site. Again the regime change is apparent in this data set at which time the asymmetry factor drops sharply indicating smaller particles after the passing of the event.

Ångstrom exponent (α) The bottom panel in the figure shows the time series of the Ångstrom exponent (α) which was calculated from the expression given by Eqn. 36 in Section iv, using wavelengths 332- and 368-nm. The plotted values were filtered by removing the outliers greater than 2 standard deviations from the mean. In general, the filtered values fall between 0 and 1.2, with a monthly mean of 0.71 and standard deviation of 0.26. The direction of the wavelength dependence in AOD given by the calculated Ångstrom exponent agrees with values obtained from current literature, e.g., Kylling et al. (1998), Wetzel et al. (2003).

ii. Monthly retrieval error time series The estimated errors in each of the retrieved parameters were calculated from $\hat{\mathbf{S}}$ as discussed in Section ii for the May 2003 time series and are shown in Figure 28 along with the χ^2 values in the bottom panel. Note that only the results for AOD and SSA at one channel (368-nm) are shown for brevity and clarity.

AOD_{368-nm} Errors The errors in AOD_{368-nm} are roughly inversely proportional to the value of AOD_{368-nm}, and range from about 2% to 28% with a mean of 10.4%. This corroborates well with the results from the synthetic retrieval testing, which showed decreasing error in all parameter, especially AOD, with increasing turbidity. There appears to be a diurnal variation in the AOD_{368-nm} errors, but as will be discussed later, the variation in percent error scales with the changing AOD_{368-nm}, such that the absolute magnitude of the error remains roughly constant on any particular day.

SSA_{368-nm} Errors The estimated errors in SSA_{368-nm} vary between 2.5% and 5.7% with a mean of 4.3%. The diurnal fluctuations in the error also scale with the diurnal fluctuations in SSA_{368-nm}, producing error bars of essentially constant size. Note that the absolute magnitude of error in SSA_{368-nm} is a much more significant fraction of the range in the variable than that of the AOD_{368-nm}, indicating that SSA_{368-nm} is not as well determined as AOD_{368-nm}.

TOC Errors The estimated errors in TOC vary between 1.0% and 3.9% with a mean of 2.0% and again, a diurnal fluctuation producing roughly constant error bars on the daily data. The mean error value in the OE retrieved TOC corresponds exactly to that reported for the direct sun technique Gao et al. (2001).

Asymmetry Factor Errors The estimated errors in asymmetry factor vary between 7.0% and 15.0% with a mean of 11.2%. As with retrieved SSA_{368-nm}, the magnitude of the error in g comprises a substantial portion of the physical range of variability, indicating uncertain knowledge in the estimated values. Note that, as for AOD_{368-nm}, the retrieval algorithm was shown to produce the best estimate for g when the atmospheric state is one of high scattering and high turbidity.

iii. Monthly retrieval diagnostic time series Figure 29 shows plots of the time series of the A-matrix values for select parameter types, as well as the retrieval information content, dof values and dof ratio from the May 2003 retrieval data set. Note that only the results for AOD and SSA at one channel (368-nm) are shown for brevity and clarity.

AOD_{368-nm} and TOC A-matrix Values The top panel shows the A-matrix values for the AOD_{368-nm} and the TOC. The AOD_{368-nm} A-matrix values have a monthly mean of 0.99 with standard deviation 0.005, while the TOC A-matrix values have a mean of 0.93 with standard deviation 0.042. Recall from Section ii that A-matrix values of 1 indicate total reliance on the measurements while A-matrix values of 0 correspond to total reliance on the *a priori* in the retrieval algorithm's estimate of the parameter. Therefore the values of AOD_{368-nm} are almost completely determined by the measurements while the reliance for TOC is generally between about 75% and 98%. The TOC A-matrix values decrease with increasing turbidity, a result that was also discovered in the synthetic retrieval testing. For AOD_{368-nm} lower than about 0.5, the TOC is determined about 95% by the measurements, but the determination is less reliant on the measurements for greater values of AOD_{368-nm}. Note however, that the synthetic retrieval of TOC was just as close to "truth" for high turbidity conditions as for low even though the A-matrix value was smaller, indicating that sufficient information for determining this parameter is contained in the measurements in all cases.

SSA_{368-nm} and Asymmetry Factor A-matrix Values The A-matrix values for SSA_{368-nm} and asymmetry factor are shown in panel 2 of Fig. 29. There is much greater variability in these A-matrix values and in general they are lower than those of the parameters in panel 1, indicating that these retrieval parameters are not as well determined by the measurements. The monthly mean A-matrix values for SSA_{368-nm} is 0.42 with standard deviation of 0.17, while for g the mean is 0.30 with standard deviation of 0.10. Both

of these A-matrix values are approximately directly proportional to the value of the retrieval parameter. The best retrieval of these parameters was shown to occur for "highly scattering" situations as was determined from the synthetic testing. The low A-matrix values, as compared to those for AOD_{368-nm} and TOC, are a direct result of the low sensitivity of the forward model for these particular parameters as inferred from Eqn. 68 and discussed in that section.

Shannon Information Content (H) Panel 3 of Fig. 29 shows the Shannon information content as was discussed in Section ii. The mean monthly value is 23.2 with standard deviation of 2.9. There is a strong diurnal variation in the values. The daily mean value appears to be correlated with AOD_{368-nm}, i.e., increasing H with increasing turbidity. The values are given in bits and from Eqn. 83 the reduction in the uncertainty of the retrieved state relative to the *a priori* due to addition of the measurements in terms of the monthly average is $2^H = 2^{23.2} = 9.6\text{x}10^6$ times.

Degrees of Freedom Shown in panel 4 of Fig. 29 are the degrees of freedom for *a priori*, signal and measurement as discussed in Section ii. The dof_a remain constant at 13.9 since this number is determined by the trace of the $\mathbf{S_a}$ matrix, which is invariant during the retrieval. The dof_s fluctuates between about 8 and 11.5, with mean 9.2 and standard deviation 0.86, indicating the number of independent measurements available for determining the retrieval parameters. This number is interpreted as the effective rank of the problem in measurement space. The dof_m have discrete values between 7 and 12 with mean 9.4 and standard deviation 1.3. This number is interpreted as the effective rank of the problem in state space. The mean condition of the posed retrieval problem can therefore be written as $p = 9.2 < m = 14 < n = 16$, which leads to a class 4 problem according to Table 2 in Section 3a. This type of problem is described as both under- and over-constrained, because there are more unknowns than measurements, and

the measurements are not all independent.

Degrees of Freedom Ratio The bottom panel in Fig. 29 shows the values of dof_R calculated using Eqn. 72. The range in values is 0.53 to 0.84 with monthly mean 0.67 and standard deviation 0.06. Recall from the discussion in Section ii that a value of dof_R equal to 1 indicates a well posed problem, while fractions of 1 are indicative of ill-posed problems. In this particular monthly retrieval data set the number of independent measurements is roughly 67% of the number of independent parameters being sought. The value of dof_R is directly proportional to both AOD_{368-nm} and SSA_{368-nm}, i.e., proportional to the turbidity and scattering conditions, indicating that the retrieval is less ill-posed under these atmospheric conditions because more information is available in the measurements via higher model sensitivity. The value of dof_R could be increased toward 1 by increasing the value of *scale* in Eqn. 88, which would have the effect of reducing dof_a, and hence dof_R. However, as discussed in Section iv an increase in *scale* leads to a decrease in the A-matrix values and to less significance in the retrieved values according to the χ^2 statistic as was demonstrated in Fig 26.

iv. Detailed Analysis of the Ångstrom Exponent Comparison of the wavelength dependence of the AOD is performed through analysis of the Ångstrom exponent, α. Positive values of α indicate decreasing AOD with increasing wavelength as interpreted from Eqn. 36. Furthermore, larger values of α are associated with smaller aerosol particles and vice versa, as discussed in Section iv. The daily average values of α for the May 2003 retrieved data set are plotted against the right ordinate in Figure 30 along with the daily averaged values of AOD_{368-nm} against the left ordinate. The Ångstrom exponent is inversely proportional to AOD_{368-nm}, i.e., decreasing α with increasing turbidity. The values of Ångstrom exponent fall between 0.2 and 1.1 with a mean of 0.53. These values are substantially lower than those reported by Wetzel *et al.* in central Alaska, a phe-

nomena which may be explained by the presence of dust (larger particles) at the Panther Junction site, versus more pristine air in Alaska Wetzel et al. (2003). If we concede that the large AOD_{368-nm} events centered on May 12 and 27 are in fact due to local dust storms then the associated decrease in α is physically plausible. The values of Ångstrom exponent measured by Kylling *et al.* at two locations in Greece show a larger variability than the OE retrieved values presented here and also show some correlation with AOD_{355-nm}.

To examine the correlation between AOD_{368-nm} and α more closely, Figure 31 shows a scatter plot of all retrieved scans for these two variables from the May 2003 data set. The values are plotted in four groups according to the air mass regimes as discussed in reference to Figure 27; days 1-9 correspond to relatively low AOD_{368-nm}, days 10-15 correspond to the build up of AOD_{368-nm} prior to the regime change, day 12 corresponds to the peak AOD_{368-nm} of the event, while days 16-31 correspond to the post regime change air mass. The mean and standard deviations of both the AOD_{368-nm} and Ångstrom exponents for these time periods are summarized in Table 15.

The data for days 1-9 show a period of low AOD_{368-nm} and large variability in α, indicating a variety of aerosol composition and size distributions. Recall, however, that the retrieval results tend to have large uncertainties at low AOD, which could be responsible for the large variability in α. The data for days 10-15 show a period of larger AOD_{368-nm} with roughly equivalent values of α as in the first 9 days, but with lower variability, indicating greater stability of the aerosol composition through this time period or greater accuracy of the retrieval results. Day 12 was plotted separately out of this time period as it seems to indicate a very stable aerosol composition on this day as indicated by the low standard deviation in α. This high turbidity condition also corresponds to the best accuracy in the retrieval as determined from the synthetic testing. The final time range, consisting of days 16-31, is a period of moderate AOD_{368-nm} values with higher mean

Table 15: Mean and standard deviations of Ångstrom exponents vs. AOD.

	AOD		α	
Day Range	**Mean**	**Std Dev**	**Mean**	**Std Dev**
1-9	0.22	0.11	0.62	0.34
10-15	0.52	0.28	0.59	0.19
12	0.97	0.09	0.66	0.04
16-31	0.34	0.20	0.80	0.23

α values than prior to the change in air mass. Since large values of α can be interpreted as the presence of small aerosol particles it can be inferred that the post regime change air mass contains smaller particles relative to the prior air mass. Again this could easily be interpreted as a dust event at the site around May 12 which would correspond to large aerosol particles.

This plot looks qualitatively similar to Figure 2 in Kylling *et al.*, which indicates slightly larger α and decreasing variability with increasing AOD Kylling et al. (1998). Kylling *et al.* state that the large variability in α for their Figure 2 (bottom) relative to their Figure 2 (top) may be due to the short spectral range of the Brewer instrument (287.5- to 366-nm) from which the Ångstrom coefficients were calculated Kylling et al. (1998). The Ångstrom coefficients presented here from the OE retrieval were calculated using AOD at 332- and 368-nm, since these are the most reliable values according to the retrieval diagnostics. It is possible that the α - AOD scatter could be reduced by calculating α using a longer wavelength range such as 311- to 368-nm, but this has not been investigated.

v. Daily retrieval comparisons More in depth analysis of the retrieval data was performed for select days May 12 and 22, which serve as representatives of a high turbidity case prior to the air mass regime change and a low turbidity case after the air mass regime change, respectively. These two cases also correspond to situations in which the

retrieval results are likely to have small uncertainties (high turbidity) and large uncertainties (low turbidity). Figure 32 shows plots of the direct, diffuse and total components of the UV-MFRSR measured irradiances at 368-nm for these two days plotted against the left ordinate. Plotted against the right ordinate in this figure are the direct-to-diffuse ratios (DDR). Recall that on a clear sky day the direct and diffuse components of the beam are approximately equal in the UV spectral range, as was discussed in Section v.

On May 12 (top panel) the direct component is only half that of the diffuse, indicating strong scattering of the incident UV light as would be due to the presence of aerosol. On May 22 (lower panel) the direct beam is about one and a half times that of the diffuse beam, indicating less scattering and hence lower aerosol content. The change in DDR can also be interpreted partially as a change in the scattering properties of the local aerosol. However, the sensitivity study performed by Petters *et al.* found that a change in AOD has the largest effect on the DDR, while a change in SSA was found to have the second largest effect on DDR, followed by changes in g, surface albedo and TOC Petters et al. (2003). Their sensitivity testing indicated that at relatively large AOD (1.0) the DDR increased from about 1.5 to 2.0 with a change in SSA from 0.75 to 0.90.

Intercomparison with independent methods: May 12, 2003 Figure 33 shows the daily time series of AOD_{368-nm}, SSA_{368-nm}, TOC, g and Ångstrom exponent for 12 May, 2003 at Panther Junction, Texas, along with the corresponding A-matrix values plotted on the right ordinate. For that particular day there were 140 retrieved cloud screened scans. After application of the 95% χ^2 filter, 114 scans remained. Table 16 provides a summary of the statistics from the daily retrieval. Error bars are plotted on the OE retrieved quantities as calculated from the retrieval error covariance matrix (see Section ii).

In panel 1 the OE AOD_{368-nm} values are over-plotted on top of the UVMRP calculated AOD_{368-nm} derived via the Langley method. The AOD_{368-nm} on this particular

Table 16: Retrieval information from Panther Junction, May 2003.

	May 12	**May 22**
N (cloud-screened)	140	179
N (retrieved)	140	174
N (χ^2 filtered)	114	154
N α	102	56
Range (time)	8:18 - 15:39	7:51 - 17:39
Range (SZA)	62.78 - 39.61	67.74 - 64.74

day decay from about 1.05 in the early part of the day to about 0.85 in the afternoon, at which time there is a break in the retrieved data set due to the χ^2 filtering (χ^2 too low). After the lapse in the data set the AOD_{368-nm} values increase from about 0.7 to 0.9. The non-filtered data set (not shown) shows smooth variation in AOD_{368-nm} during the lapse. The OE retrieved and Langley derived data sets overlap well within the OE error bars and have a RMS difference of 0.0087. The relatively large values of AOD_{368-nm} corresponds to a low direct-to-diffuse irradiance ratio as discussed previously due to the greater number of aerosol particles available for scattering of the direct beam. The A-matrix values for AOD_{368-nm} are very close to 1 throughout the day.

Shown in panel 2 are the OE retrieved SSA_{368-nm}, for which there are no independent sources for comparison. The diurnal variation in SSA_{368-nm} appears to be well correlated with the variation in AOD_{368-nm} and ranges from about 0.91 in the early part of the day down to about 0.89 in the afternoon. Note however that a zero-slope line can easily be fit to the SSA_{368-nm} data within the error bars, indicating that the small diurnal variation is insignificant. Following the break in the data set there is a steady increase in SSA_{368-nm} to about 0.92 in the later part of the day. Note that the relatively large values of SSA_{368-nm}, along with AOD_{368-nm} around 1.0, fulfill the requirement of the "highly scattering" atmosphere discussed in Section 5a with regard to the synthetic retrievals. Hence the retrieved values on this particular day can be considered accurate.

The non-filtered data set (not shown) shows a smooth parabolic shape with the minimum around local noon. Kylling *et al.* claim that SSA "undoubtedly has a diurnal variation" Kylling et al. (1998), but give no supporting argument for this claim. One hypothesis for this variation is that changes in relative humidity throughout the day would cause hygroscopic particles to become saturated or encased with water. These particles would then absorb more UV radiation, causing a decrease in SSA values. The OE retrieved SSA_{368-nm} on this particular day closely match the results obtained by Petters *et al.* of SSA_{368-nm}=0.89 with AOD_{340-nm}=0.5, averaged over 11 retrievals with varying air masses. The range in estimated OE error is 0.86 to 0.95 (uncertainty $\pm$0.045) which is similar to the results obtained by Petters *et al.* of $\pm$0.04 at AOD=1.0, averaged over the 7 UV-MFRSR channels. The OE SSA_{368-nm} results also are in general agreement with those from other studies conducted at various locations as was discussed in Section ii. The A-matrix values for SSA_{368-nm} on this day range between about 0.8 and 0.65, corroborating the idea that the algorithm can provide reasonable retrieval of SSA during high turbidity conditions for a highly scattering atmosphere. Hence, the confidence in the retrieved values of SSA_{368-nm} on this particular day is high.

Panel 3 of Fig. 33 shows the UVMRP calculated values of TOC derived via the direct sun method Gao et al. (2001), over-plotted with the OE retrieved TOC values with associated error bars (constant $\pm$2% for the UVMRP direct sun method). The values on this particular day lie in the range 260 to 270 DU. The two data sets fall within uncertainties with RMS difference of 5.8 DU. A parabolic diurnal variation of about 10 DU with a minimum around solar noon is present in the UVMRP data set. The OE retrieved TOC appears to follow more of a constant decay throughout the day with only a slight increase at the very end. It is possible to fit a zero-slope line through the TOC data within the error bars, indicating the non-significance of the diurnal fluctuations. Recall from the synthetic retrieval testing that the uncertainty in retrieved TOC was larger for

high turbidity conditions. The A-matrix values for TOC on this day are around 0.85.

Panel 4 of Fig. 33 shows the values of asymmetry factor, which fall around 0.87 for the first part of the day, but have a large increase in the values in the afternoon. The error in this retrieval parameter is fairly large and indicates a range in values of between about 0.80 and 1.0. The median of this range of values in g coincides with the value of 0.90 given by Madronich (as discussed in iii) for soot and desert aerosols, particles which are expected to be found at this particular measurement site. There are no known independent sources with which to compare asymmetry factor for this particular data set. The A-matrix values for retrieved g on this day range from about 0.3 in the morning to about 0.5 in the afternoon. This indicates that the estimated value of this parameter is somewhat tenuous and that the results should be interpreted with care.

The bottom panel of Fig. 33 shows the intercomparison between calculated Ångstrom exponent from both the UVMRP Langley AOD values and the OE retrieved AOD values. The additional filtering process applied when calculating these values as discussed in Section iv left 102 of the 114 χ^2 filtered scans for analysis. There is a clear bias in the data sets, yielding a RMS difference of 0.54, with the OE values having a mean of 0.67 and standard deviation of only 0.04, while the UVMRP values have a mean of 0.52 with a much larger standard deviation of 0.52 (it is coincidental that the mean and standard deviation on this day are equivalent). There appears to be discrete values between which the UVMRP calculated Ångstrom exponents drift. Furthermore, note that there are some large outliers at both the beginning and end of the time series. Overall these values of α indicate the consistency of the aerosol composition on this particular day.

Intercomparison with independent methods: May 22, 2003 Figure 34 shows the daily time series of AOD_{368-nm}, SSA_{368-nm}, TOC, g and Ångstrom exponent for 22 May, 2003 at Panther Junction, Texas, with the A-matrix values plotted against the right ordinate. For that particular day there were 174 retrieved cloud screened scans. After

application of the 95% χ^2 filter 154 scans remained. Table 16 provides a summary of the statistics from the daily retrieval. Error bars are plotted on the OE retrieved quantities as calculated from the retrieval error covariance matrix (see Section ii).

Panel 1 shows that the AOD_{368-nm} on this particular day remain almost constant at 0.3 with an OE estimated uncertainty of about ± 0.05. The OE and UVMRP data sets overlap well within the OE error bars and have a RMS difference of 0.012 as calculated from the $N = 154$ scans remaining after the χ^2 filtering was applied. This low value of AOD corresponds to a high direct-to-diffuse irradiance ratio as discussed previously since there is relatively little aerosol present to cause scattering. Furthermore, the low AOD corresponds to low turbidity, which was shown to yield somewhat tenuous retrieval results, especially for SSA and g, even for "highly scattering" atmospheres. The A-matrix values are near 1 throughout the day, indicating strong reliance on the measurements. Note that the retrieval of AOD_{368-nm} is well determined and has reasonably small error even under relatively low turbidity conditions.

Shown in panel 2 of Figure 34 are the OE retrieved SSA_{368-nm}, for which there are no independent sources for comparison. There is again a small diurnal variation present in AOD_{368-nm}, with a minimum around noon and the beginning of a sharp increase in the trend prior to a section of data being filtered by the χ^2 stipulation. The unfiltered data set (not shown) has SSA reaching a peak of 0.95 at time 15:30, were it remains for about 45 minutes before again abruptly falling back to about 0.89 at 16:15 as seen in the figure. Most of the scans missing between 16:15 and 17:40 have been cloud screened rather than χ^2 filtered. The range in estimated OE error is 0.84 to 0.95 (uncertainty ± 0.055) which is again similar to the results obtained by Petters *et al.* of ± 0.04 at AOD=1.0, averaged over the 7 UV-MFRSR channels. The OE AOD_{368-nm} results also are in general agreement with those from other studies conducted at various locations. The A-matrix values on this day range from about 0.3 to 0.7 with a mean value substantially lower than that from

May 12. Recall from the synthetic testing that the retrieval of AOD_{368-nm} is not as well conditioned for low turbidity scenarios.

Panel 3 of Figure 34 shows the UVMRP calculated values of TOC derived via the direct sun method Gao et al. (2001) over-plotted with the OE retrieved TOC values with associated error bars (constant $\pm 2\%$ for the UVMRP direct sun method). The values on this particular day lie in the range 280 to 295 DU. For the most part the two data sets fall within the overlapping uncertainties, which are about ± 3 DU for both sets, with RMS difference of 5.6 DU. A small decay in the values is noticeable at the beginning of the day in both data sets but for the majority of the day the values remain basically constant. The non χ^2 filtered data (not shown) shows a sudden drop in the OE retrieved TOC of about 7 DU as the local time approaches the time of the cloud screened scans ($\sim$ 15:00). This shift appears to be in conjunction with the shift in SSA_{368-nm} that was mentioned in the preceding paragraph. It is hard to determine if this shift is a by-product of the OE algorithm trying to find the best statistical fit to the data or due to the presence of cloud not detected by the cloud screening algorithm, but it is noted that this shift does not take place in the UVMRP TOC values. The A-matrix values are about 0.9 for much of the day, indicating that the measurements contain about 90% of the information relative to the *a priori* in determining the estimated values of TOC.

Panel 4 of Figure 34 shows the values of asymmetry factor, which begin around 0.81 and decay smoothly to about 0.75 through the afternoon, followed by a rather sharp increase to about 0.83 prior to the χ^2 filtered data. The error in this retrieval parameter is fairly large and indicates a range in values of between about 0.68 and 0.92. This range of values in g coincides somewhat with the range for sulfate, marine and small dust given by Madronich (as discussed in Section iii). It is interesting to note that the regime change observed in the full monthly time series data set (Figure 27) suggests a change in the air mass type which is heavily supported by this large change in the asymmetry factor.

There are no known independent sources with which to compare asymmetry factor for this particular data set. The A-matrix values drift between about 0.2 and 0.4, indicating that there is not much information provided by the measurements for determining this parameter.

The final panel shows the intercomparison between calculated Ångstrom exponent from both the UVMRP Langley AOD values and the OE retrieved AOD values. The additional filtering process applied when calculating these values as discussed in Section iv left only 56 of the 154 χ^2 filtered scans for analysis. There is a small bias in the data sets, yielding a RMS difference of 0.54, with the OE values having a mean of 0.61 and standard deviation of 0.16, while the UVMRP values have a mean of 0.82 with a much larger standard deviation of 0.47. Note that the sign of the bias is opposite that on May 12. Furthermore, note that there are still some large outliers in the UVMRP time series even after the σ filtering was performed. Overall these values of α match those obtained by Kylling *et al.* from their studies in Greece Kylling et al. (1998), indicating physically reasonable results.

SSA wavelength comparisons Figures 35 and 36 show the daily retrieved values of the SSA for all 7 wavelength channels from May 12 and May 22, 2003 at Panther Junction as well as the associated A-matrix values. There is some diurnal dependence in the retrieved values of SSA, especially at the longer wavelengths. Comparison of the A-matrix values from the two days indicates that there is considerably more information in the measurements on May 12 than May 22 (mean A-matrix value 0.59 on May 12 versus 0.29 on May 22) which also had higher AOD ($AOD_{368-nm} \simeq 1.0$ on May 12 versus $AOD_{368-nm} \simeq 0.3$ on May 22). This result supports the SSA uncertainty analysis of Petters *et al.* who found decreasing uncertainty with increasing AOD (see Figure 5 Petters et al. (2003)). This result is also supported by the synthetic retrieval testing which showed decreasing retrieval error and increasing SSA A-matrix values with increasing

turbidity for the "highly scattering" scenario.

The A-matrix values for SSA_{300-nm} are close to zero on both days, indicating that AOD_{300-nm} can not be retrieved from the information available in the measurements. It is clear that on this particular day the value of the SSA is directly proportional to increasing wavelength. This wavelength dependence again agrees with findings by Petters *et al.* in North Carolina Petters et al. (2003), but is opposite that retrieved using the original version of this algorithm in Mexico City in 2003 Goering et al. (2005).

It was mentioned in Section ii that using the A-matrix values as a quantification of the quality of a retrieval is perhaps desirable. Since the A-matrix values associated with the 7 channel AOD values and the TOC were always relatively large, and the values associated with g are relatively low, screening the data based on these parameters will not be considered. Instead the focus will be on using the A-matrix values associated with the retrieved SSA values. Recall that in the DDR technique of Petters *et al.*, used to determine values of SSA, they concluded that a minimum threshold of AOD $\geq$0.3 was necessary in order to obtain a reasonable SSA retrieval based on sensitivity studies Petters et al. (2003). The optimal estimation results from May 22, which had a mean AOD_{368-nm} of $\simeq$ 0.3, can then be used to determine a minimum A-matrix value. Since the SSA A-matrix values were about 0.30 on this day for all wavelengths except 300-nm, 0.30 seems a reasonable minimum threshold to use for post-screening the retrieval data. Physically this threshold is interpreted as follows; if the A-matrix values associated with any of the $SSS_{305-nm} \rightarrow SSS_{368-nm}$ fall below 0.30, meaning that the measurements contributed less than 30% of the information to the retrieved value of SSA at that wavelength, then the retrieved value of SSA for that particular scan at that wavelength should be flagged as "uncertain". Note however, that the optimal estimation retrieval was shown to produce high quality results for some parameters even when the AOD is less than the Petters *et al.* minimum threshold of 0.3, assuming that the scattering properties of the atmosphere

were not too low.

To compare the wavelength dependence of SSA more directly with those retrieved by Petters *et al.* in North Carolina, plots of SSA versus wavelength are shown in Figure 37 using a daily averaged value from the OE retrieval on May 22, 2003 from Panther Junction and the 11 daily values obtained from Table 1 of Petters et al. (2003). The date and the air mass type for the Petters *et al.* data are indicated in the legend, where C indicates continental, M marine and HP highly polluted. It is clear that the variability in the Petters *et al.* data is quite large, but the average of all 11 days (plotted as red triangles with dotted line) is actually surprisingly close to that retrieved in Panther Junction (plotted as black +'s with dotted line). Even the strength of the wavelength dependence scales quite well, excepting a small dip in SSS_{317-nm} and SSS_{325-nm} in the Petters *et al.* data.

Retrieval Testing without Cloud-Screening Applied It has been suggested that the Delta-Eddington radiative transfer approximation could be used as a cloud screening tool by way of the χ^2 statistic or by failed retrievals [L'Ecuyer, personal communication]. The logic here is that the algorithm can be run rapidly using this approximation (refer back to Table 4). If there are clouds or thick water vapor present, the retrieval algorithm should have trouble converging on a solution, or at least provide a poor χ^2 value if it does converge. After the full data set is screened in this way, the algorithm would be rerun using the 4-stream discrete ordinate approximation to provide usable retrieval results. This would provide a self consistent means for screening the irradiance data set, rather than relying on precalculated Langley AOD values, as is currently done using the Smirnov *et al.* screening Smirnov et al. (2000). An alternative method is to implement the more robust cloud screening algorithm of Long and Ackerman Long and Ackerman (2000). This technique relies on broadband pyranometer measured irradiances and was used by Goering *et al.* for cloud screening of the Mexico City data set Goering et al. (2005). However the code was not immediately available for use in this research;

To test the feasibility of using the χ^2 statistic as a cloud-screening tool, the full set of non-cloud screened irradiance data from May 24 was used as input into the retrieval algorithm. The test retrieval was able to converge successfully on 142 of the 274 scans in the full data file (52%), compared to convergence of 95 of the 97 scans (98%) in the original monthly run of the cloud-screened data. Figure 38 highlights some results of the testing. Shown in the top panel of the figure are time series plots of the 368-nm direct irradiance plotted as red diamonds and the direct-to-diffuse irradiance ratio (DDR) plotted as a red dash-dotted line, both against the left ordinate. The χ^2 values are plotted as blue asterisks against the right ordinate along with the upper boundary of the 95% confidence interval as a solid blue line. Analysis indicates that when the 368-nm direct irradiances are close to zero, and hence DDR also close to zero, the values of χ^2 become very large, in excess of 100. Note that there are much fewer individual χ^2 points ($N = 104$), relative to the number of measured irradiance points ($N = 274$), since the retrieval often was unable to converge due to cloud contamination.

Shown in the lower panel of Figure 38 are time series plots of the retrieved AOD_{368-nm} (red diamonds against the left ordinate), as well as the χ^2 values. This plot indicates that the excessively large χ^2 (> 100) correspond to retrieved AOD_{368-nm} greater than about 1.2. Since AOD_{368-nm} much larger than 1 is unphysical except under the most extreme conditions, e.g., perhaps in a smoke plume, it can be assumed that these large AOD_{368-nm} actually correspond to cloudy conditions. In this case, the large χ^2 values could be used as an indicator of cloudy conditions. Note that this test retrieval on May 24, 2003 at Panther Junction was calculated using the normal operating mode of the retrieval algorithm, i.e., Delta-Eddington approximation on the first iteration, followed by the 4-stream Discrete Ordinate Method, and required about 174 minutes of computation time.

6d. *Summary of Retrieval Results and Intercomparisons*

Based on the one month time series of data from May, 2003 at Panther Junction, Texas, the overall performance of the optimal estimation retrieval can be summarized as follows. Based on the input error budget that was characterized through model sensitivity testing, measurement error analysis and instrument calibration error analysis, about 50% of successfully converged retrieval scans were significant at the 95% level. The retrieved results of AOD_{368-nm}, SSA_{368-nm}, TOC and g showed realistic variations in time. The retrieved values of AOD_{368-nm}, TOC and g had inversely proportional error, while SSA_{368-nm} had directly proportional error. The A-matrix values showed that AOD_{368-nm} and TOC were well determined by the measurements, while the determination of SSA_{368-nm} and g were directly proportional to the scattering properties of the atmospheric state. The dof analysis showed that the retrieval approached the well-posed condition as the turbidity increased, i.e., $dof_R \rightarrow 1$ as AOD increased. Finally, detailed intercomparisons to independent methods for AOD_{368-nm}, TOC and Ångstrom exponent indicated favorable results, i.e., low RMS differences.

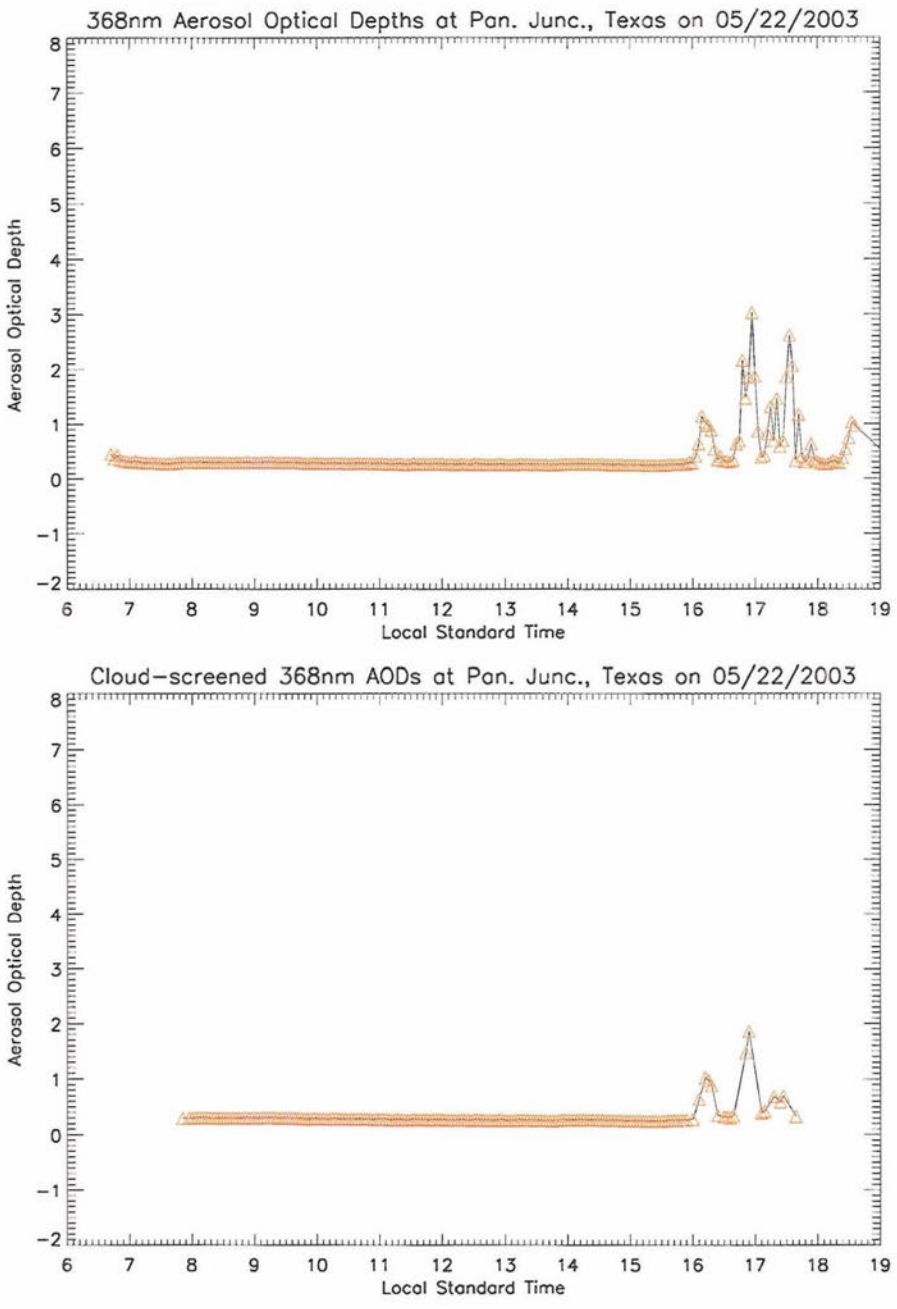

Figure 25: Time series of AOD_{368-nm} on May 22, 2003 from Panther Junction, Texas as calculated by the UVMRP and used in the cloud screening algorithm (top panel). Time series of the AOD_{368-nm} remaining after application of screening algorithm (bottom panel).

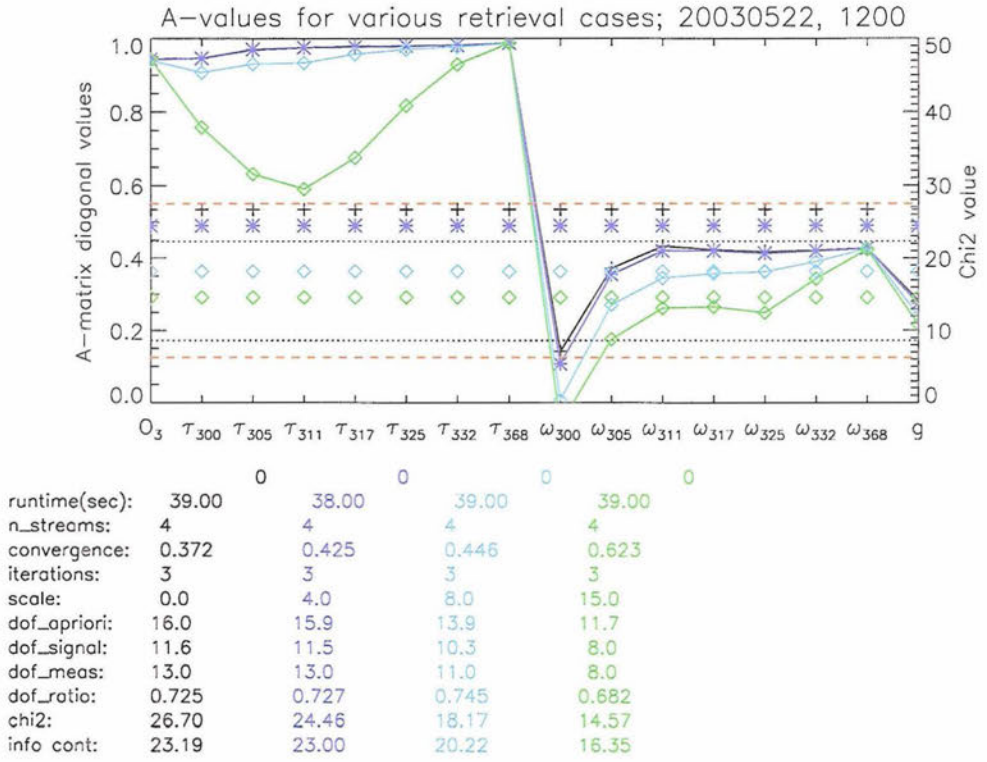

Figure 26: A-matrix diagonal values (left ordinate) for the 16 retrieval parameters produced by the retrieval algorithm for various cases of the *scale* factor used in the $\mathbf{S_a}$ off-diagonal correlation equation. Each color represents a retrieval run with *scale* set to a different value. Plotted on the right ordinate are the χ^2 values with the 80% and 95% confidence intervals plotted as black dotted and dashed red lines, respectively. All cases are for the noon scan on May 22, 2003 at Panther Junction, Texas. Additional information pertaining to each case is given below the graph in the corresponding color.

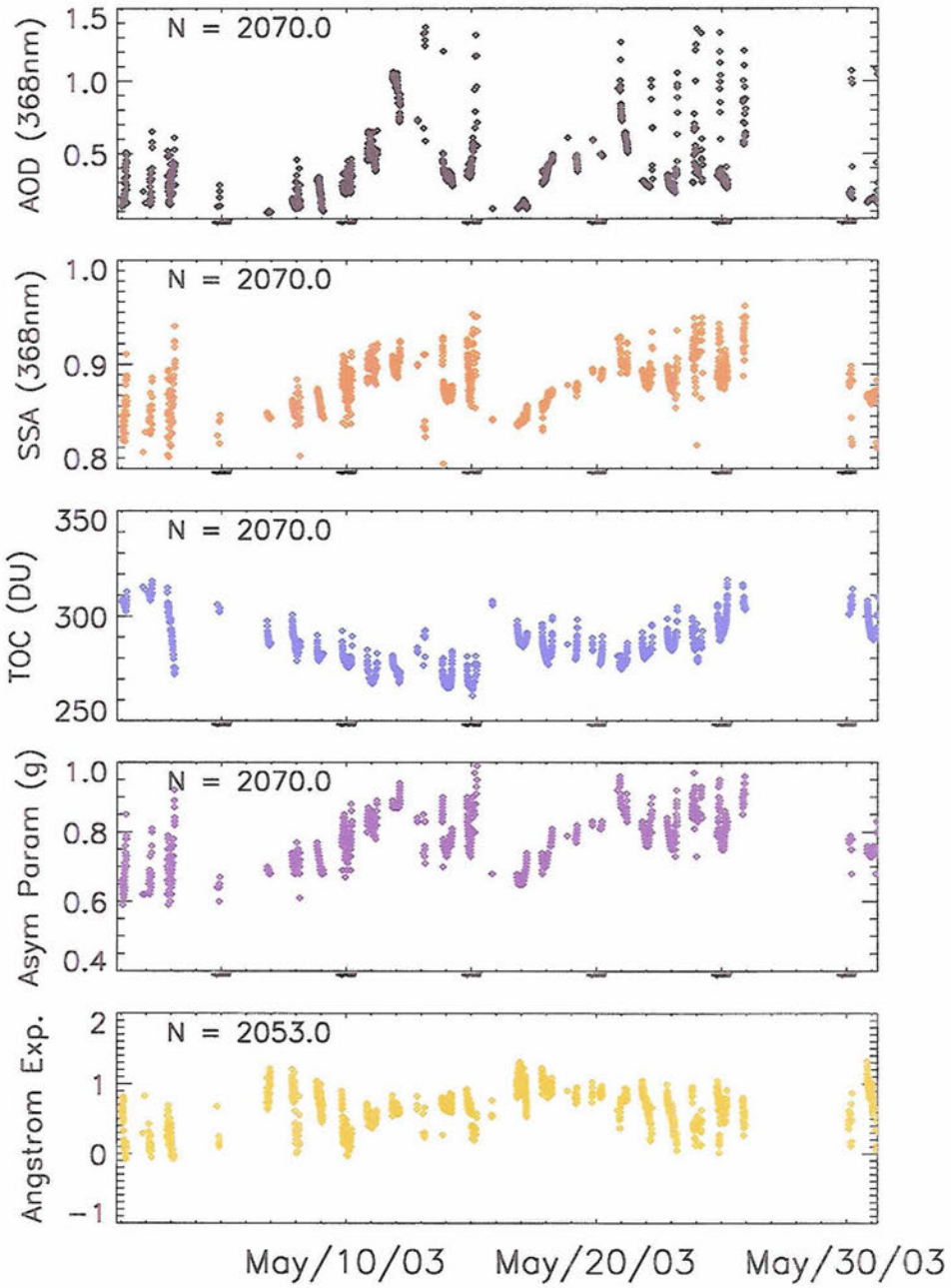

Figure 27: Retrieved values of AOD_{368-nm} (top panel), SSA_{368-nm} (2nd panel), TOC (3rd panel), asymmetry factor (4th panel) and calculated Ångstrom exponent (bottom panel) for May 2003 at Panther Junction, Texas.

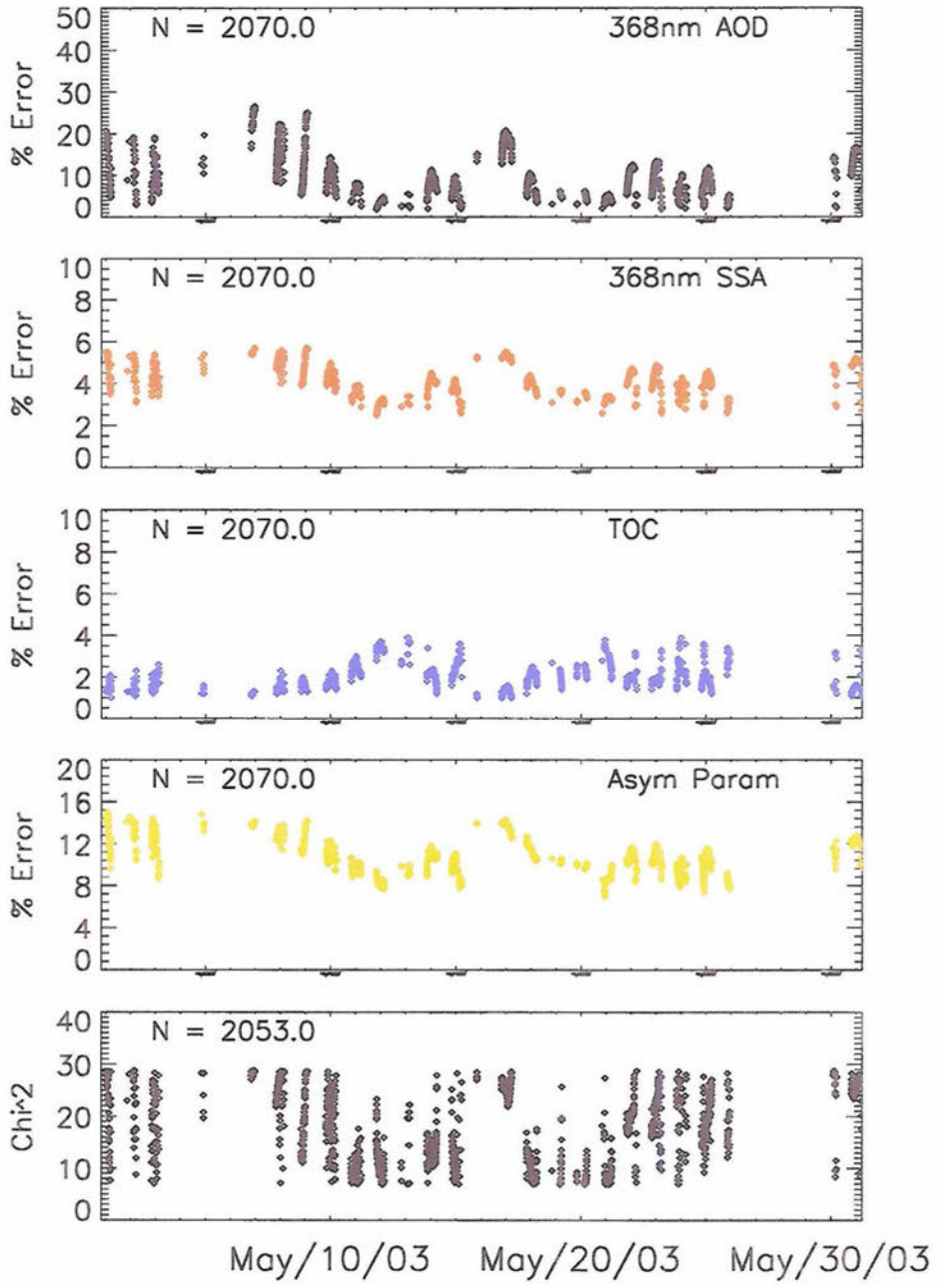

Figure 28: Estimated retrieval errors calculated from $\hat{\mathbf{S}}$ for May 2003 at Panther Junction, Texas for the following parameters; AOD_{368-nm} (top panel), SSA_{368-nm} (2nd panel), TOC (3rd panel), asymmetry factor (4th panel). Bottom panel shows χ^2 values. Note the difference in the ranges of the ordinate scale for the various parameters.

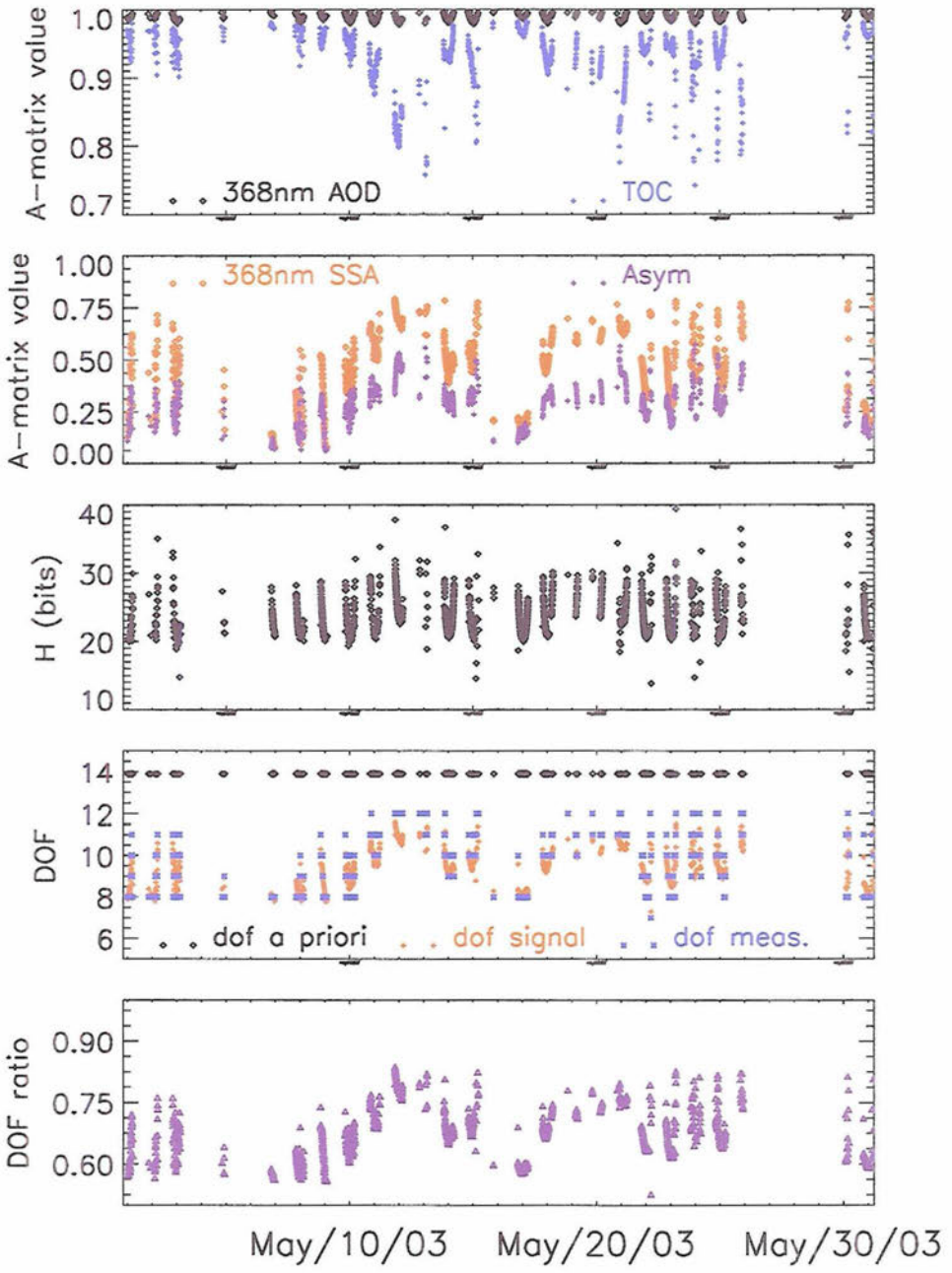

Figure 29: Retrieval diagnostics for May 2003 at Panther Junction, Texas. A-matrix values for AOD_{368-nm} and TOC (top panel), A-matrix values for SSA_{368-nm} and asymmetry factor (2nd panel), information content (3rd panel), dof_a, dof_s and dof_m (4th panel) and dof_R (bottom panel).

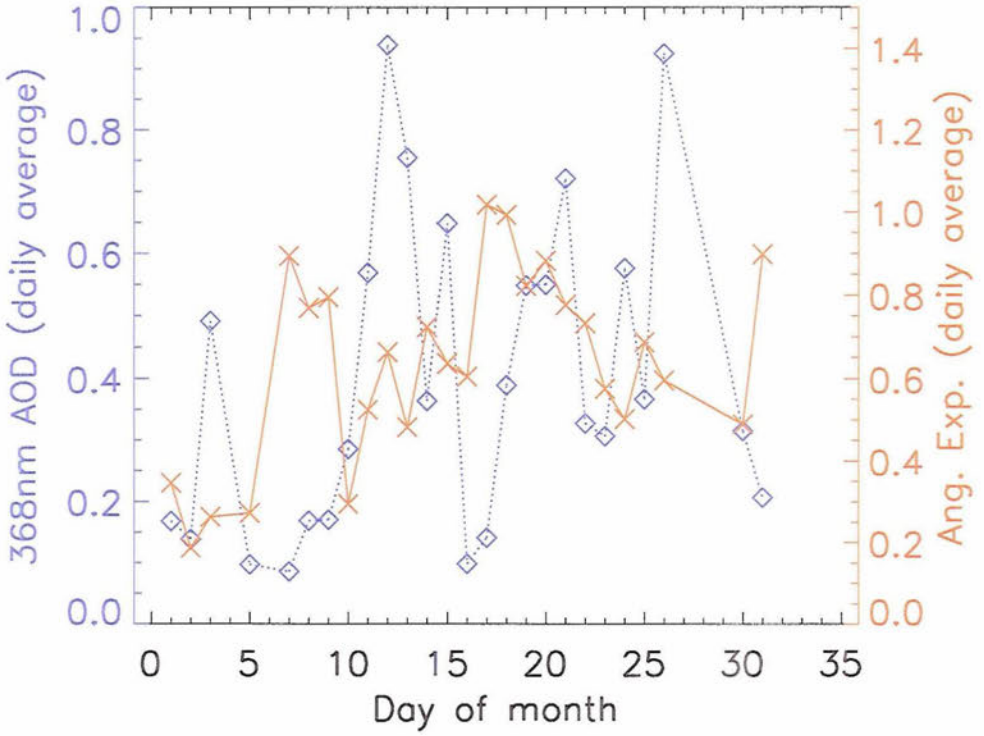

Figure 30: Monthly time series of daily averages of AOD_{368-nm} (left ordinate) and Ångstrom exponent (right ordinate) for May, 2003 at Panther Junction, Texas. AOD_{368-nm} plotted as blue diamonds with dotted line and Ångstrom exponent plotted as red "x" with solid line.

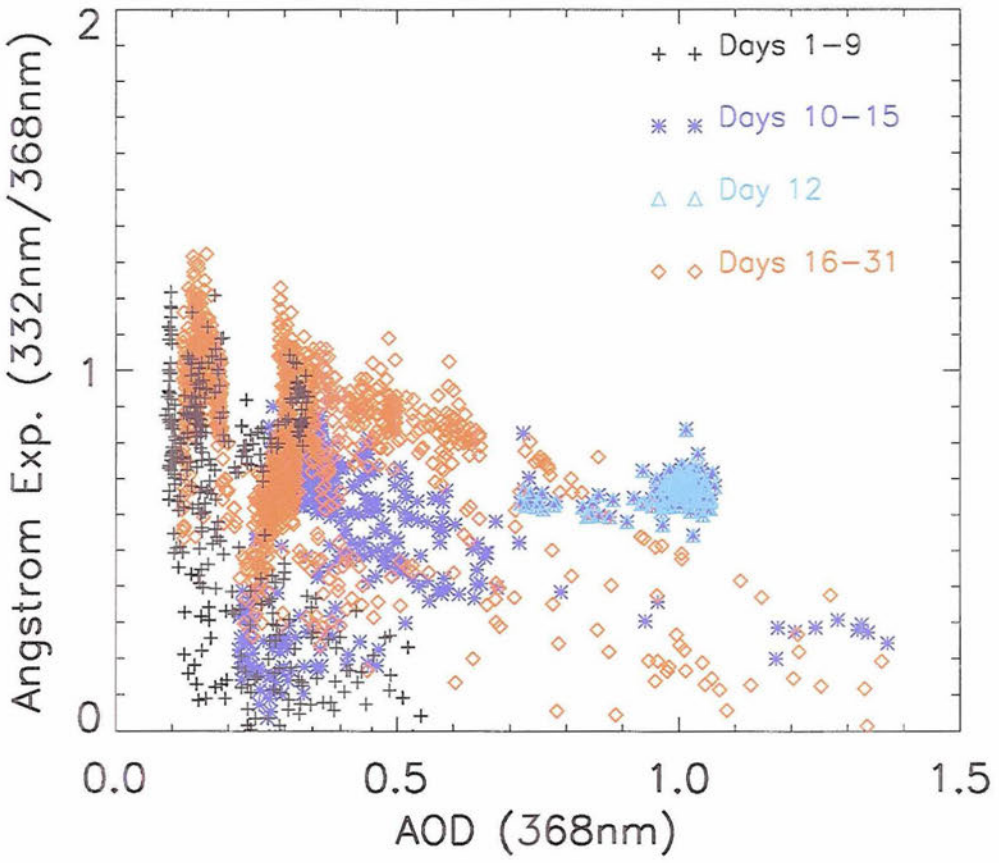

Figure 31: Plots of Ångstrom exponent versus AOD_{368-nm} for May, 2003 at Panther Junction, Texas.

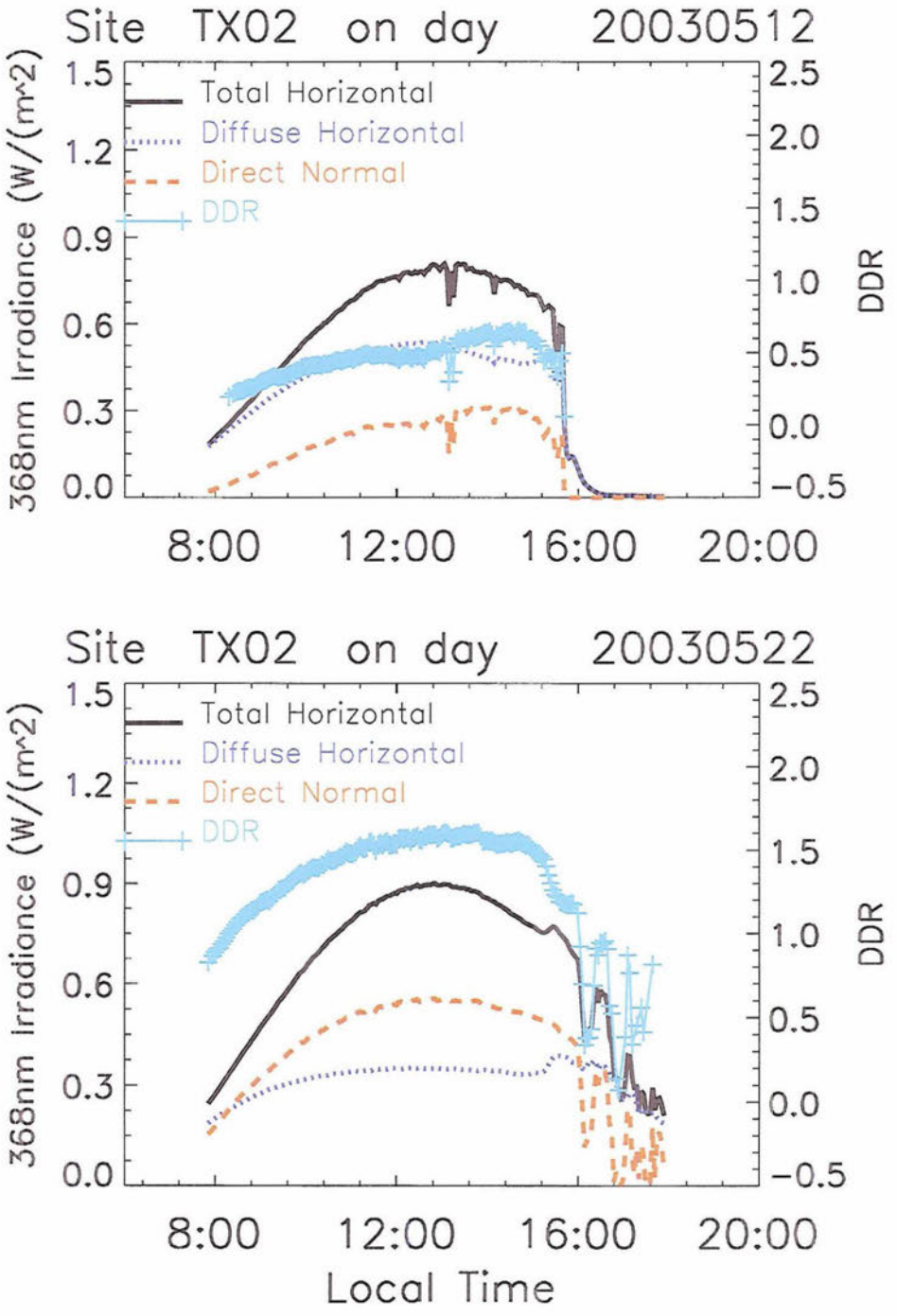

Figure 32: Daily time series of the UV-MFRSR measured irradiances on select days May 12 (top panel) and May 22 (lower panel), 2003 from Panther Junction, Texas. The total horizontal (solid black curve), diffuse horizontal (dotted blue curve) and direct normal (dashed red curve) are plotted against the left ordinate, while the DDR (light blue +'s with solid line) is plotted against the right ordinate. Note the difference in the DDR scale for the 2 days.

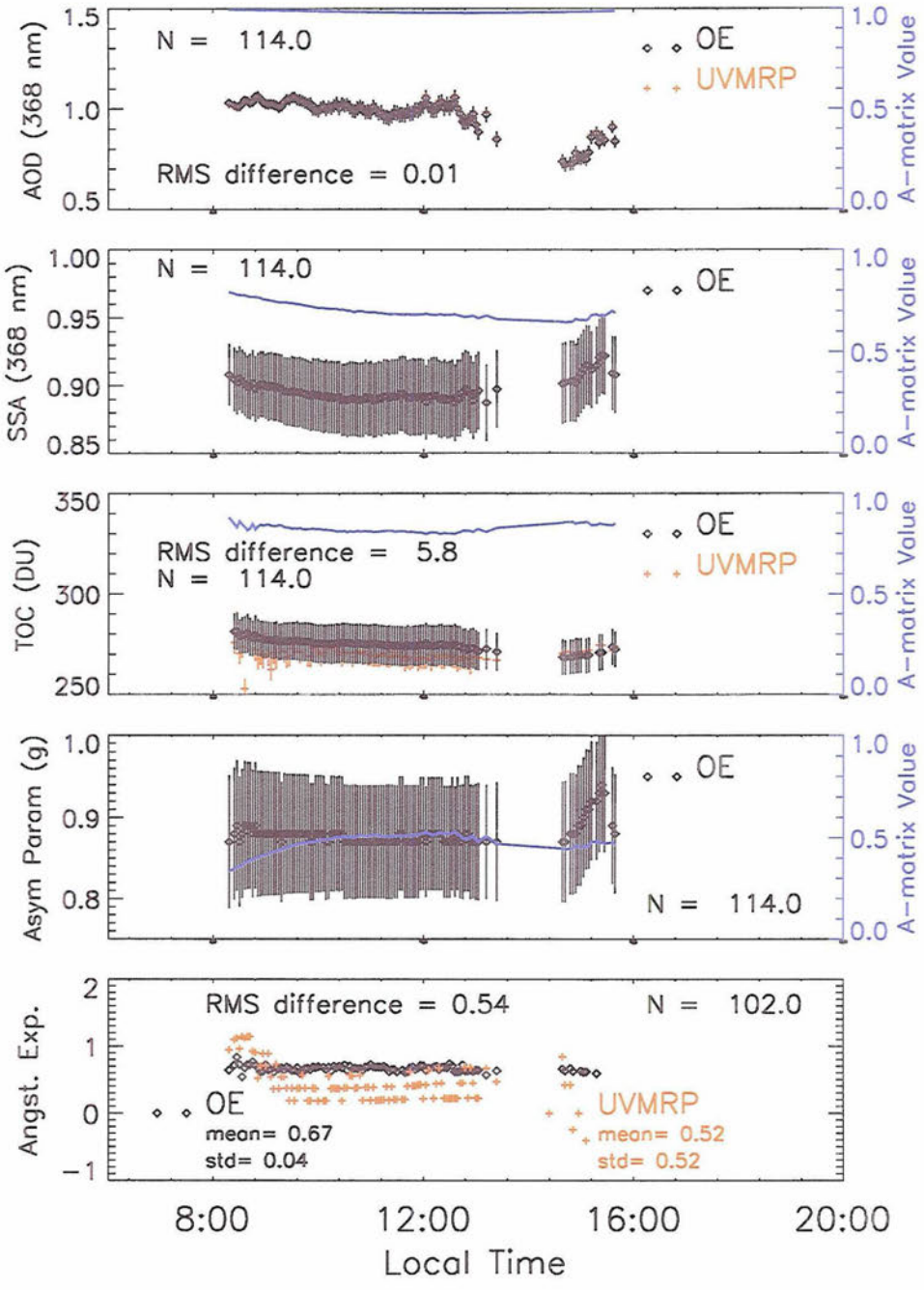

Figure 33: Values of AOD_{368-nm} (top panel), SSA_{368-nm} (2nd panel), TOC (3rd panel), asymmetry factor (4th panel) and calculated Ångstrom exponents (bottom panel) for 12 May 2003 at Panther Junction, Texas. Optimal Estimation (OE) values plotted in black and independently determined values plotted in red. RMS differences calculated with "N" points labeled on each panel. A-matrix values for each retrieval parameter are plotted as solid blue lines against the right ordinate.

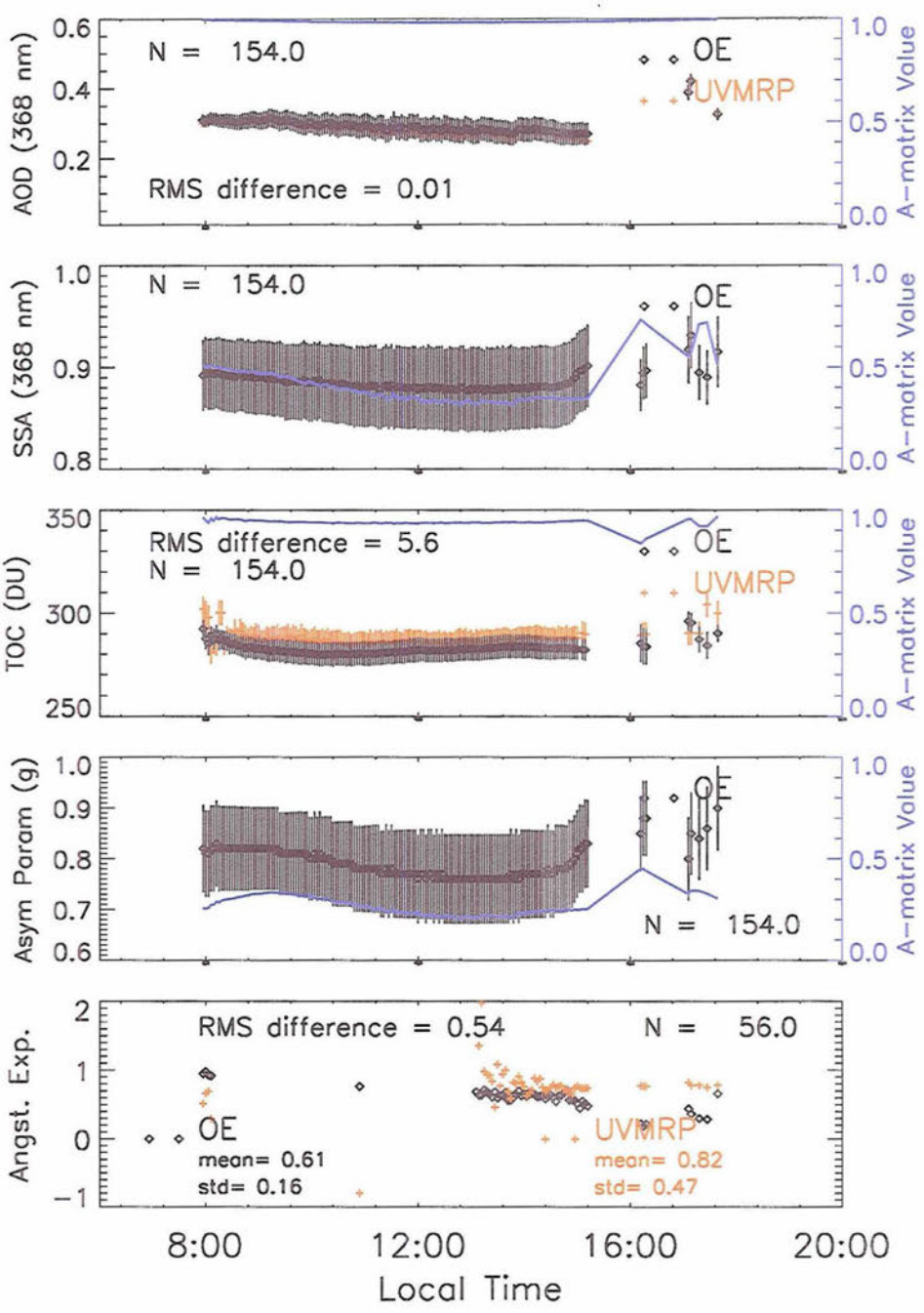

Figure 34: Same as Fig. 33, but for 22 May 2003.

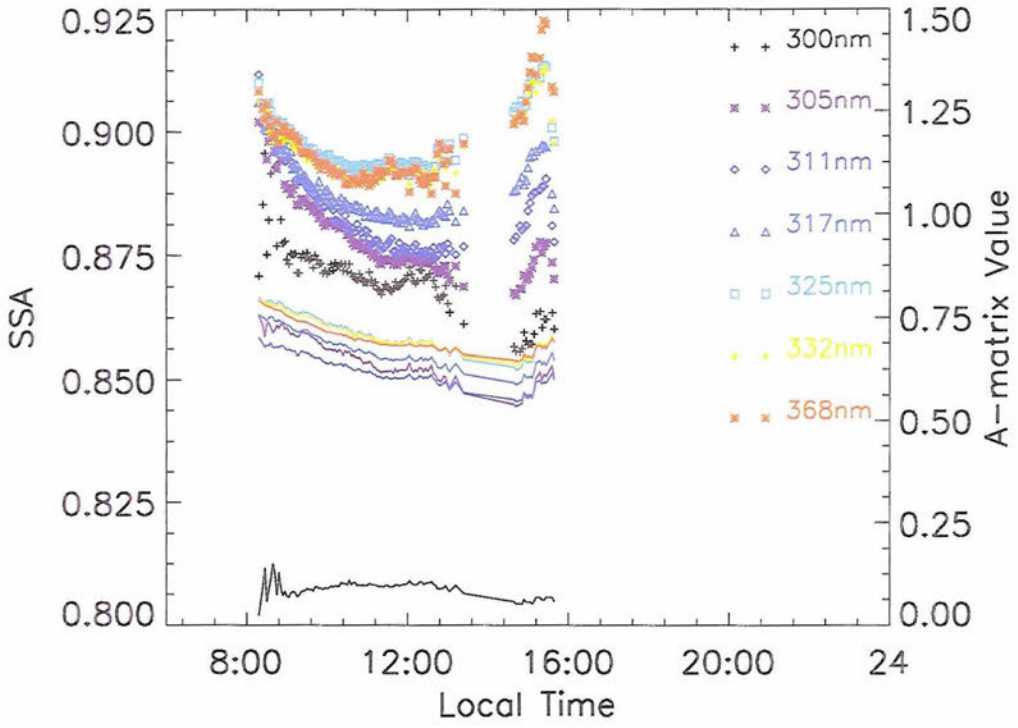

Figure 35: Time series of the OE retrieved SSA values at 7 wavelength channels from Panther Junction, Texas on May 12, 2003 plotted on the left ordinate using various symbols and colors. Associated A-matrix values plotted on the right ordinate as solid lines with color matching the retrieval wavelength.

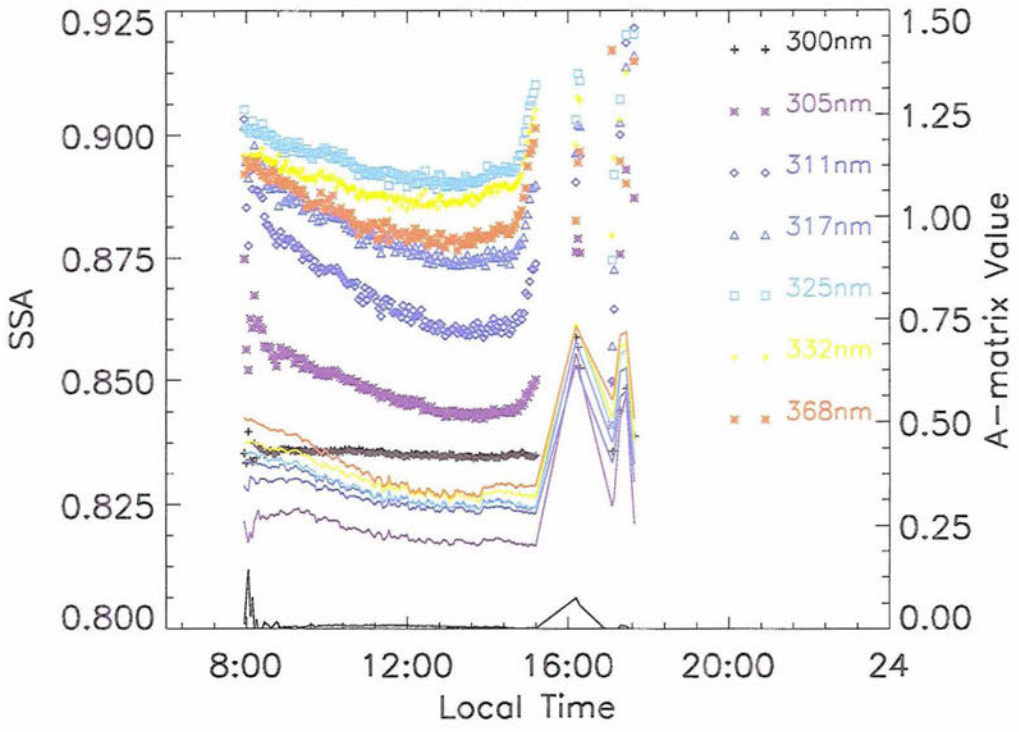

Figure 36: Same as Fig. 35, but for May 22, 2003.

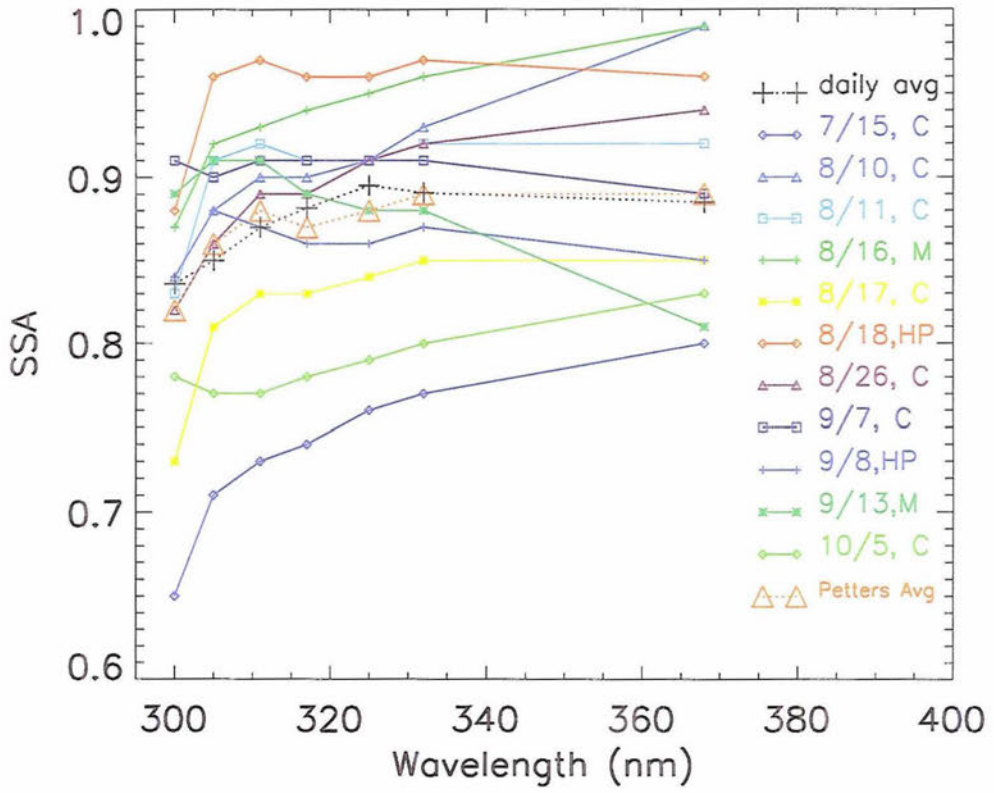

Figure 37: Plots of SSA vs. wavelength from the daily averaged OE retrieved values on May 22, 2003 at Panther Junction, Texas (plotted as black pluses with dotted line) and Petters *et al.* retrieved values of SSA from 1999 at Black Mountain, North Carolina. The air mass type for the Petters *et al.* data are indicated as; C (continental), M (marine) and HP (highly polluted). Averages of each wavelength of the 11 Petters days are plotted as red triangles with a dotted line.

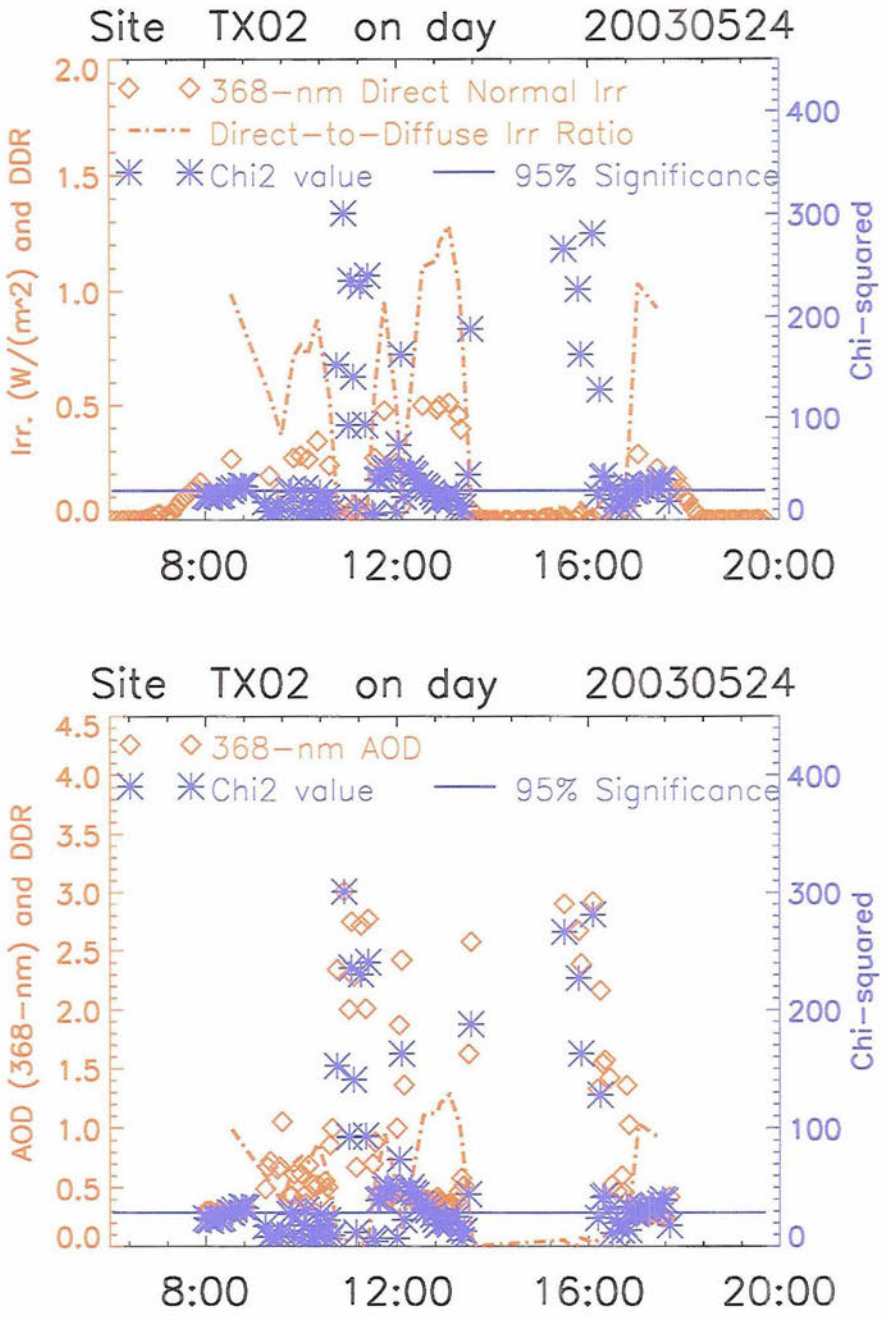

Figure 38: Time series plots from non-cloud screened retrieval testing for May 24, 2003 at Panther Junction, Texas. The top panel shows the measured 368-nm direct irradiance plotted as red diamonds and the direct-to-diffuse irradiance ratio (DDR) plotted as a red dash-dotted line, both against the left ordinate. The χ^2 values are plotted as blue asterisks against the right ordinate along with the upper boundary of the 95% confidence interval as a solid blue line. The lower panel shows AOD_{368-nm} plotted as red diamonds against the left ordinate and χ^2 values plotted as blue asterisks against the right ordinate along with the upper boundary of the 95% confidence interval as a solid blue line.

7. Discussion and Conclusions

7a. *Advantages of the Optimal Estimation Framework*

The major advantages of the Bayesian optimal estimation retrieval described in this work over other independent retrieval methods are as follows;

1. The algorithm requires an explicit model-measurement error budget ($\mathbf{S}_y$) and an independent *a priori* error budget ($\mathbf{S}_a$), both of which allow for covariances among parameters, and each of which can be easily modified to meet the specific requirements of the system;

2. The algorithm provides a simultaneous determination of all the unknown state parameters, contained in $\hat{\mathbf{x}}$;

3. The algorithm provides estimated errors, contained in $\hat{\mathbf{S}}$, for each of the retrieved parameters;

4. The algorithm returns values of the associated statistical significance (χ^2) and retrieval diagnostics (A-matrix values, dof values, H), which allow for analysis of the usefulness of individual retrievals as well as for consistent intercomparison of retrievals from site to site, etc.

7b. *Quantification of Useful Retrieval Domain*

Based on the analysis given in Chapters 5 and 6, a physical domain will be quantified in which the OE retrieval as described in this document can be performed successfully. The idea is to provide a guiding policy for accurate implementation, as well as quick and effective interpretation of retrieval results on a scale useful for an operational product, which will assumably be maintained by an operator with only cursory knowledge of the

theory and interpretation of results of the optimal estimation technique. A summary of the results is presented in Table 17.

The cloud screening algorithm applied in this work relied on deviations and temporal consistencies in the Langley derived AOD_{368-nm} and AOD_{332-nm} calculated by the UVMRP Smirnov et al. (2000). Invariably, all scans made at SZA $> 65°$ were rejected by the screening. Furthermore, the results from the model sensitivity testing indicated that error in the radiative transfer approximation become significant for angles larger than $65°$. Therefore no retrieval results have been analyzed outside of this range, setting the current boundary for this physical parameter.

The retrieval was shown to produce the best results during relatively turbid conditions, i.e., for AOD $> 0.78 \rightarrow 0.66$ from 300- to 368-nm. The majority of photon scattering in the UV spectral range is induced by increased aerosol loading rather than a change in the scattering properties, i.e., changes in AOD have larger impact than changes in SSA Petters et al. (2003). This is partially due to the fact that the SSA of real aerosol particles measured in the earth's atmosphere generally fall within the limited range between about 0.7 and 0.95. However, this range may not hold true for certain types of highly absorbing aerosols, such as black carbon or soot, which are formed via combustion of fossil fuels Hansen and Sato (2001), and are therefore expected to be found near urban centers.

Increasing turbidity causes an increase in the diffuse component of radiation, while simultaneously decreasing the direct beam, yielding smaller values of DDR. Comparing the DDR values from May 12 (peak DDR=0.5) and May 22 (peak DDR=1.5) indicates a factor of 3 difference in DDR. Since the results from May 22 indicated that the retrieval was on the lower limit of success, a DDR of about 1.5 could be considered as a threshold level for allowable retrievals. Although the DDR is a function of SZA, Figure 32 indicates that the peak value normally occurs at mid-day for non-cloud sky conditions. The

DDR therefore provides an *a priori* method for screening data scans before performing the retrieval algorithm, which could produce a large savings in computation time, by avoiding cases in which there is insufficient information contained in the measurements to accurately retrieve values of SSA.

It was shown through the synthetic retrieval testing that the algorithm works best when both the SSA and asymmetry factor are relatively large, such that the number of photons in the transmitted beam which experience a scattering event is also relatively high. The results from that testing showed that reliable retrieval results were produced when SSA$> 0.83 \rightarrow 0.89$ from 300-nm to 368-nm and $g > 0.65$. This was true for SZA out to $65°$. Using these lower boundaries of SSA and g, a lower boundary of AOD was determined to be $\simeq 0.1 \rightarrow 0.07$ from 300-nm to 368-nm, below which the estimated retrieval errors in AOD approached 50%. These boundary conditions of AOD, SSA and g provide an *a posteriori* method for screening retrieval results.

The analysis of the diagnostic results showed that implementing a χ^2 filtering at the 95% confidence interval omitted about half of the successfully retrieved scans. Recall that χ^2 too high is indicative of underestimating the input error budget while χ^2 too low suggests overestimate of the error budget. Since some rejected scans had χ^2 values above the upper boundary and some below the lower boundary it seems that the input error budget as determined from the model sensitivity testing was reasonable. Therefore the number of rejected scans cannot be altered much by manipulation of the error budget. Only adjusting the χ^2 rejection region, i.e., changing the significance interval, will substantially change the number of filtered scans. The selection of the 95% interval seems a reasonable choice, although a less stringent level may be desirable to retain more data. For example the rejection interval could be adjusted in an *a posteriori* manner, such that some predetermined percentage of scans are retained, e.g., set χ^2 such that 90% of scans are retained.

Table 17: Physical domain for successful OE retrieval algorithm.

Parameter	Range or limit	Pre or Post Screening
SZA	$< 65°$	Pre
DDR	< 1.5	Pre
AOD	$> 0.1 - 0.07$ 300nm $\rightarrow$ 368nm	Post (or Pre using UVMRP Langley AODs)
SSA	$> 0.83 - 0.89$ 300nm $\rightarrow$ 368nm	Post
g	> 0.65	Post
χ^2	$6.9 < \chi^2 < 28.9$ for 95% signif.	Post
SSA A-matrix Values	> 0.3 (except 300nm)	Post

An *a posteriori* filter criteria using the A-matrix values can also be implemented. Recall from the discussion in Section v on the wavelength dependence of the SSA that retrieved SSA values with associated A-matrix values below 0.3 should be flagged. This tends to occur when both the turbidity conditions and the scattering properties are relatively low (AOD<0.3). The interpretation of this is that under these atmospheric conditions the amount of photon scattering is small and hence there is not enough information contained in the direct and diffuse beam to distinguish the SSA values. Note that the retrieved values of SSA_{300-nm} always had very low associated A-matrix values. This parameter should be considered as irretrievable by the current version of the algorithm.

7c. *Future Work*

This document describes many improvements to the optimal estimation retrieval algorithm as originally constructed by Goering *et al.* Goering et al. (2005). During the course of this research several tasks were identified which would improve the retrieval and provide validation of the results. They are, in no particular order:

1. Removing the SSA_{300-nm} from the retrieval vector may help remove constraints on the ill-posed nature of the problem. It has been convincingly shown that the UV-MFRSR measurements do not contain enough information to successfully retrieve this parameter.

2. Since the forward model supports radiative transfer calculations in the visible spectral region, a version of the code could be constructed to retrieve the aerosol parameters using visible MFRSR measurements. These instruments are co-located with the UV-MFRSR at every UVMRP research site and make measurements at 415-, 500-, 610-, 665-, 862- and 940-nm with a nominal 10-nm FWHM pass band. Having a longer spectral range of AOD values would help constrain the calculated values of Ångstrom exponents, as well as allow comparison of aerosol properties to a much more comprehensive set of previous research which has been performed in the visible spectrum, e.g., Alexandrov et al. (2002). However, constraining the values of surface albedo in the OE algorithm would be much more difficult, since surface reflectances in the visible wavelength spectrum are highly variable. It might be necessary to add surface albedo as a retrieval parameter into the OE algorithm in the visible case;

3. A comprehensive Langley derived AOD error analysis is needed to provide better intercomparison with the OE retrieved values. This can be done following the arguments given in Section i;

4. Synthetic retrieval testing should be performed with g constrained to determine if the incorporation of g actually increases the usefulness of the retrieval results. The retrieval showed low skill in estimating values of g under low scattering atmospheric conditions, but it is currently unclear if allowing this parameter to vary helped increase the skill of retrieving the other state parameters, especially the

SSA;

5. The Petters *et al.* DDR technique for calculating SSA values should be implemented for intercomparison with the optimal estimation retrieved values. This was done by Goering *et al.*, and results showed favorable comparisons at 332-nm Goering et al. (2005);

6. Initial work has been done using the χ^2 statistic and failed retrievals as a cloud screening tool. If there are clouds or thick water vapor present, the retrieval algorithm should have trouble converging on a solution, or at least provide a poor χ^2 value if it does converge. This provides a self consistent means for screening the irradiance data set, rather than relying on precalculated Langley AOD values, as is currently done using the Smirnov *et al.* screening Smirnov et al. (2000). An alternative is to implement the more robust cloud screening algorithm of Long and Ackerman Long and Ackerman (2000). This technique relies on broadband pyranometer measured irradiances and was used by Goering *et al.* for cloud screening of the Mexico City data set used in that research Goering et al. (2005). However the code was not immediately available for use in this research;

7. Back trajectory calculations to determine the source of air masses, as was done by Wenny *et al.* Wenny et al. (1998), would be valuable for aerosol composition determination. This is a non trivial task, requiring the use of atmospheric transport models and integration of meteorological parameters, but would help clarify interpretation of the retrieved aerosol parameters and provide some validation of the results. Alternatively, the retrieval algorithm could be performed on data from the UVMRP site located at Rayleigh, North Carolina, which is within about 100 miles of the research sites used in the Wenny *et al.* study.

8. Testing of the other 2-stream approximations available within the TUV code should

be performed. These approximations include the following; the delta function method, the delta discrete ordinate method, the Hybrid modified Eddington-delta function method, the Practical Improved Flux Method, the quadrature method, the modified quadrature method, the hemispheric mean method and the hemispheric constant method. Since each two-stream model has been developed with different goals in mind, e.g. for calculation of photolysis rates or solar heating rates, an approximation that may work well under one set of atmospheric conditions may not perform well under another Toon et al. (1989). Model sensitivity testing could be performed following the same technique as that described in Section ii to determine if one of the 2-stream solvers provides fast and accurate results relative to the 4-stream discrete ordinate method which was selected for the current version of the algorithm.

9. Additional solution space testing should be carried out, with TOC and g incorporated as floating, rather than fixed, variables. Results from this testing would indicate if the retrieval solution remained well-behaved and unique relative to these two parameters. This would require a more involved analysis than the 2-D plots of AOD-SSA domain space presented in this document. More powerful 3-D visualization software is available off the shelf, e.g., Vis-5D, available as freeware from the University of Wisconsin.

References

Alexandrov, M., A. Lacis, B. Carlson, and B. Cairns, 2002: Remote Sensing of Atmospheric Aerosols and Trace Gases by Means of Multifilter Rotating Shadowband Radiometer. Part ii: Climatological Applications. *Journal of Atmospheric Sciencies*, **59**, 544–566.

Anderson, T., R. Charlson, N. Bellouin, O. Boucher, M. Chin, S. Chistopher, J. Haywood, Y. Kaufman, S. Kinne, J. Ogren, L. Remer, T. Takemura, D. Tanre, O. Torres, C. Trepte, B. Wielicki, D. Winker, and H. Yu, 2005: An "A-Train" Strategy for Quantifying Direct Aerosol Forcing of Climate. *Bull.Amer.Meteor.Soc.*, **in press**.

Bernhard, G. and G. Seckmeyer, 1999: Uncertainty of Measurements of Spectral Solar UV Irradiance. *Journal of Geophysical Research*, **104**, 14,321–14,345.

Bigelow, D. and J. Slusser, 2000: Establishing the Stability of Multifilter UV Rotating Shadow-band Radiometers. *Journal of Geophysical Research*, **105**, 4833–4840.

Bigelow, D., J. Slusser, A. Beaubien, and J. Gibson, 1998: The USDA Ultraviolet Radiation Monitoring Program. *Bull.Amer.Meteor.Soc.*, **79**, 601–615.

Bruhl, C. and P. Crutzen, 1989: On the Disproportionate Role of Tropospheric Ozone as a Filter Against Solar UV Radiation. *Geophysical Research Letters*, **17**, 703–706.

Deepak, A., 1977: *Inversion Methods in Atmospheric Remote Sounding*. Academic Press, 117-138 pp.

Doda, D. and A. Green, 1980: Surface Reflectance Measurements in the UV from an Airborne Platform. Part 1. *Applied Optics*, **19**, 2140–2145.

— 1981: Surface Reflectance Measurements in the UV from an Airborne Platform. Part 2. *Applied Optics*, **20**, 636–642.

Early, E., A. Thompson, C. Johnson, J. DeLuisi, P. Disterhoft, D. Wardle, E. Wu, W. Mou, Y. Sun, T. Lucas, T. Mestechkina, L. Harrison, J. Berndt, and D. Hayes, 1988a: The 1995 North American Interagency Intercomparison of Ultraviolet Monitoring Spectroradiometers. *J. Res. Natl. Inst. Stand. Technol.*, **103**, 15–62.

Early, E., E. Thompson, and P. Disterhoft, 1988b: Field Calibration Unit for Ultraviolet Spectroradiometers. *Applied Optics*, **37**, 6664–6670.

Engelen, R. J. and G. L. Stephens, 1997: Infrared Radiative Transfer in the 9.6μm Band: Application to TIROS Operational Vertical Sounder Ozone Retrieval. *Journal of Geophysical Research*, **102**, 6929–6939.

Farman, J., B. Gardiner, and J. Shanklin, 1985: Large Losses of Total Ozone in Antarctica Reveal Seasonal ClO_x/NO_x Interaction. *Nature*, **315**, 207–210.

Frederick, J. and D. Lubin, 1988: The Budget of Biologically Active Ultraviolet Radiation in the Earth-Atmosphere System. *Journal of Geophysical Research*, **93**, 3825–3832.

Frederick, J., H. Snell, and E. Haywood, 1989: Solar Ultraviolet Radiation at the Earth's Surface. *Photochem. Photobiol*, **51**, 443–450.

Gao, W., J. Slusser, J. Gibson, G. Scott, D. Bigelow, J. Kerr, and B. McArthur, 2001: Direct-Sun Column Ozone Retrieval by the Ultraviolet Multifilter Rotating Shadow-Band Radiometer and Comparison with Those from Brewer and Dobson Spectrophotometers. *Applied Optics*, **40**, 3149–3155.

Goering, C. D., T. S. L'Ecuyer, G. L. Stephens, J. R. Slusser, G. Scott, J. Davis, J. C. Barnard, and S. Madronich, 2005: Simultaneous Retrievals of Column Ozone and Aerosol Optical Properties from Direct and Diffuse Solar Irradiance Measurements. *Journal of Geophysical Research*, **110**.

Grant, R. and J. Slusser, 2003: Spatial Variability in UV Radiation During the Growing Season Across the Continental USA. *Theor. Appl. Climatol.*, **74**, 167–177.

Gröbner, J. and J. Kerr, 2001: Ground-Based Determination of the Spectral Ultraviolet Extraterrestrial Solar Irradiance: Providing a Link Between Space-Based and Ground-Based Solar UV Measurements. *Journal of Geophysical Research*, **106**, 7211–7217.

Hand, J., S. Kreidenweis, D. E. Sherman, J. Collett, S. Hering, D. Day, and W. Malm, 2002: Aerosol Size Distributions and Visibility Estimates During the Big Bend Regional Aerosol and Visibility Observational (BRAVO) Study. *Atmospheric Environment*, **36**, 5043–5055.

Hansen, J. and M. Sato, 2001: Trends of Measured Climate Forcing Agents. *PNAS*, **98**, 14778–14783.

Harrison, L. and J. Michalsky, 1994: Objective Algorithm for the Retrieval of Optical Depths from Ground-Based Measurements. *Applied Optics*, **33**, 5126–5132.

Harrison, L., J. Michalsky, and J. Berndt, 1994: Automated Multifilter Rotating Shadow-Band Radiometer: An Instrument for Optical Depth and Radiation Measurements. *Applied Optics*, **33**, 5118–5125.

Harwood, M. and R. Jones, 1994: Temperature Dependent Ultraviolet-Visible Absorption Cross Sections of NO_2 and N_2O_4: Low-Temperature Measurements of the Equilibrium Constant for $2NO_2 \rightleftharpoons N_2O_4$. *Journal of Geophysical Research*, **99**, 22,955–22,964.

Hecht, E., 1987: *Optics*. Addison-Wesley Publishing Company, Reading, Massachusetts.

Hidy, G., ed., 1972: *Aerosols and Atmospheric Chemistry*. Academic Press, New York, 149-153 pp.

Holben, B., T. Eck, I. Slutsker, D. Tanre, J. Buis, A. Setzer, E. Vermote, J. Reagan, Y. Kaufman, T. Nakajima, F. Lavenu, I. Jankowiak, and A. Smirnov, 1998: AERONET–A Federated Instrument Network and Data Archive for Aerosol Characterization. *Remote Sensing of the Environment*, **66**, 1–16.

Houghton, J., Y. Ding, D. Griggs, M. Noguer, P. van der Linden, X. Dai, K. Maskell, and C. Johnson, 2001: *Climate Change 2001: The Scientific Basis. Contribution of Working Group I to the Third Assessment Report of the Intergovernmental Report on Climate Change*. Cambridge University Press, Cambridge, U.K.

Huffman, R. E., 1992: *Atmospheric Ultraviolet Remote Sensing*. Academic Press, Inc, San Diego, California.

Im, J.-S., V. K. Saxena, and B. N. Wenny, 2001: An Assessment of Hygroscopic Growth Factors for Aerosols in the Surface Boundary Layer for Computing Direct Radiative Forcing. *Journal of Geophysical Research*, **106**, 20,213–20,224.

Janson, G. and J. Slusser, 2003: Long-Term Stability of UV Multifilter Rotating Shadowband Radiometers. *Ultraviolet Ground- and Space-based Measurements, Models and Effects III, San Diego, California, August 4–6, 2003*, J. Slusser, J. Herman, and W. Gao, eds., The International Society for Optical Engineering, Bellingham, Washington, volume 5156, 94–100.

Johnson, R. A. and G. K. Bhattacharyya, 1996: *Statistics: Principles and Methods*. John Wiley and Sons, Inc.

Kimlin, M., N. Downs, and A. Parisi, 2003: Comparison of Human Facial UV Exposure at High and Low Latitudes and the Potential Impact on Dermal Vitamin D Production. *Photochem. Photobiol. Sci.*, **2**, 370–375.

Krotkov, N., P. K. Bhartia, J. Herman, J. Slusser, G. Labow, G. Scott, G. Janson, T. F. Eck, and B. Holben, 2005: Aerosol Ultraviolet Absorption Experiment (2002 to 2004), Part 1: Ultraviolet Multifilter Rotating Shadowband Radiometer Calibration and Intercomparison with CIMEL Sunphotometers. *Optical Engineering*, **44**.

Kylling, A., A. Albold, and G. Seckmeyer, 1997: Transmittance of a Cloud is Wavelength-Dependent in the UV-Range: Physical Interpretation. *Geophysical Research Letters*, **24**, 397–400.

Kylling, A., A. Bais, M. Blumthaler, J. Schreder, C. Zerefos, and E. Kosmidis, 1998: Effect of Aerosols on Solar UV Irradiances During the Photochemical Activity and Solar Ultraviolet Radiation Campaign. *Journal of Geophysical Research*, **103**, 26051–26060.

Lantz, K., P. Disterhoft, E. Early, A. Thompson, J. DeLuisi, J. Berndt, L. Harrison, P. Kiedron, J. Ehramjian, G. Bernhard, L. Cabasug, J. Robertson, W. Mou, T. Taylor, J. Slusser, D. Bigelow, B. Durham, G. Janson, D. Hayes, M. Beaubien, and A. Beaubien, 2002: The 1997 North American Interagency Intercomparison of Ultraviolet Spectroradiometers Including Narrowband Filter Radiometers. *J. Res. Natl. Inst. Stand. Technol.*, **107**, 19–62.

Lantz, K. O., P. Disterhoft, J. J. DeLuisi, E. Early, A. Thompson, D. Bigelow, and J. Slusser, 1999: Methodology for Deriving Clear-Sky Erythemal Calibration Factors for UV Broadband Radiometers of the U.S. Central UV Calibration Facility. *Journal of Atmospheric and Oceanic Technology*, **16**, 1736–1752.

Larason, T. C. and C. L. Cromer, 2001: Sources of Error in UV Radiation Measurements. *J. Res. Natl. Inst. Stand. Technol.*, **106**, 649–656.

L'Ecuyer, T., P. Gabriel, K. Leesman, S. J. Cooper, and G. L. Stephens, 2005: Objective

Assessment of the Information Content of Visible and Infrared Radiance Measurements for Cloud Microphysical Property Retrievals Over the Global Oceans. Part I: Liquid Clouds. *Journal of Applied Meteorology*.

L'Ecuyer, T. and G. L. Stephens, 2002: An Estimation-Based Precipitation Retrieval Algorithm for Attenuating Radars. *Journal of Applied Meteorology*, **41**, 271–285.

Leszczynski, K., K. Jokela, L. Ylianttila, R. Visuri, and M. Blumthaler, 1998: Erythemally Weighted Radiometers in Solar UV Monitoring: Results from the WMO/STUK Intercomparison. *Photochemistry and Photobiology*, **67**, 212–221.

Liou, K., 2002: *An Introduction to Atmospheric Radiation*. Academic Press.

Long, C. N. and T. P. Ackerman, 2000: Identification of Clear Skies from Broadband Pyranometer Measurements and Calculation of Downwelling Shortwave Cloud Effects. *Journal of Geophysical Research*, **105**, 15,609–15,626.

Lorente, J., A. Redano, and X. DeCabo, 1994: Influence of Urban Aerosol on Spectral Solar Irradiance. *Journal of Applied Meteorology*, **33**, 406–415.

Madronich, S., 1993: *Environmental UV Photobiology*, Plenum Press, Springer, New York. 1–39.

McMeeking, G., S. Kreidenweis, C. Carrico, T. Lee, and J. Collet, 2005: Observations of Smoke-Influenced Aerosol During the Yosemite Aerosol Characterization Study: Size Distributions and Chemical Composition. *Journal of Geophysical Research*, **110**.

Nakajima, T., A. Higurashi, K. Kawamoto, and J. Penner, 2001: A Possible Correlation Between Satellite-Derived Cloud and Aerosol Microphysical Parameters. *Geophysical Research Letters*, **28**, 1171–1174.

Nicolet, M., 1984: On the Molecular Scattering in the Terrestrial Atmosphere: An Empirical Formula for its Calculation in the Homosphere. *Planet. Space Sci.*, **32**, 1467–1468.

Petters, J., V. Saxena, J. Slusser, B. Wenny, and S. Madronich, 2003: Aerosol Single Scattering Albedo Retrieved from Measurements of Surface Irradiance and a Radiative Transfer Model. *Journal of Geophysical Research*, **108**, 4288.

Ramanathan, V., P. Crutzen, J. Kiehl, and D. Rosenfeld, 2001: Aerosols, Climate and the Hydrological Cycle. *Science*, **294**, 2119–2124.

Rodgers, C. D., 2000: *Inverse Methods For Atmospheric Sounding: Theory and Practice*. World Scientific Publishing Co. Pte. Ltd.

Rogers, R. and M. Yau, 1989: *A Short Course in Cloud Physics*. Butterworth-Heinemann.

Sabburg, J., J. Rives, R. Meltzer, T. Taylor, G. Schmalzle, S. Zheng, N. Huang, and A. Wilson, 2002: Comparisons of Corrected Daily Integrated Erythemal UVR Data from the U.S. EPA/UGA Network of Brewer Spectroradiometers with Model and TOMS-Inferred Data. *Journal of Geophysical Research*, **107**, 4676.

Schwander, H., P. Koepke, and A. Ruggaber, 1997: Uncertainties in Modeled UV Irradiances Due to Limited Accuracy and Availability of Input Data. *Journal of Geophysical Research*, **102**, 9419–9429.

Seckmeyer, G., S. Thiel, M. Blumthaler, P. Fabian, S. Gerber, A. Gugg-Helminger, D.-P. Hader, M. Huber, C. Kettner, U. Kohler, P. Kopke, H. Maier, J. Schafer, P. Suppan, E. Tamm, and E. Thomalla, 1994: Intercomparison of Spectral-UV-Radiation Measurement Systems. *Applied Optics*, **33**, 7805–7811.

Seinfeld, J. H. and S. N. Pandis, 1998: *Atmospheric Chemistry and Physics*. John Wiley and Sons, Inc.

Slusser, J., J. Gibson, D. Bigelow, D. Kolinski, P. Disterhoft, K. Lantz, and A. Beaubien, 2000: Langley Method of Calibrating UV Filter Radiometers. *Journal of Geophysical Research*, **105**, 4841–4849.

Smirnov, A., B. Holben, T. Eck, O. Dubovik, and I. Slutsker, 2000: Cloud-Screening and Quality Control Algorithms for the AERONET Database. *Remote Sensing of the Environment*, **73**, 337–349.

Stamnes, K., S. Tsay, W. Wiscombe, and K. Jayaweera, 1988: Numerically Stable Algorithm for Discrete-Ordinate-Method Radiative Transfer in Multiple Scattering and Emitting Layered Media. *Applied Optics*, **27**, 2502–2509.

Stephens, G. L., 1994: *Remote Sensing of the Lower Atmosphere*. Oxford University Press, Inc., New York, New York.

Suzuki, K., T. Nakajima, A. Numaguti, T. Takemura, K. Kawamoto, and A. Higurashi, 2004: A Study of the Aerosol Effect on a Cloud Field with Simultaneous Use of GCM Modeling and Satellite Observation. *Journal of Atmospheric Sciencies*, **61**, 179–194.

Takemura, T., T. Nozawa, S. Emori, T. Nakajima, and T. Nakajima, 2005: Simulation of Climate Response to Aerosol Direct and Indirect Effects with Aerosol Transport-Radiation Model. *Journal of Geophysical Research*, **110**.

Toon, O., C. Mckay, and T. Ackerman, 1989: Rapid Calculation of Radiative Heating Rates and Photodissociation Rates in Inhomogenous Multiple Scattering Atmospheres. *Journal of Geophysical Research*, **94**, 16,287–16,301.

Twomey, S., 1977: *Introduction to the Mathematics of Inversion in Remote Sensing and Indirect Measurements*. Elsevier Scientific Publishing Company, Amsterdam.

Wallace, J. M. and P. V. Hobbs, 1977: *Atmospheric Science: An Introductory Survey*. Academic Press, London, U.K.

Webb, A. R., 2003: UV Instrumentation for Field and Forest Research. *Agricultural and Forest Meteorology*, **120**.

Wenny, B., V. Saxena, and J. Frederick, 2001: Aerosol Optical Depth Measurements and Their Impact on Surface Levels of Ultraviolet-B Radiation. *Journal of Geophysical Research*, **106**, 17,311–17,319.

Wenny, B., J. Schafer, J. DeLuisi, V. Saxena, W. Barnard, I. Petropavlovshikh, and A. Vergamini, 1998: A Study of Regional Aerosol Radiative Properties and Effects on Ultrviolet-B Radiation. *Journal of Geophysical Research*, **103**, 17083–17097.

Wetzel, M. A., G. E. Shaw, J. R. Slusser, R. D. Borys, and C. F. Cahill, 2003: Physical, Chemical and Ultraviolet Radiative Characteristics of Aerosol in Central Alaska. *Journal of Geophysical Research*, **108**, 4418.

WHO, ed., 1994: *Ultraviolet Radiation: An Authoritative Scientific Review of Environmental and Health Effects of UV, with Reference to Global Ozone Layer Depletion*. United Nations Environment Programme, the International Commision on Non-Ionizing Radiation Protection and the World Health Organization, Geneva.

Appendix A: Description of acronyms, symbols and terminology. Units or size given in [brackets].

AOD Aerosol Optical Depth

CSU Colorado State University

CUCF Central Ultra-violet Calibration Facility, part of NOAA

DE Delta-Eddington (radiative transfer approximation)

DU Dobson Units, units of total ozone column

dof degrees of freedom

DOM Discrete Ordinate Method (radiative transfer approximation)

DDR Direct-to-Diffuse Ratio (of irradiances)

EM Electro-Magnetic (energy)

ERB Earth Radiation Budget

IC Information Content (of a retrieval)

NCAR National Center for Atmospheric Research

nm nanometers, 10^{-9} meters

μ **m** micrometers, 10^{-6} meters

NOAA National Oceanic and Atmospheric Administration

NREL National Resource Ecology Laboratory

NWS National Weather Service

OE Optimal Estimation

PDF Probability Distribution Function

ppb parts per billion

ppm parts per million

ppt parts per trillion

RHS Right Hand Side

RMS Root Mean Square

SSA Single Scattering Albedo

SZA Solar Zenith Angle

TOA Top Of Atmosphere

TOC Total Ozone Column

TOMS Total Ozone Mapping Spectrometer, satellite

TUV Tropospheric Ultraviolet-Visible (radiative transfer model)

USDA United States Departement of Agriculture

UV Ultra-Violet (radiation)

UVI Ultra-Violet Index

UV-MFRSR Ultra-Violet Multi-Filter Rotating Shadow-Band Radiometer

UVMRP Ultra-Violet Monitoring and Research Program

WHO World Health Organization

α Ångstrom exponent

α_λ wavelength-dependent ozone absorption coefficients

α_p particle polarizibility

α_s surface albedo

β single scattering albedo

β_t turbidity coefficient, used in Ångstrom formulation

δ combined uncertainties from all sources of error, used in S_y

ϵ error

ξ percent error in retrieved parameters

g asymmetry factor, first moment of the phase function

k coefficient of extinction (k_e), absorption (k_a) or scattering (k_s) $[cm^{-1}]$

f flux, luminosity $[W]$

F flux density, irradiance, $[W/(m^2)]$

H Shannon information content

h Planck's constant, 6.63x10^{-34} [Js]

I intensity, radiance $[W/(m^2 * sr)]$

λ wavelength

$\tilde{\lambda}$ eigenvalues of a matrix

N number appearing

n_0 particle number density $[cm^{-3}]$

$n(r)$ aerosol size distribution, in terms of particle radius r

γ slope of the straight line through $\log n(r)$

Ω total ozone column

ω aerosol single scattering albedo

$P(\cos\Phi)$ phase function in terms of the scattering angle, Φ

Φ scattering angle, angle between the incident beam and the scattered beam

ϕ azimuthal angle of the sun

Q_s extinction efficiency

sr steradian, unit for solid angle

$\mu = \cos\theta$, the inverse of the air mass ratio defined by m, where θ is the solar zenith angle

$m = \sec\theta$, ratio of the air mass between the sun and observer to the air mass with respect to the local zenith distance

ν wavenumber $[cm^{-1}]$

$\tilde{\nu}$ oscillator frequency $[s^{-1}]$

θ solar zenith angle

ρ particle density $[gcm^{-3}]$

σ cross section of extinction (σ_e), absorption (σ_a) or scattering (σ_s) $[cm^2]$

σ standard deviation

η mass cross section of extinction (η_e), absorption (η_a) or scattering (η_s) $[cm^2 g^{-1}]$

τ total optical depth

V voltage

W Watts

x size parameter

χ^2 statistical significance of a chi-squared distribution

z altitude

UV-A $400 - 320nm$

UV-B $320 - 280nm$

UV-C $< 280nm$

a priori knowledge of the state based on physics and/or climatology

F Forward model

R Retrieval process

b parameters to which the model is sensitive but are not allowed to vary, e.g., surface albedo, vertical temperature profile, etc.

c retrieval method parameters, e.g., convergence criteria, number of iterations allowed, etc.

$\mathbf{m}$ number of measurements, 14

$\mathbf{n}$ number of state parameters, 15 or 16

$\mathbf{p}$ rank of the kernel matrix, $\mathbf{K}$

$\mathbf{y}$ vector of measurements, [1xm]

$\mathbf{x}$ vector of state parameters, [1xn]

$\hat{\mathbf{x}}$ vector of estimated values of state parameters, [1xn]

$\mathbf{x_a}$ vector of *a priori* values of state parameters, [1xn]

$\mathbf{S_y}$ matrix of measurement-model error covariances, [mxm]

$\mathbf{S_y}$ matrix of error covariances in *a priori* state parameters, [nxn]

$\mathbf{K}$ matrix of contribution functions, kernel, Jacobian, [mxn]

$\mathbf{F(x)}$ forward model evaluated using state parameters, $\mathbf{x}$, as inputs

$\hat{\mathbf{S}} = (\mathbf{K^T S_y^{-1} K} + \mathbf{S_a^{-1}})^{-1}$, matrix of estimated retrieval error covariances, [nxn]

$P(x)$ probability distribution of state space

$P(y)$ probability distribution of measurement space

$P(x, y)$ joint probability distribution of state and measurement spaces

$P(y|x)$ probability distribution of measurement space for a given state space, described by the forward model

$P(x|y)$ probability distribution of state space for a given measurement space, the solution to the retrieval process